# PFLOTRAN Development FY2021

## Spent Fuel and Waste Disposition

*Prepared for*
*U.S. Department of Energy*
*Spent Fuel & Waste Science and Technology*

*M. Nole, R.C. Leone, H.D. Park, M. Paul,*
*A. Salazar, G.E. Hammond[*], P.C. Lichtner[**]*

*Sandia National Laboratories*
*[*]Pacific Northwest National Laboratory*
*[**]OFM Research*

*July 21, 2021*
**M3SF-21SN010304072**
**SAND2021-xxxxx R**

## DISCLAIMER

This is a technical report that does not take into account contractual limitations or obligations under the Standard Contract for Disposal of Spent Nuclear Fuel and/or High-Level Radioactive Waste (Standard Contract) (10 CFR Part 961). For example, under the provisions of the Standard Contract, spent nuclear fuel in multi-assembly canisters is not an acceptable waste form, absent a mutually agreed to contract amendment.

To the extent discussions or recommendations in this report conflict with the provisions of the Standard Contract, the Standard Contract governs the obligations of the parties, and this report in no manner supersedes, overrides, or amends the Standard Contract.

This report reflects technical work which could support future decision making by DOE. No inferences should be drawn from this report regarding future actions by DOE, which are limited both by the terms of the Standard Contract and Congressional appropriations for the Department to fulfill its obligations under the Nuclear Waste Policy Act including licensing and construction of a spent nuclear fuel repository.

Sandia National Laboratories is a multi-mission laboratory managed and operated by National Technology & Engineering Solutions of Sandia, LLC., a wholly owned subsidiary of Honeywell International, Inc., for the U.S. Department of Energy's National Nuclear Security Administration under contract DE-NA0003525.

# APPENDIX E

# NFCSC DOCUMENT COVER SHEET[1]

Name/Title of
Deliverable/Milestone/Revision No. PFLOTRAN Development FY2021 / M3SF-21SN010304072
Work Package Title and Number GDSA – PFLOTRAN Development – SNL / SF-21SN01030407
Work Package WBS Number. 1.08.01.03.04

Responsible Work Package Manager Michael Nole (Name/Signature)
Date Submitted 07/19/2021

| | | | | |
|---|---|---|---|---|
| Quality Rigor Level for Deliverable/Milestone[2] | ☐ QRL-1<br>☐ Nuclear Data | ☐ QRL-2 | ☒ QRL-3 | ☐ QRL-4<br>Lab QA Program[3] |

This deliverable was prepared in accordance with Sandia National Laboratories
(Participant/National Laboratory Name)

QA program which meets the requirements of
☒ DOE Order 414.1 ☐ NQA-1 ☒ Other

**This Deliverable was subjected to:**

| | |
|---|---|
| ☒ Technical Review | ☐ Peer Review |
| **Technical Review (TR) Review Documentation Provided** | **Peer Review (PR) Review Documentation Provided** |
| ☐ Signed TR Report or, | ☐ Signed PR Report or, |
| ☐ Signed TR Concurrence Sheet or, | ☐ Signed PR Concurrence Sheet |
| or, | |
| ☒ Signature of TR Reviewer(s) below | ☐ Signature of PR Reviewer(s) below |

**Name and Signature of Reviewers**
Tara LaForce

**NOTE 1:** *Appendix E should be filled out and submitted with the deliverable. Or, if the PICS:NE system permits, completely enter all applicable information in the PICS:NE Deliverable Form. The requirement is to ensure that all applicable information is entered either in the PICS:NE system or by using the NFCSC Document Cover Sheet.*

- *In some cases there may be a milestone where an item is being fabricated, maintenance is being performed on a facility, or a document is being issued through a formal document control process where it specifically calls out a formal review of the document. In these cases, documentation (e.g., inspection report, maintenance request, work planning package documentation or the documented review of the issued document through the document control process) of the completion of the activity, along with the Document Cover Sheet, is sufficient to demonstrate achieving the milestone.*

**NOTE 2**: *If QRL 1, 2, or 3 is not assigned, then the QRL 4 box must be checked, and the work is understood to be performed using laboratory QA requirements. This includes any deliverable developed in conformance with the respective National Laboratory / Participant, DOE or NNSA-approved QA Program.*

**NOTE 3:** *If the lab has an NQA-1 program and the work to be conducted requires an NQA-1 program, then the QRL-1 box must be checked in the work Package and on the Appendix E cover sheet and the work must be performed in accordance with the Lab's NQA-1 program. The QRL-4 box should not be checked.*

# ACKNOWLEDGEMENTS

This report incorporates principal contributions in Section 2 from the following co-authors:

Glenn Hammond: Section 2.2.1 (Multi-continuum Transport), Section 2.4.4 (International User Base), and Section 2.2.5 (Open Source)

Rosie Leone: Section 2.1.2 (QA Test Suite), Section 2.1.3 (Computing Resources), and Section 2.2.1 (Multi-continuum Transport)

Peter Lichtner: Section 2.2.1 (Multi-continuum Transport: dual-continuum validation) and Section 2.2.2 (Design Document: Variable Mineral Surface Area)

Michael Nole: Section 2.1.1 (Jira), Section 2.2.7 (Criticality Sub-module), and Section 2.4 (Integration and Outreach)

Heeho Park: Section 2.1.3 (Computing Resources), Section 2.3.2 (Linear Solvers) 2.3.3 (Non-linear Solvers), and Section 2.3.4 (Numerical Experiments)

Matt Paul: Section 2.3.1 (Characteristic Curve Smoothing)

Alex Salazar: Section 2.2.3 (Thermal Characteristic Curves), Section 2.2.4 (Thermal Conductivity Anisotropy), Section 2.2.5 (Special Thermal Conductivity Models), Section 2.2.6 (Smectite-Illite Transition), and Section 2.2.7 (Criticality Sub-module)

The authors thank Tara LaForce of Sandia National Laboratories (SNL) for her thoughtful technical review, Spencer Jordan for his contribution to the test problem in Section 2.1.2, and staff from U.S. Department of Energy Office of Nuclear Energy (DOE-NE), Prasad Nair (DOE NE-81), for discussions, oversight, and guidance on topics addressed in this report.

# EXECUTIVE SUMMARY

The Spent Fuel & Waste Science and Technology (SFWST) Campaign of the U.S. Department of Energy (DOE) Office of Nuclear Energy (NE), Office of Spent Fuel & Waste Disposition (SFWD) is conducting research and development (R&D) on geologic disposal of spent nuclear fuel (SNF) and high-level nuclear waste (HLW). A high priority for SFWST disposal R&D is to develop a disposal system modeling and analysis capability for evaluating disposal system performance for nuclear waste in geologic media.

This report describes fiscal year (FY) 2021 advances of the PFLOTRAN Development group of the SFWST Campaign. The mission of this group is to develop a geologic disposal system modeling capability for nuclear waste that can be used to probabilistically assess the performance of generic disposal concepts. In FY 2021, development proceeded along three main thrusts: software infrastructure, code performance, and process model advancement. Software infrastructure improvements included implementing an Agile software development framework and making improvements to the QA Test Suite. Code performance improvements included development of advanced linear and nonlinear solvers as well as design of flexible smoothing algorithms for capillary pressure functions. Process modeling advancements included the addition of flexible thermal conductivity function definitions and refinement of multi-continuum reactive transport to support Sandia's participation in DECOVALEX.

This report fulfills the GDSA PFLOTRAN Development Work Package Level 3 Milestone – *PFLOTRAN Development, FY2021*, M3SF-21SN010304072.

# CONTENTS

# FIGURES

# TABLES

# NOMENCLATURE

| | |
|---|---|
| DCDM | Dual Continuum Disconnected Matrix |
| DFN | Discrete Fracture Network |
| DOE | U.S. Department of Energy |
| DPC | Dual-Purpose Canister |
| EBS | Engineered Barrier System |
| NBS | Natural Barrier System |
| ECPM | Equivalent Continuous Porous Medium |
| GDSA | Geologic Disposal Safety Assessment |
| HLW | High-level Nuclear Waste |
| LBNL | Lawrence Berkeley National Laboratory |
| MINC | Multiple Interacting Continua: dual porosity model where the primary and secondary continuum are solved simultaneously |
| NE | DOE Office of Nuclear Energy |
| ORNL | Oak Ridge National Laboratory |
| PNNL | Pacific Northwest National Laboratory |
| QA | Quality Assurance |
| R&D | Research & Development |
| SFWD | Spent Fuel & Waste Disposition |
| SFWST | Spent Fuel & Waste Science and Technology |
| S-I | Smectite-to-Illite |
| SNF | Spent Nuclear Fuel |
| SNL | Sandia National Laboratories |
| TCC | Thermal Characteristic Curve |
| TH | Thermal-Hydrological |
| V&V | Verification & Validation |
| WF | Waste Form |

(This page left intentionally blank.)

# 1. INTRODUCTION

The Spent Fuel & Waste Science and Technology (SFWST) Campaign of the U.S. Department of Energy (DOE) Office of Nuclear Energy (NE), Office of Spent Fuel & Waste Disposition (SFWD) is conducting research and development (R&D) on geologic disposal of spent nuclear fuel (SNF) and high-level nuclear waste (HLW). A high priority for SFWST disposal R&D is disposal system modeling (DOE 2012, Table 6; Sevougian et al., 2019b). The SFWST GDSA PFLOTRAN Development work package is charged with developing subsurface simulation software for use in system performance assessment of nuclear waste disposal in geologic media.

This report fulfills the requirements of the GDSA PFLOTRAN Development work package (SF-21SN01030407) Level 3 Milestone – FY21 Advances in GDSA PFLOTRAN Development, M3SF-21SN010304072.

## 1.1 PFLOTRAN

PFLOTRAN (Hammond et al., 2011; Lichtner and Hammond, 2012) is an open source, multi-phase flow and reactive transport simulator designed to leverage massively-parallel high-performance computing to simulate subsurface earth system processes. PFLOTRAN has been employed on petascale leadership-class DOE computing resources (e.g., Jaguar [at Oak Ridge National Laboratory (ORNL)] and Franklin/Hopper [at Lawrence Berkeley National Laboratory (LBNL)]) to simulate THC processes at the Nevada Test Site (Mills et al., 2007), multi-phase $CO_2$-$H_2O$ for carbon sequestration (Lu and Lichtner 2007), CO2 leakage within shallow aquifers (Navarre-Sitchler et al., 2013), and uranium fate and transport at the Hanford 300 Area (Hammond et al., 2007; Hammond et al., 2008; Hammond and Lichtner, 2010; Hammond et al., 2011; Chen et al., 2012; Chen et al., 2013). PFLOTRAN is also undergoing qualification for use in PA at the Waste Isolation Pilot Plant (WIPP).

PFLOTRAN solves the non-linear partial differential equations describing non-isothermal multi-phase flow and reactive transport in porous media. Parallelization is achieved through domain decomposition using the Portable Extensible Toolkit for Scientific Computation (PETSc) (Balay et al., 2013). PETSc provides a flexible interface to data structures and solvers that facilitate the use of parallel computing. PFLOTRAN is written in Fortran 2003/2008 and leverages state of the art Fortran programming (i.e., Fortran classes, pointers to procedures, etc.) to support its object-oriented design. The code provides “factories” within which the developer can integrate a custom set of process models and time integrators for simulating surface and subsurface multi-physics processes. PFLOTRAN employs a single, unified framework for simulating multi-physics processes on both structured and unstructured grid discretizations (i.e., there is no duplication of the code that calculates multi-physics process model functions in support of structured and unstructured discretizations). The code requires a small, select set of third-party libraries (e.g., MPI, PETSc, BLAS/LAPACK, HDF5, Metis/Parmetis). Both the unified structured/unstructured framework and the limited number of third-party libraries greatly facilitate usability for the end user.

PFLOTRAN serves as the multi-physics simulation engine of the GDSA Framework (Figure 1-1). As such, PFLOTRAN has been developed to model various components of the radionuclide source term such as waste form inventory and waste form degradation, radioactive isotope decay and ingrowth, and radionuclide release. These are coupled to the flow and transport solvers which then can model several processes including multiphase non-isothermal advection, diffusion, and dispersion through porous media in either a single- or multi-continuum formulation while considering chemical reactions and isotope decay/ingrowth in the pore system. The flow and transport models ultimately feed a biosphere model which can be used to estimate dose. This report details the various components of the source term, flow, and transport models that have been enhanced this year. The new functionality described here is currently available in the master version of the code and is documented at doc-dev.pflotran.org unless otherwise stated.

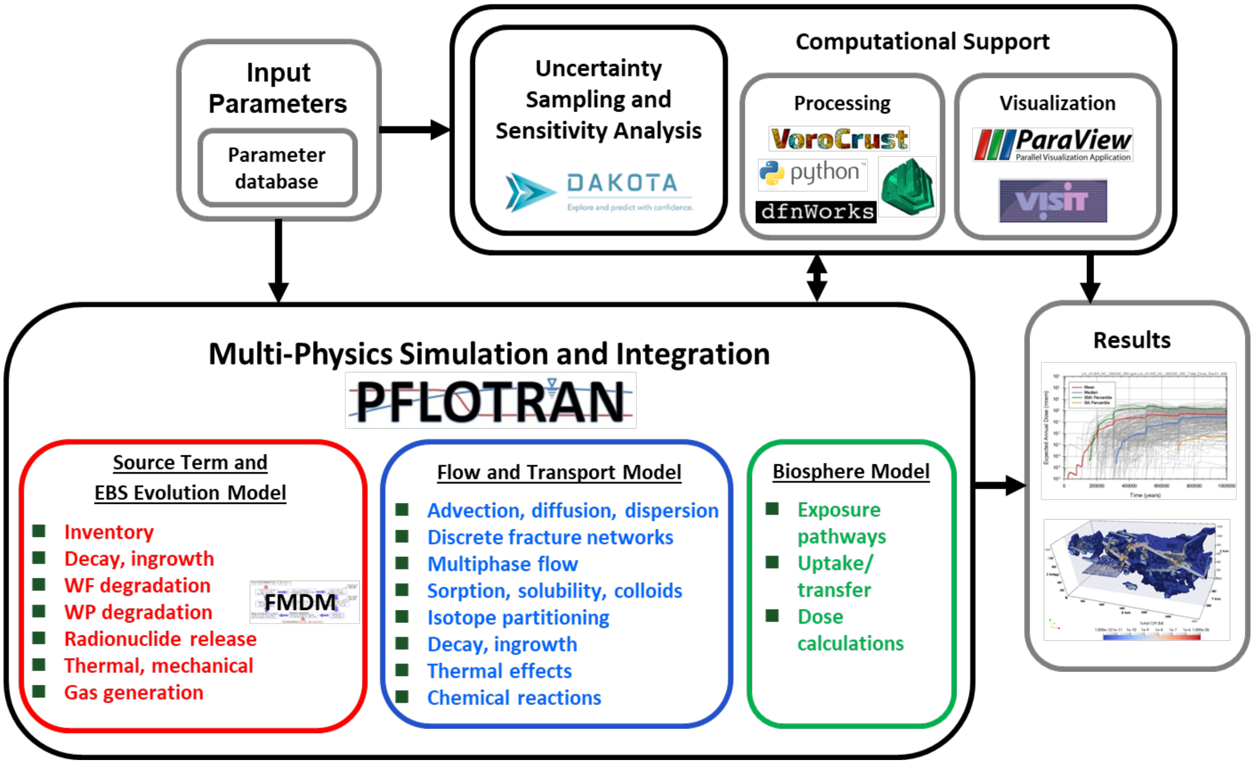

Figure 1-1 PFLOTRAN is the multi-physics simulation engine of the GDSA Framework (Mariner et al., 2020)

The generic geologic disposal system conceptual model consists of a series of layers at progressively greater distance from the radioactive waste form (Figure 1-2). The waste forms themselves and their containers (waste packages) constitute source terms of heat and radionuclides in this conceptual model. The near field is composed of the Engineered Barrier System (EBS) buffer/backfill and seals/liner as well as the disturbed rock zone (DRZ) portion of the natural barrier system (NBS). The far field consists of the host rock (NBS), and beyond that the biosphere constitutes the receptor. This conceptual model forms the basis by which new process models are characterized, implemented in the code, and tested for use in GDSA applications.

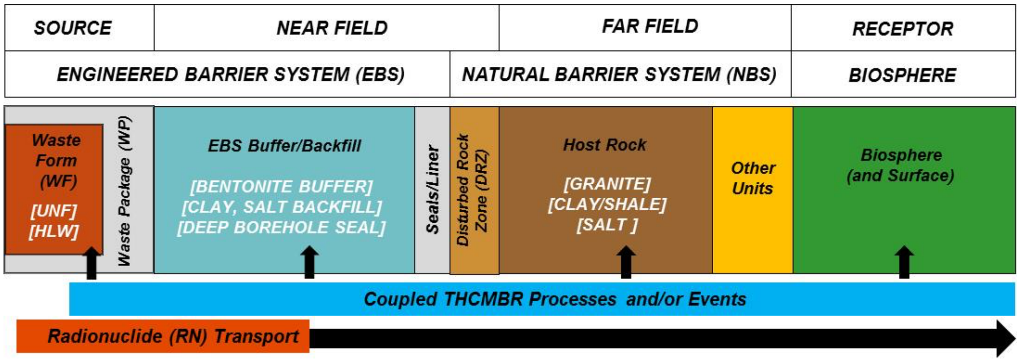

Figure 1-2 Schematic diagram of the conceptual model framework of a generic geologic disposal system (Mariner et al., 2020)

# 2. PFLOTRAN DEVELOPMENT

## 2.1 Software Infrastructure

### 2.1.1 Jira

Over the past year, the PFLOTRAN development team has adopted an Agile framework for code development which is meant to facilitate more efficient and transparent code development. Using the Atlassian Jira issue and project tracking software, the team has been working in 2-week "sprints" where individual team members have specific sets of issues (which encompass bugs and general development tasks) to which they are assigned. For the rest of Section 2.1.1, use of the word "issue" refers to the definition specific to the Jira software framework. The issues described here fall into 5 general categories:

- Epic: An epic describes a significant addition to the code, such as a new flow mode or transport mode in PFLOTRAN, which encompasses multiple different interacting process models.
- Story: A story describes a single process model or set of interacting functions that produce a code feature for a narrower purpose than an Epic. Examples of stories this FY include matrix diffusion implementation for multi-continuum transport mode (Section 2.2.1), addition of thermal characteristic curves (Section 2.2.3), and new non-linear solver development (Section 2.3.3).
- Task: A task describes general code improvement and maintenance items that apply to new or existing process models. These are the smallest step toward pursuing a story, but they do not have to be associated with stories. Examples of tasks this FY include documentation of new features, adding capability to read adsorption coefficient values from datasets, optimizing solver metrics for unsaturated zone simulations, and preparing journal papers.
- Sub-task: Sub-tasks arise when more granularity is necessary for a task, but it does not make sense to split the task into multiple separate tasks. Sub-tasks encompass the same scope as tasks.
- Bug: A bug describes a piece of code that is not working as intended. Examples of bugs fixed this FY included an HDF5 error when running in parallel and convergence metrics not being recognized under certain circumstances when using new solvers.

All the issues being pursued in the current sprint are summarized graphically in a table which delineates issues by their respective phase of the development process (Figure 2-1). The first column, "To-Do" describes issues that have been selected for development but have not yet begun. These issues have been assigned developers and "story points", which are a relative metric of the time-intensiveness of a given issue. "In Progress" describes issues that are currently being worked on by a developer, but which are not yet ready to be reviewed for merging into the master branch of the code. The "Under Review" label describes issues that are under review for merging into the master branch of the code by a Senior Developer. The "Done" label describes issues that have been fully completed.

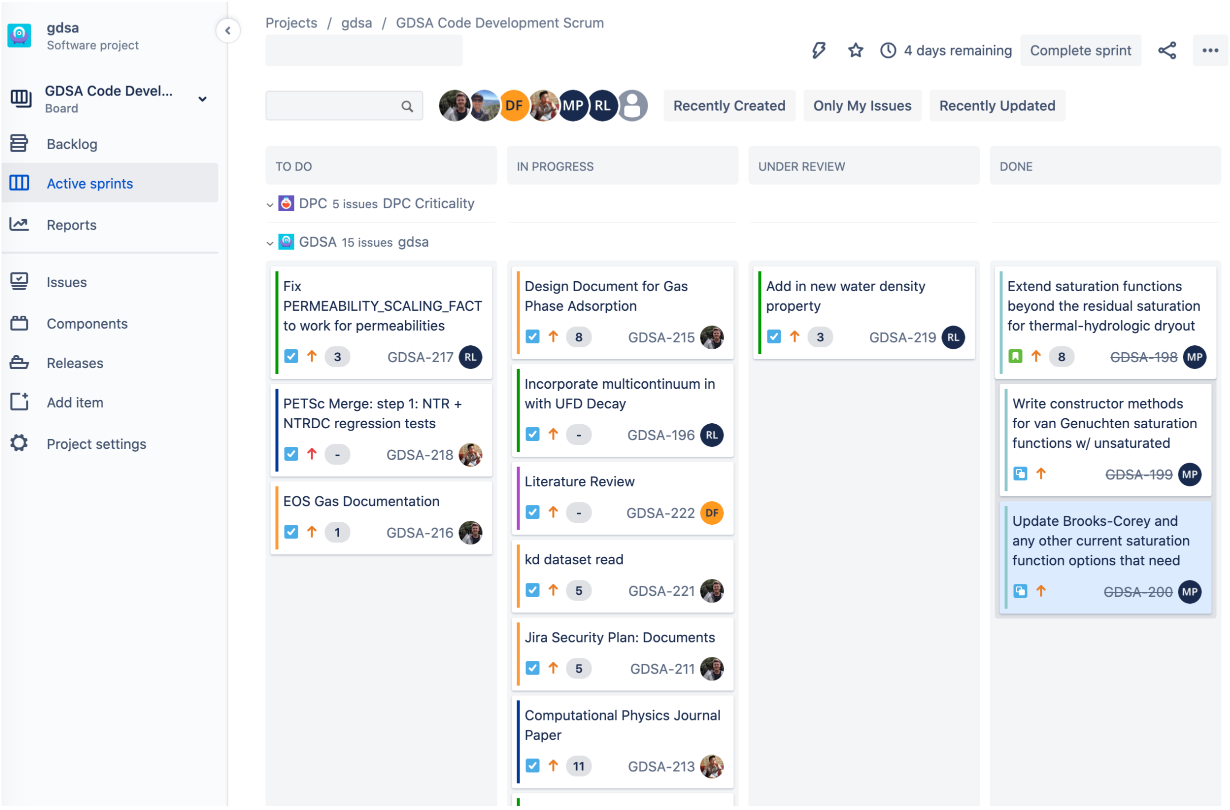

TO DO

- Fix PERMEABILITY_SCALING_FACT to work for permeabilities — 3 — GDSA-217 — RL
- PETSc Merge: step 1: NTR + NTRDC regression tests — - — GDSA-218
- EOS Gas Documentation — 1 — GDSA-216

IN PROGRESS

- Design Document for Gas Phase Adsorption — 8 — GDSA-215
- Incorporate multicontinuum in with UFD Decay — - — GDSA-196 — RL
- Literature Review — - — GDSA-222 — DF
- kd dataset read — 5 — GDSA-221
- Jira Security Plan: Documents — 5 — GDSA-211
- Computational Physics Journal Paper — 11 — GDSA-213

UNDER REVIEW

- Add in new water density property — 3 — GDSA-219 — RL

DONE

- Extend saturation functions beyond the residual saturation for thermal-hydrologic dryout — 8 — ~~GDSA-198~~ — MP
- Write constructor methods for van Genuchten saturation functions w/ unsaturated — ~~GDSA-199~~ — MP
- Update Brooks-Corey and any other current saturation function options that need — ~~GDSA-200~~ — MP

Figure 2-1 PFLOTRAN Jira Issues: Sprint Table

The breakdown of issue categorization for the GDSA PFLOTRAN Development work scope is summarized in a pie chart in Figure 2-2. In general, the team should be pursuing significantly fewer Epics than all other types of issues. This is because Stories and Tasks can all be encompassed in an Epic. For example, if an Epic is to design a new flow mode in PFLOTRAN that uses 3 mass balances and 1 energy balance, a series of stories might describe how to implement the constitutive relationships for each balance. Those stories would have their own sets of tasks which could include a literature review of equations of state and then implementation of those equations of state in support of fulfilling a story. When necessary, sub-tasks break tasks down into smaller bites but are of the same scope as tasks. Bugs are generally independent of the Epic-Story-Task hierarchy, and they can either arise during new process model implementation or be revealed while exercising existing capabilities.

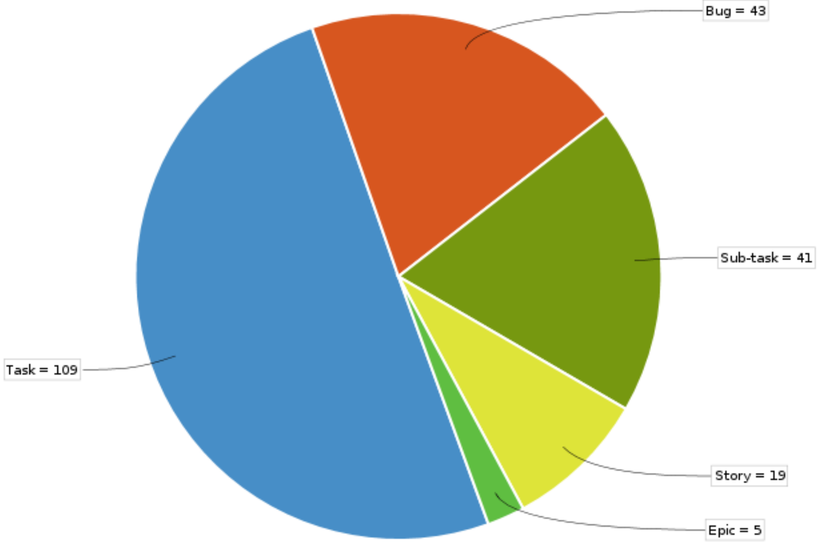

Figure 2-2 PFLOTRAN Jira Issues Separated by Category

The Agile software development format has facilitated a 2-week cycle of issue re-prioritization whereby at bi-weekly team meetings the current set of issues is compared to a backlog of issues that are ranked by priority. This backlog is ultimately maintained by the developers, but it is open to the entire GDSA team for contributions. GDSA team members are encouraged to make use of this system as a formal means for documenting bugs in the code or requesting new features with the understanding that every two weeks the current set of issues will be re-prioritized by the development team. This has facilitated a more even distribution of development work by issue category and by issue volume across the PFLOTRAN development team while also providing enhanced accountability to the GDSA PFLOTRAN user base.

New issues are continuously added to the Jira backlog either by PFLOTRAN developers or GDSA users. From June 2020 to June 2021, the number of issues logged in the Jira database increased steadily over time from just over 5 issues to 75 issues (Figure 2-3, red line) as the system has been integrated into the development and use workflow for GDSA. Correspondingly, the number of issues completed (Figure 2-3, green line) has steadily increased over time during the past year from around the same starting point to just over 60 issues, demonstrating that the PFLOTRAN developers are addressing and completing issues in a timely manner. Looking purely at number of issues completed can belie significant differences in issue rigor (e.g., story versus bug, or a story worth 1 story point versus a story worth 13 story points) or importance, so this chart should be viewed as a very rough glimpse of the timeliness of issue completion.

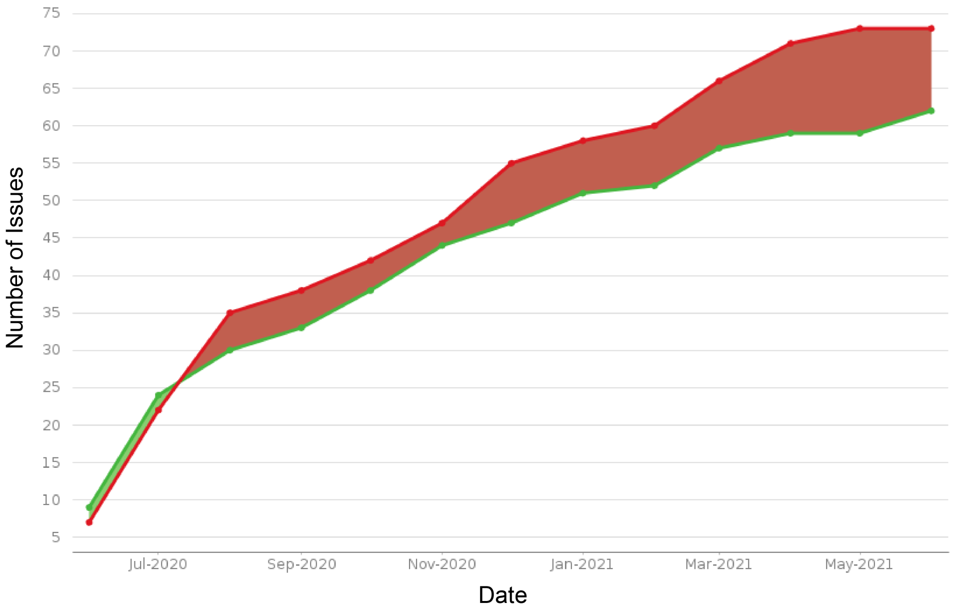

Figure 2-3 PFLOTRAN Jira Issues by date: Red = new issues, green = resolved issues

### 2.1.2 QA Test Suite

Quality Assurance (QA) is vital to establish confidence in PFLOTRAN calculations and technical requirements. In code development, QA includes performing verification studies to compare simulation outputs with other simulators, analytical solutions, or experimental data. In complex scenarios, analytical solutions may be too simple for comparison and other simulators must be used to verify results. Therefore, it is important for a QA framework to be flexible to allow comparison with multiple simulators to ensure verification across the entire code. The PFLOTRAN QA test suite has been developed to compare PFLOTRAN results with several other simulators including TOUGH3 (Jung, 2017), CrunchTope (Steefel, 2009), and TDycore (https://github.com/TDycores-Project/TDycore).

QA tests from the previous toolbox (Frederick, 2018) were updated to work with the new QA-toolbox outlined in Mariner et al. (2020) and migrated to a new GDSA-QA Git repository. Several tests were expanded on to have both time slices and observation point comparisons. In addition, two new tests were added to the GDSA-QA. The first is a multi-continuum test described in Section 2.2.1.6, the second is of a radial two-domain heating problem based on heat diffusion from a well problem presented in Dake (1978). The analytical solution is outlined in LaForce et al. (2020), and the PFLOTRAN solution uses a full 1D radial mesh solved in TH mode. The analytical solution is compared to the PFLOTRAN solution at a time slice of ~ 58 days and for observation points located at radii of 5 m, 24.9 m, 62.5 m, and 75 m (Figure 2-4).

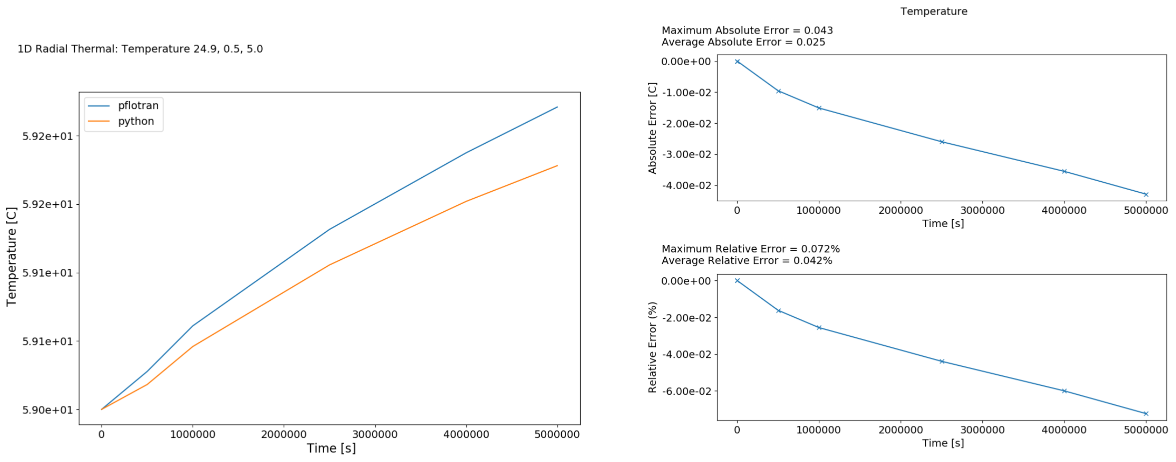

Figure 2-4 Left: Analytical (Python) vs numerical (PFLOTRAN) solution at 24.9 m. Right: absolute and relative error in the numerical solution

### 2.1.3 Computing Resources

This year, the GDSA group started using the condominium-style supercomputer Boca, which is hosted at SNL. The high-performance computing group maintains the compute nodes at SNL. Heeho Park and Rosie Leone manage the GDSA accounts and GDSA group usage. The computing cluster has a total of 128 nodes or 4608 cores of 2.6GHz Intel Xeon Gold 6240 processors with 192 GB RAM per node connected by Infiniband. Each node has 36 cores or 72 threads. There are currently more than ten active users from the GDSA group.

The current GDSA allocation includes 16 nodes (36 cores per node) which are always available to use 24/7, giving us the freedom to run medium- to large-scale simulations without queue time. PFLOTRAN scalability studies have demonstrated that optimal performance is achieved at roughly 10,000 degrees of freedom per core. Therefore, when running TH simulations which solve 2 degrees of freedom per core, our Boca allocation can allow us to optimally run simulations with 2.8 million grid cells without experiencing performance degradation. This number of cells would decrease when running with additional degrees of freedom, such as when adding chemistry or when running in GENERAL mode. Running larger simulations is possible, but users should expect more performance degradation the larger the problem becomes.

## 2.2 Process Modeling

### 2.2.1 Multi-continuum Transport

Matrix diffusion describes the diffusive migration of dissolved solutes from fluid flowing in fractures into the pore space of a rock matrix (and vice versa). Matrix diffusion can retard radionuclide transport along fracture networks in two ways: 1) it can spread radionuclides from flowing fractures into stagnant pore water and 2) the matrix provides an increase in mineral surface for geochemical surface reactions compared to fracture alone. The rate of transport in and out of the matrix can be represented by a Fickian diffusion process over a dual porosity system and is governed by several physical properties including matrix porosity, matrix diffusivity, retardation factor and local advective gradient (Winterle, 1998).

The multiple continuum model in PFLOTRAN models a secondary continuum (matrix) coupled to the primary continuum (fracture) modeled as a disconnected one-dimensional domain which is referred to as the DCDM (Dual Continuum Disconnected Matrix) model (Lichtner, 2000). Advection and diffusion are allowed in the primary continuum, and in the secondary continuum transport occurs through diffusion only. The secondary continuum is modeled as a one-dimensional domain where diffusive fluxes occur perpendicular to the fracture wall. Each primary continuum cell has a corresponding set of secondary continuum cells attached to it. The secondary cells cannot interact with secondary cells associated with other primary cells. The equations for the primary and secondary continuum are solved separately and coupled together by a mass exchange flux assuming symmetry along the axis dividing them (Iraola et al, 2019).

The multiple continuum model in PFLOTRAN has undergone several developments in the past year. Processes that have been improved and developed include sorption capabilities, dispersion in the fracture, parallel implementation, and spatial aperture discretization. Additionally, the model has been verified by several benchmark cases and model comparisons.

As an example, in PFLOTRAN the block outlined in Table 2-1 can be added in an input deck under the MATERIAL card to use the secondary continuum functionality.

Table 2-1 Sample secondary continuum input card to PFLOTRAN

| **Input** | **Description** |
|---|---|
| SECONDARY_CONTINUUM | |
| TYPE SLAB | Secondary continuum geometry |
| LENGTH 1 | Half fracture spacing [m] |
| AREA 1.0 | Fracture/matrix interfacial area per unit (bulk) volume [1/m] |
| NUM_CELLS 100 | Number of cells in secondary continuum |
| EPSILON 0.00005d0 | Fracture volume fraction |
| DIFFUSION_COEFFICIENT 1.6d-10 | Effective diffusion coefficient, includes tortuosity |
| POROSITY 0.01 | Porosity of the matrix |
| / | |

### 2.2.1.1 Sorption

Matrix diffusion coupled with sorption is currently considered one of the most important retardation factors in crystalline rock (SKBF 1983). Matrix diffusion allows for an increase in the mineral surfaces available for sorption reactions causing a retardation of radionuclides. The magnitude of sorption depends on the mineral and groundwater chemistry such as pH, temperature, and ionic strength. Sorption can be expressed through linear distribution coefficients, defined as (Freeze and Cheery 1979):

$$K_f = \frac{\text{mass sorbed}/\text{area fracture}}{\text{mass dissolved}/\text{volume water}}$$ Equation 2.2-1

Which relates to the retardation coefficient (R [-]) as (Tang et al. 1981):

$$R = 1 + \frac{K_f}{b}$$ Equation 2.2-2

Where $b$ is half the fracture aperture, and $K_f$ is the linear distribution coefficient in the fracture.

To study this effect, the sorption model implemented in the multi-continuum was developed and compared with Tang et al. (1981) as described in Section 2.2.1.6, Figure 2-8. The results show the multi-continuum model in PFLOTRAN matching up to the analytical solutions for a range of retardation factors in the matrix.

#### 2.2.1.2 Fracture properties

The secondary continuum can take on several geometries in PFLOTRAN: slab, nested cubes, sphere, or cylinder. The slab geometry has been the focus of development this past year. The slab geometry assumes symmetry along the fracture-matrix system. The system is defined using fracture volume fraction $\varepsilon_f$ [-]:

$$\varepsilon_f = \frac{\delta}{\delta + L} \qquad \text{Equation 2.2-3}$$

Where $\delta$ [m] is the half fracture aperture and $L$ is the half fracture spacing. The specific surface area (the surface area of the fracture divided by the bulk volume [1/m]), $A_{fm}$, is then specified as follows:

$$A_{fm} = \frac{1}{\delta + L} \qquad \text{Equation 2.2-4}$$

The multi-continuum model has been developed to include spatially varying fracture volume fractions in the domain. This is particularly useful in crystalline rock simulations where multiple varying fractures are present throughout the entire domain. A test case can be seen in Section 2.2.1.8 where an Equivalent Continuous Porous Medium (ECPM) is compared to a discrete fracture network (DFN) transport simulation with matrix diffusion. In the ECPM varying porosity values are calculated in each grid cell representing the amount of stochastic and deterministic fractures that intersect the grid cell. A dataset corresponding to porosity values in the domain is input using a half fracture spacing equal to half the grid cell size. More tests are currently being implemented to test this capability further.

#### 2.2.1.3 Towards Validation of PFLOTRAN Dual Continuum Model

PFLOTRAN uses a novel approach to implement the dual continuum model based on the work of Gilman (1986) and Lichtner and Karra (2014). In this approach the fracture (primary continuum) and matrix (secondary continuum) are rigorously decoupled by sandwiching the primary continuum solve between backward and forward matrix solves. This formulation is based on an effective 1D treatment of the matrix transport equations. The fracture continuum equations can be 1D, 2D or 3D. To validate the implementation of this approach in PFLOTRAN, analytical solutions presented by Tang et al. (1981) and Sudicky & Frind (1982), for fracture-matrix contaminant transport were evaluated for use as a benchmark problem within the scope of the analytical solutions.

The Tang et al. (1981) solution (hereafter referred to as Tang et al.) is restricted to a single fracture with an infinite matrix domain; whereas the solution presented by Sudicky & Frind (1982) (hereafter referred to as Sudicky & Frind) applies to an infinite set of equally spaced parallel fractures. Both approaches do not directly deal with precipitation-dissolution reactions but are restricted to radioactive decay with equal decay constants for fracture and matrix. However, it was discovered that the analytical solution presented by Sudicky & Frind does not satisfy the boundary condition imposed at the inlet as discussed in detail below. This observation is somewhat surprising given its omission in the published errata by Davis and Johnston (1984) regarding the Sudicky & Frind analytical solution.

### Equivalency of PFLOTRAN Governing Equations with Tang et al. and Sudicky & Frind

Tang et al. present an analytical solution to the governing equations for one-dimensional flow along a single fracture infinite in extent with diffusion into an infinite rock matrix perpendicular to the fracture. This model applies to PFLOTRAN only if the fracture spacing is sufficiently large that there is no interaction between neighboring fractures.

Sudicky & Frind (see errata in Davis and Johnston (1984) and Sudicky and Frind (1984)), attempted to formulate an analytical solution for equally spaced fractures with a finite matrix based on the work of Skopp and Warrick (1974). This work excludes radioactive decay and constant distribution coefficient ($K_D$) description of sorption. However, as demonstrated below, both analytically and numerically, the solution developed by Skopp and Warrick (1974) and incorporated in Sudicky & Frind fails to satisfy the boundary condition imposed at the inlet to the fracture network.

The geometry used in the Sudicky & Frind formulation is that of a platelet or slab with surface area A. The system consists of equally spaced fractures with half-fracture aperture given by the parameter $b$, and half-fracture spacing by $l$. The representative elementary volume (REV), fracture and matrix volumes are defined, respectively, as

$$V_f = Ab \qquad \text{Equation 2.2-5}$$

$$V_m = A(l - b) \qquad \text{Equation 2.2-6}$$

$$V = V_f + V_m = Al \qquad \text{Equation 2.2-7}$$

with area $A$. The fracture volume fraction $\epsilon_f$ is related to parameters $b$ and $\ell$ by

$$\epsilon_f = \frac{V_f}{V_f+V_m} = \frac{b}{\ell}. \qquad \text{Equation 2.2-8}$$

The matrix volume fraction $\epsilon_m$ is equal to

$$\epsilon_m = \frac{V_m}{V_f+V_m} = 1 - \epsilon_f, \qquad \text{Equation 2.2-9}$$

$$= 1 - \frac{b}{\ell}. \qquad \text{Equation 2.2-10}$$

The fracture and matrix equations are coupled through the specific interfacial surface area $A_{fm}$ given in terms of the parameters $b$ and $\ell$ by

$$A_{fm} = \frac{A}{V} = \frac{1}{\ell}. \qquad \text{Equation 2.2-11}$$

The inverse relations are given by

$$b = \frac{\epsilon_f}{A_{fm}} \qquad \text{Equation 2.2-12}$$

$$\ell = \frac{1}{A_{fm}} \qquad \text{Equation 2.2-13}$$

Assuming a one-dimensional fracture transport equation coupled to the matrix transport equation for fully saturated conditions the governing equations as implemented in PFLOTRAN are given by

$$\frac{\partial}{\partial t}\epsilon_f\varphi_f C_f + \frac{\partial}{\partial x}\epsilon_f\varphi_f v_f C_f - \frac{\partial}{\partial x}\left(\epsilon_f\varphi_f D_f \frac{\partial C_f}{\partial x}\right) = -A_{fm}\varphi_m\tau_m D_0 \frac{\partial C_m}{\partial y}|_{y=b} - A_{fm}\frac{\partial S_f}{\partial t} \qquad \text{Equation 2.2-14}$$

$$\frac{\partial}{\partial t}\varphi_m C_m - \frac{\partial}{\partial y}(\varphi_m\tau_m D_0 \frac{\partial C_m}{\partial y}) = -\rho_s(1-\varphi_m)\frac{\partial S_m}{\partial t} \qquad \text{Equation 2.2-15}$$

for fracture and matrix, respectively, with coordinate $x$ along the fracture and coordinate $y$ perpendicular to the fracture (gravity is not considered). The diffusion/dispersion coefficient $D_f$ for the fracture is given by

$$D_f \quad = \tau_f D_0 + \alpha_L v_f, \qquad \text{Equation 2.2-16}$$

with molecular diffusion coefficient in pure water $D_0$, tortuosity $\tau_f$ and longitudinal dispersion coefficient $\alpha_L$. Transverse dispersion is not considered. The transport equations consider advection and dispersion with sorption in the fracture coupled to diffusion and sorption in the matrix. Radioactive decay is not considered. Note that the units of the fracture and matrix sorbed phases, $S_f$ and $S_m$, are mol/m$^2$ and mol/kg, respectively.

The fracture-matrix equations are coupled through the boundary condition

$$C_m(y,t|x)|_{y=b} \quad = C_f(x,t). \qquad \text{Equation 2.2-17}$$

From symmetry considerations a zero gradient boundary condition is imposed at the matrix midpoint in the Sudicky & Frind model, or zero concentration at infinity in the Tang et al. model

$$\frac{\partial C_m}{\partial y}|_{y=\ell} = 0, \quad \text{(Sudicky \&Frind)}, \qquad \text{Equation 2.2-18}$$

$$C_m(\infty,t|x) \ = 0, \quad \text{(Tang et al.)}. \qquad \text{Equation 2.2-19}$$

The fracture equation is subject to the initial and boundary conditions

$$C_f(x,0) = \ C_\infty, \qquad \text{Equation 2.2-20}$$

$$C_f(0,t) = C_0,$$ Equation 2.2-21

$$C_f(\infty,t) = 0.$$ Equation 2.2-22

Substituting the expressions for $\epsilon_f$ and $A_{fm}$ in the fracture transport equation in terms of the parameters $b$ and $\ell$, assumed to be constant, and multiplying through by $b+\ell$ and dividing by $b$ yields the following alternative form for the fracture equation

$$\frac{\partial}{\partial t}\varphi_f C_f + \frac{\partial}{\partial x}\varphi_f v_f C_f - \frac{\partial}{\partial x}\left(\varphi_f D_f \frac{\partial C_f}{\partial x}\right) = -\frac{\varphi_m \tau_m D_0}{b}\frac{\partial C_m}{\partial y}\Big|_{x=b} - \frac{1}{b}\frac{\partial S_f}{\partial t}.$$ Equation 2.2-23

Combining this equation with the matrix equation, Eqn. 2.2-15, aside from introduction of the intrinsic fracture porosity $\varphi_f$ which is taken as one in Tang el al. and Sudicky & Frind, yields the Tang et al. and Sudicky & Frind governing equations for the fracture-matrix system of equations.

### Critique of Analytical Solutions

To test the analytical solutions derived by Tang et al. and Sudicky & Frind for the fracture, the analytical solutions were evaluated numerically close to the inlet and analytically in the limit $x \to 0$. The matrix concentration was not tested except for the steady-state solution. The Tang et al. solution satisfied the imposed boundary condition at the fracture inlet $c_f(0,t) = c_f^0$; however, the Sudicky & Frind solution did not. Instead, it satisfies the condition $\lim_{x\to 0} c_f(x,t) = 1/2\ c_f^0$.

### Tang et al.

The Tang et al. analytical solutions presented in their Eqn. (35) for the full solution and Eqn. (42b) for $D = 0$, can be easily shown to satisfy the inlet boundary condition in the fracture. Setting $x = 0$ ($z$ in their notation) yields the result

$$c_f(0) = \frac{c_f^0}{\sqrt{\pi}}\left(\int_0^\infty e^{-\xi^2} d\xi\right)\left\{erfc\left(\lambda^{\frac{1}{2}}t\right) + erfc\left(-\lambda^{\frac{1}{2}}t\right)\right\}.$$ Equation 2.2-24

Noting that

$$\int_0^\infty e^{-\xi^2} d\xi = \frac{\sqrt{\pi}}{2},$$ Equation 2.2-25

$$erfc\left(\lambda^{\frac{1}{2}}t\right) + erfc\left(-\lambda^{\frac{1}{2}}t\right) = 2,$$ Equation 2.2-26

from the identity erfc($-x$) = 2 − erfc($x$), gives

$$c_f(0) \quad = \frac{c_f^0}{\sqrt{\pi}} \frac{\sqrt{\pi}}{2} 2 = c_f^0, \qquad \text{Equation 2.2-27}$$

in agreement with the imposed boundary condition at the inlet as expected.

**Sudicky & Frind**

First the steady-state case is considered followed by the transient solution for advection-diffusion/dispersion. It is demonstrated that in the latter case the inlet boundary condition is not satisfied, even though for sufficiently large fracture spacing the Tang et al. and Sudicky & Frind solutions should agree with one another.

*Steady-State Solution*

The steady-state Sudicky & Frind analytical solutions for fracture and matrix are given by

$$c_{ss}(x) = c_0 \exp\left\{ \nu x \left[ 1 - \left( 1 + \frac{4}{\gamma}(1+\beta) \right)^{\frac{1}{2}} \right] \right\}, \qquad \text{Equation 2.2-28}$$

$$c'_{ss}(y|x) = c_{ss}(x) \frac{\cosh\left[ G\lambda^{\frac{1}{2}}(B-y) \right]}{\cosh\left[ \sigma\lambda^{\frac{1}{2}} \right]}, \qquad \text{Equation 2.2-29}$$

where the various parameters appearing in the above equations are defined by

$$\nu = \frac{v}{2D}, \qquad \text{Equation 2.2-30}$$

$$\gamma = \frac{v^2}{\lambda D R}, \qquad \text{Equation 2.2-31}$$

$$\beta = \frac{\theta (R' D')^{1/2}}{\lambda^{1/2} b R} \tanh\left[ \sigma \lambda^{\frac{1}{2}} \right], \qquad \text{Equation 2.2-32}$$

$$\sigma = G(B-b), \qquad \text{Equation 2.2-33}$$

$$G = \sqrt{\frac{R'}{D'}}. \qquad \text{Equation 2.2-34}$$

Evaluating the steady-state solution for the fracture at the boundary $x = 0$ yields $c_{ss}(0) = c_{ss}^0$. The matrix solution in this case can also be evaluated yielding $c'_{ss}(b, x) = c_{ss}(x)$. Thus, the Sudicky & Frind solution is consistent with the imposed boundary conditions for fracture and matrix under steady-state conditions.

*Transient: Advection/Diffusion/Dispersion*

The fracture concentration for advection and diffusion/dispersion involves a double integral over $\xi$ and $\epsilon$ (Sudicky & Frind, 1984):

$$c(x,t) = c_0 \frac{2}{\pi^{\frac{3}{2}}} \exp\,(\nu x) \int_{l(x)}^{\infty} \exp\left[-\xi^2 - \frac{\nu^2 x^2}{4\xi^2} - \frac{R\lambda x^2}{4D\xi^2}\right] \times \int_0^{\infty} \frac{\epsilon}{\lambda^2 + \frac{\epsilon^4}{4}} \exp(\epsilon_{\mathrm{R}}) \left\{ e^{-\lambda T} \left[\frac{\epsilon^2}{2} \sin(\epsilon_I) - \cos(\epsilon_I)\right] + \frac{\epsilon^2}{2} \sin(\Omega) - \cos(\Omega) \right\} d\epsilon d\xi, \qquad \text{Equation 2.2-35}$$

where the following additional quantities are defined

$$l = \frac{x}{2} \left(\frac{R}{Dt}\right), \qquad \text{Equation 2.2-36}$$

$$T = t - \frac{Rx^2}{4D\xi^2}, \qquad \text{Equation 2.2-37}$$

$$A = \frac{bR}{\theta (R\prime D\prime)^{1/2}}, \qquad \text{Equation 2.2-38}$$

$$\kappa = \frac{2}{v} \sqrt{RD}, \qquad \text{Equation 2.2-39}$$

$$Y = \frac{\nu^2 \kappa^2 x^2}{4A\xi^2}, \qquad \text{Equation 2.2-40}$$

$$\nu = \frac{v}{2D}, \qquad \text{Equation 2.2-41}$$

$$\epsilon_R = -\frac{\omega\epsilon}{2} \left(\frac{\sinh(\sigma\epsilon) - \sin(\sigma\epsilon)}{\cosh(\sigma\epsilon) + \cos(\sigma\epsilon)}\right), \qquad \text{Equation 2.2-42}$$

$$\epsilon_I = \frac{\epsilon^2 T}{2} - \frac{\omega\epsilon}{2} \left(\frac{\sinh(\sigma\epsilon) + \sin(\sigma\epsilon)}{\cosh(\sigma\epsilon) + \cos(\sigma\epsilon)}\right), \qquad \text{Equation 2.2-43}$$

$$\Omega = \frac{\omega\epsilon}{2} \left(\frac{\sinh(\sigma\epsilon) + \sin(\sigma\epsilon)}{\cosh(\sigma\epsilon) + \cos(\sigma\epsilon)}\right), \qquad \text{Equation 2.2-44}$$

$$\omega = \frac{\theta (R\prime D\prime)^{1/2} x}{bv}. \qquad \text{Equation 2.2-45}$$

The initial and boundary conditions imposed on the governing partial differential equations are given by

$$c(x, t = 0) = 0, \qquad \text{Equation 2.2-46}$$

$$c(x = 0, t) = c_0, \qquad \text{Equation 2.2-47}$$

$$c(x = \infty, t) = 0, \qquad \text{Equation 2.2-48}$$

for the fracture, and

$$c'(y, t = 0|x) = 0, \qquad \text{Equation 2.2-49}$$

$$c'(y = b, t|x) = c(x,t), \qquad \text{Equation 2.2-50}$$

$$\frac{\partial c\prime}{\partial y}(y = \ell, t|x) = 0 \qquad \text{Equation 2.2-51}$$

for the matrix.

### Inlet Boundary Condition $x = 0$

The fracture solution near the inlet is plotted in Figure 2-11 for different times along with the steady-state solution using the parameters listed in Table 2-4. As can be observed at the inlet ($x = 0$) the concentration is fixed at $1/2\, c_0$ for the transient case as confirmed analytically below. For distances further from the inlet the steady-state solution is obtained. The steady-state solution gives the correct concentration at the boundary.

At the inlet the solute concentration in the fracture is given by the expression (Sudicky & Frind):

$$c(x,t) = c_0 \frac{2}{\pi^{\frac{3}{2}}} \int_0^\infty e^{-\xi^2} d\xi \times \int_0^\infty \frac{\epsilon}{\lambda^2+\frac{1}{4}\epsilon^4} \left\{ e^{-\lambda t} \left[ \frac{\epsilon^2}{2} \sin\left(\frac{1}{2}\epsilon^2 t\right) - \lambda \cos\left(\frac{1}{2}\epsilon^2 t\right) + \lambda \right] \right\} d\epsilon, \qquad \text{Equation 2.2-52}$$

which follows from Eqn. 2.2-35. To obtain this result the following simplifications were made: $l = 0$, $Y = 0, T = t, \epsilon_R = 0, \epsilon_I = 1/2\, \epsilon^2 t$. The following integrals obtained from Mathematica, (Wolfram Research Inc., 2019, Version 12.0.0.0) are used to evaluate the fracture concentration at $x = 0$:

$$I_0 = \int_0^\infty e^{-\xi^2} d\xi = \frac{1}{2}\sqrt{\pi}, \qquad \text{Equation 2.2-53}$$

$$I_1 = \int_0^\infty \frac{\epsilon}{\lambda^2+\frac{1}{4}\epsilon^4} d\epsilon = \frac{\pi}{2\lambda}, \qquad \text{Equation 2.2-54}$$

$$I_2 = \int_0^\infty \frac{1}{\epsilon} \sin\left(\frac{1}{2}\epsilon^2 t\right) d\epsilon = \frac{\pi}{4}, \qquad \text{Equation 2.2-55}$$

$$I_3 = \int_0^\infty \frac{\epsilon^3}{\lambda^2+\frac{1}{4}\epsilon^4} \sin\left(\frac{1}{2}\epsilon^2 t\right) d\epsilon = \pi e^{-\lambda t}, \qquad \text{Equation 2.2-56}$$

$$I_4 = \int_0^\infty \frac{\epsilon}{\lambda^2+\frac{1}{4}\epsilon^4} \cos\left(\frac{1}{2}\epsilon^2 t\right) d\epsilon = \frac{\pi}{2\lambda} e^{-\lambda t}. \qquad \text{Equation 2.2-57}$$

It follows that

$$\int_0^\infty \frac{\epsilon}{\lambda^2+\frac{1}{4}\epsilon^4} \left[\frac{\epsilon^2}{2} \sin\left(\frac{1}{2}\epsilon^2 t\right) - \lambda \cos\left(\frac{1}{2}\epsilon^2 t\right)\right] d\epsilon = 0, \qquad \text{Equation 2.2-58}$$

$$\lambda \int_0^\infty \frac{\epsilon}{\lambda^2+\frac{1}{4}\epsilon^4} d\epsilon = \frac{\pi}{2}. \qquad \text{Equation 2.2-59}$$

With these results the Sudicky & Frind analytical solution at the inlet reduces to the single integral

$$c(0,t) = c_0 \frac{2}{\pi^{\frac{3}{2}}} \frac{\sqrt{\pi}}{2} \int_0^\infty \frac{\epsilon}{\lambda^2+\frac{1}{4}\epsilon^4} \left\{ e^{-\lambda t} \left[ \frac{\epsilon^2}{2} \sin\left(\frac{1}{2}\epsilon^2 t\right) - \lambda \cos\left(\frac{1}{2}\epsilon^2 t\right) \right] + \lambda \right\} d\epsilon, \qquad \text{Equation 2.2-60}$$

$$= c_0 \frac{2}{\pi^{\frac{3}{2}}} \frac{\sqrt{\pi}}{2} \left[\frac{\pi}{2}\right], \qquad \text{Equation 2.2-61}$$

$$= \frac{1}{2} c_0, \qquad \text{Equation 2.2-62}$$

which clearly disagrees with the imposed boundary condition $c(x=0,t)=c_0$, and in agreement with the numerical results.

Noting that the inlet boundary condition is independent of the decay constant $\lambda$ a simpler expression can be obtained by setting $\lambda = 0$. In this case the concentration at the inlet simplifies to

$$c(0,t) = c_0 \frac{2}{\pi^{\frac{3}{2}}} \int_0^\infty e^{-\xi^2} d\xi \int_0^\infty \frac{\epsilon}{\frac{1}{4}\epsilon^4} \left[\frac{\epsilon^2}{2} \sin\left(\frac{1}{2}\epsilon^2 t\right)\right] d\epsilon, \qquad \text{Equation 2.2-63}$$

$$= c_0 \frac{2}{\pi^{\frac{3}{2}}} \frac{\sqrt{\pi}}{2} \int_0^\infty \frac{\epsilon}{\frac{1}{4}\epsilon^4} \left[\frac{\epsilon^2}{2} \sin\left(\frac{1}{2}\epsilon^2 t\right)\right] d\epsilon, \qquad \text{Equation 2.2-64}$$

$$= c_0 \frac{2 \cdot 4}{\pi^{\frac{3}{2}}} \frac{\sqrt{\pi}}{2} \frac{1}{2} \int_0^\infty \frac{1}{\epsilon} \sin\left(\frac{1}{2}\epsilon^2 t\right) d\epsilon, \qquad \text{Equation 2.2-65}$$

$$= c_0 \frac{2 \cdot 4}{\pi^{\frac{3}{2}}} \frac{\sqrt{\pi}}{2} \frac{\pi}{8}, \qquad \text{Equation 2.2-66}$$

$$= \frac{1}{2} c_0. \qquad \text{Equation 2.2-67}$$

Again, the incorrect boundary condition at the inlet is obtained.

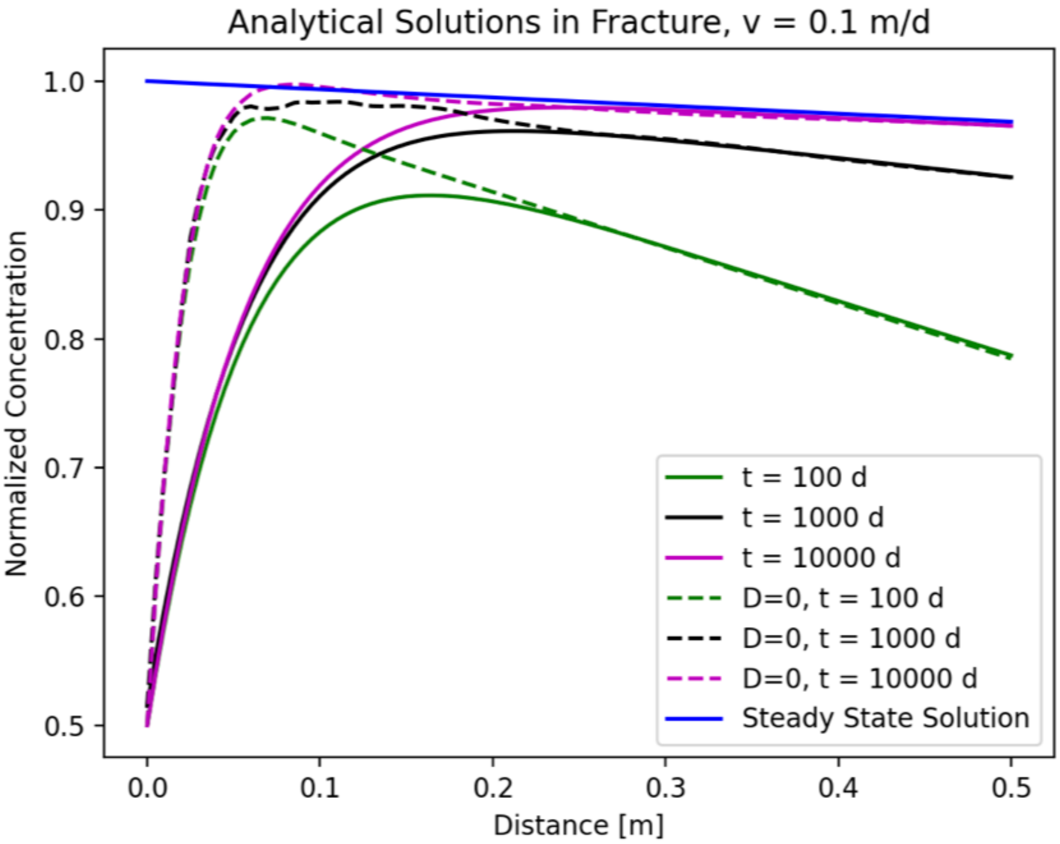

Figure 2-5 Behavior of the Sudicky & Frind analytical solution close to the inlet for the fracture concentration with (solid) and without (dashed) diffusion/dispersion plotted as a function of distance along the fracture for times of 100, 1000, and 10000 days. Transient profiles are compared with the steady-state solution. The figure demonstrates that the boundary condition at the inlet is not obeyed yielding ½ $c_0$ instead of the imposed $c_0$($c_0$=1). Values of parameters used are listed in Table 2-4.

Table 2-2 Parameter values for Sudicky & Frind example (see Figure 2-11).

| Quantity | Value |
|---|---|
| $b$ | $50 \times 10^{-6}$ m |
| $\ell$ | 0.25 m |
| $\alpha_L$ | 0.1 m |
| $D_f$ | $1.6 \times 10^{-9}$ m$^2$ s$^{-1}$ |
| $\theta$ | 0.01 |
| $\tau$ | 0.1 |
| $\lambda$ | $1.7797 \times 10^{-9}$ s$^{-1}$ |
| $v$ | 0.1 m d$^{-1}$ |
| $R_f$ | 1 |
| $R_m$ | 1 |

**Discussion**

The processes considered by Tang et al. and Sudicky & Frind consist of radioactive decay and sorption using a linear $K_D$ approximation. Precipitation/dissolution through a linear kinetic rate law is not considered. This process can be subsumed under decay, however, because the decay constant is the same for fracture and matrix this approach would lead to a significant restriction of the systems that can be described. Joshi et al. (2012) consider a more general case but solve the inverse Laplace transform numerically.

#### 2.2.1.4 Parallel Implementation

PFLOTRAN uses a highly efficient algorithm to solve the primary and secondary continuum as separate systems (Lichtner and Karra, 2014) rather than one combined system. This contrasts with the Multiple Interacting Continua (MINC) dual continuum approach used in the flow and reactive transport simulator TOUGH, where the secondary and primary are treated as a single system solved simultaneously. The primary equation is solved between forward and backward solves of the secondary continuum. Since the secondary continuum only takes information from its corresponding primary cell, this makes the PFLOTRAN multi-continuum model ideal for complex and challenging transport problems.

To further improve the efficiency of the multi-continuum model, the code has been developed and tested to be able to run in parallel on large computing architectures using multiple nodes and processing cores. A test was run with 49,685 degrees of freedom in the primary continuum for Richards flow mode and 49,685 degrees of freedom in the primary continuum for transport. Each primary node in the transport had 1,000 secondary continuum degrees of freedom. The simulation ran on 8 nodes and 288 processors and is outlined in Section 2.2.1.8. The simulation ran in ~2.5 hours demonstrating PFLOTRANs multi-continuum model ability for complex large-scale problems.

#### *2.2.1.5 DECOVALEX*

The DECOVALEX project is an international research and model comparison collaboration for advancing the understanding and modeling of coupled thermo-hydro-mechanical-chemical (THMC) processes in geological systems (decovalex.org). Task F of DECOVALEX-2023 is a new task that will focus on comparison of models and methods used for post-closure performance assessment. Members of the GDSA team at SNL are leading this effort.

Two hypothetical repositories will be modeled in Task F: one in crystalline rock and the other in salt. Over the next four years, this task promises to provide numerous opportunities for learning new modeling approaches, developing new models for use in PA simulations, testing uncertainty and sensitivity analysis methods, comparing PA methods, and networking with modelers in other programs. Additional information on the plans and status of this work is documented in LaForce et al. (2020).

The DECOVALEX Task F crystalline case has allowed for the multi-continuum model to be developed and verified by comparing the code to analytical solutions and other reactive transport models. A benchmark test for the crystalline case solving for transport in a single fracture with matrix diffusion can be seen in Section 2.2.1.6. The multi-continuum model has also been developed to allow for use with an ECPM and is planned on being used for the full-scale repository comparison.

#### *2.2.1.6 Benchmarking: Tang et al. (1981)*

The first benchmark test is based on the analytical solution by Tang et al. (1981) for the problem of transport of a radionuclide in a single fixed-aperture fracture with diffusion into the rock matrix, where the rock matrix is assumed to be infinite. The governing equations are derived from mass conservation of the radionuclide and the following assumptions are made:

1. The width of the fracture is much smaller than its length.
2. Transverse diffusion and dispersion within the fracture always assure complete mixing across the fracture width.
3. The permeability of the porous matrix is very low and transport in the matrix will be mainly by molecular diffusion.
4. Transport along the fracture is much faster than transport within the matrix.

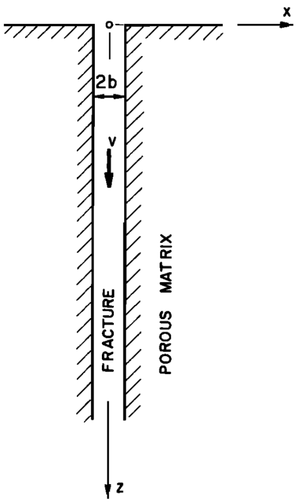

Figure 2-6 Fracture-Matrix system from (Tang et al. 1981), z represents distance along the fracture and x represents distance into the matrix.

The governing equations, as defined in PFLOTRAN, are given below (note the change in notation from the previous, more general equations):

$$\frac{\partial c}{\partial t}+\frac{v}{R}\frac{\partial c}{\partial z}-\frac{D}{R}\frac{\partial^2 c}{\partial z^2}+\lambda c+\frac{J}{bR}=0 \qquad \text{Equation 2.2-68}$$

$$\frac{\partial c'}{\partial t}-\frac{D'}{R'}\frac{\partial^2 c'}{\partial z^2}+\lambda c'=0 \qquad \text{Equation 2.2-69}$$

Where $c$, $c'$ are the concentration of solute in solution in the fracture and rock matrix respectively (M/L$^3$), $R'$ is the retardation factor in the matrix, λ is the decay constant, and z is the distance along the fracture. With *v* as average linear groundwater velocity in the fracture (L/T) and *D* is the hydrodynamic dispersion coefficient in the fracture given by:

$$D=\alpha_L v+D^* \qquad \text{Equation 2.2-70}$$

The effective diffusion coefficient, $D'$ is given by:

$$D'=\tau D^* \qquad \text{Equation 2.2-71}$$

And the diffusive mass flux *J* (M/L$^2$/T), from the fracture in the rock matrix is given by, at x = *b*:

$$J=-\phi D'\frac{\partial c'}{\partial x} \qquad \text{Equation 2.2-72}$$

Where x is the distance into the matrix. The initial conditions are given by:

$$c(z,0) = c'(x,z,0) = 0 \qquad \text{Equation 2.2-73}$$

The boundary conditions are given by:

$$c(0,t) = c_0 \qquad \text{Equation 2.2-74}$$
$$c(\infty,t) = 0 \qquad \text{Equation 2.2-75}$$

$$c'(b,z,t) = c(z,t) \qquad \text{Equation 2.2-76}$$
$$c'\,(\infty,z,t) = 0 \qquad \text{Equation 2.2-77}$$

The analytical solution is then derived in the Laplace domain. Material and fluid properties for the analytical and PFLOTRAN solution are listed in Table 2-3. The analytical solution was coded in Python for comparison.

The benchmark case is then modelled in PFLOTRAN using the slab geometry, a half fracture spacing of 1 m, and 100 secondary cells per primary cell. The analytical solution and PFLOTRAN multiple continuum model with reactive transport are compared in Figure 2-6. Comparisons are shown for along the fracture and into the matrix at a distance 2 m down the fracture. Tracer concentrations are normalized to the inlet concentration value. By 10,000 days the tracer can be seen as far as ~5-6 m down the fracture, by then the curve has almost converged on the steady state solution. The tracer penetrates to ~1 m into the matrix at 2 m down the fracture. The PFLOTRAN simulations are verified to agree between 0.1-15% relative error for relative concentrations in the fracture with higher values of relative error being associated with small relative concentrations values further along the fracture. When only looking at relative concentrations above 0.1 the greatest relative error is ~8%.

Table 2-3 Tang et al (1981) benchmark case parameters

| **Parameter** | **Value** |
|---|---|
| Diffusion coefficient in water ($D^*$) | 1.6 x $10^{-9}$ $m^2/s$ |
| Tortuosity ($\tau$) | 0.1 |
| Fracture width ($2b$) | $10^{-4}$ m |
| Dispersivity ($\alpha_L$) | 0.5 m |
| Half-life ($t_{1/2}$) | 12.35 y |
| Retardation factor in matrix ($R'$) | 1.0 |
| Retardation factor in fracture ($R$) | 1.0 |
| Matrix Porosity ($\phi$) | 0.01 |
| Concentration, $c_0$ (z=0) | 1.0 |
| Average linear velocity in fracture ($v$) | 0.01 m/d |

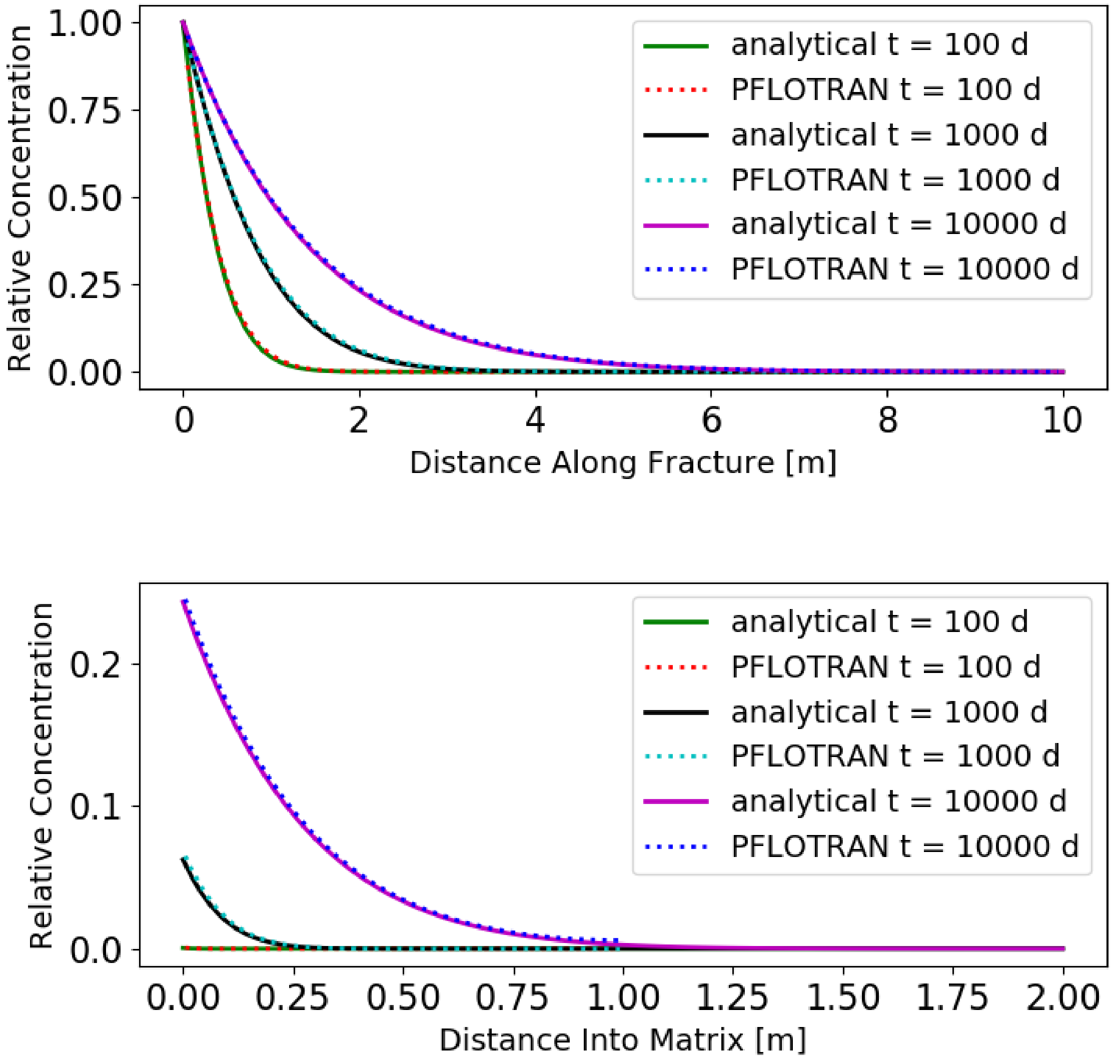

Figure 2-7 Results for concentration along fracture (top) and into the matrix (bottom) at z = 2 m down fracture.

Additionally, the benchmark case was expanded on to test varying retardation factors in the matrix. These results can be seen in Figure 2-8 at a time of 1000 days. The tracer is significantly retarded when the retardation factor is greater than one. The retardation factor in the fracture was 1.0 for all simulations. The PFLOTRAN solution agreed within 0.2-19% relative error, with the highest relative error at relative concentrations less than 0.05. These comparisons expand on Iraola et al. (2019) by adding in retardation and dispersion in the fracture.

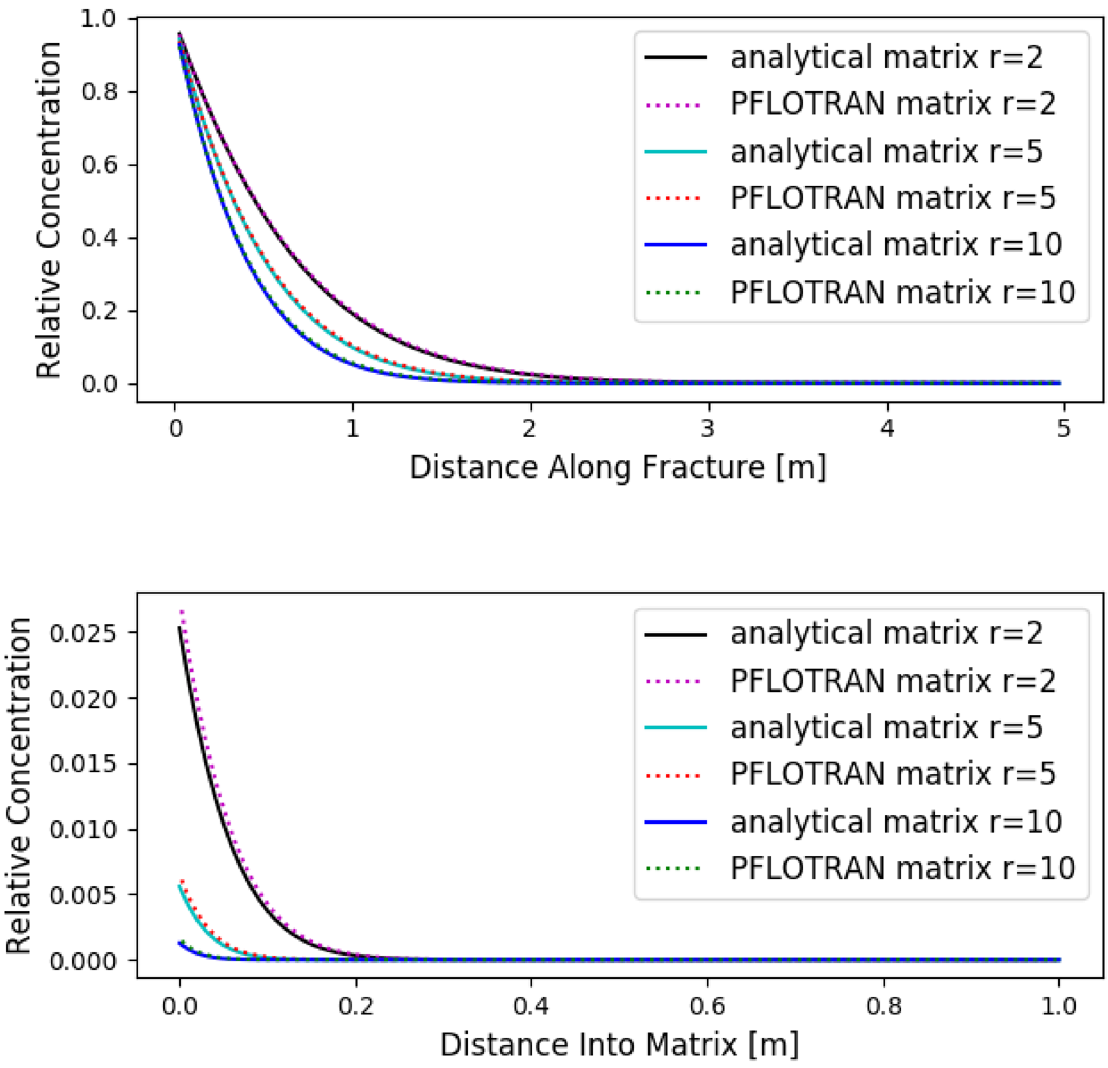

Figure 2-8 Results at 1000 days for various retardation factor along the fracture (top) and into the matrix (bottom) at a location of 2 m down the fracture.

#### 2.2.1.7 Benchmarking: Sudicky et al. (1982)

The work by Sudicky et al. (1982) describes an extension of Tang et al. (1981) of transport in discrete parallel fractures with a finite matrix domain. A benchmark case was developed to compare the solution with PFLOTRAN multi-continuum with the same parameters in Table 2-3, but two different finite matrix lengths were tested. A small matrix size of 0.05 m and a larger matrix of 0.25 m were tested. The results are shown in Figure 2-9, observation points are plotted along various distances down the fracture. For the small matrix size, one meter down the fracture the relative concentration reaches a constant value of ~0.84 around ~4000 days. Two meters down the fracture, the relative concentration reaches ~0.72 around

~5000 days. Three meters down the fracture, the relative concentration reaches a value of ~0.6 around ~6000 days. For the larger matrix, relative concentrations are still rising at 10000 days. The solutions begin to converge to a constant value at a relative concentration of ~0.6 one meter down the fracture, ~0.34 two meters down the fracture, and ~0.18 three meters down the fracture. The results show strong agreement with the analytical solution differing by a relative error less than 5%, the relative error then decreases as time increases in the simulation.

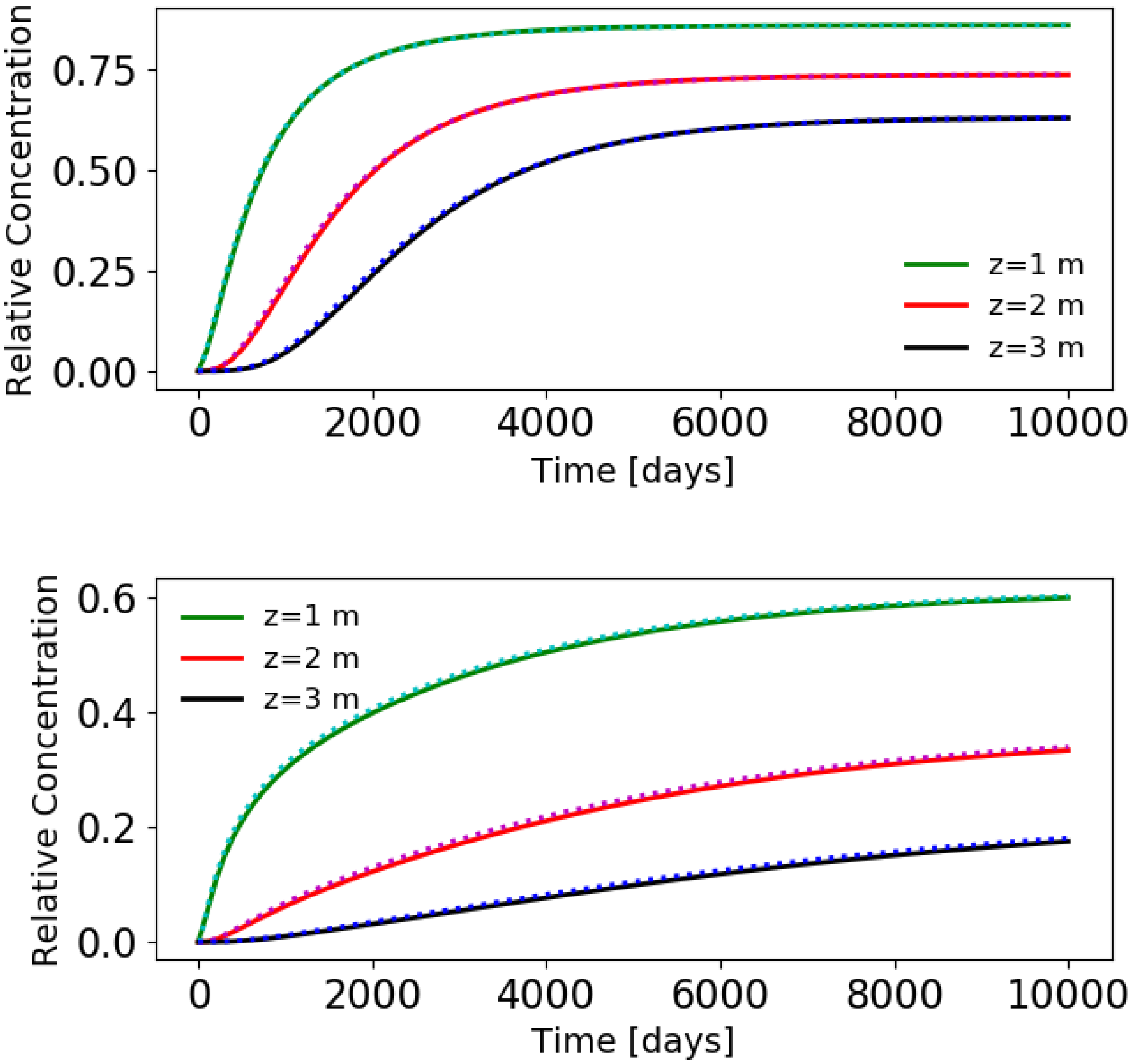

Figure 2-9 Breakthrough curves for small matrix of 0.05 m (top) and large matrix size of 0.25 m (bottom). Z values represent meters down the fracture. Solid lines represent the analytical solution and dotted lines represent the PFLOTRAN solution.

#### 2.2.1.8 Transport in a 4-Fracture plus Stochastic Fracture DFN

A benchmark case was developed to demonstrate the capability of defining spatially varying fracture properties across a domain. The test problem consists of four deterministic fractures and stochastic fractures generated based on Central Hydraulic Unit West (CHUW) Case A distributions from Posiva WR 2012-42 (Hartley et al. 2012, Table D-4) corresponding to Depth Zone 4, which applies at repository depth (Hartley et al. 2016, Table 3-1). The fractures were generated using Los Alamos National Laboratories (LANL) dfnWorks (Hyman et al. 2015) software where the deterministic fractures were built on an example in dfnWorks and upscaled to a 1 km cubic domain. A steady state flow field solution was solved with PFLOTRAN. Figure 2-10 shows the fracture domain pressure solution used for the transport simulations.

Groundwater flow is simulated by a steady state (saturated, single-phase) flow driven by a pressure gradient along the x-axis. A three-dimensional one km cubic domain was chosen. Constant pressure (Dirichlet) boundary conditions were applied on the inflow and outflow faces. An initial pulse of tracer was inserted uniformly along the fractures on the west face (x = -500) of the domain at time zero; the concentration at the west face was set to zero for all other times. The tracer exits the domain through the fractures on the east face (x = 500). All other faces were assigned no flow boundary conditions. Diffusion into the matrix occurs along the fractures. Table 2-3 shows material and fluid properties that were applied in this model. Normalized breakthrough curves (total mass that has crossed the east face divided by the initial mass at the west face) were generated at the outflow face and compared over 1000000 years.

The tracer was modeled using two different methods. First, LANL dfnTrans particle tracking software (Lagrangian reference frame) took the flow field and fracture information and simulated matrix diffusion via a time domain random walk (TDRW) approach. Second, PFLOTRAN using the advection-dispersion equation (Eulerian reference frame) and the multi-continuum reactive transport model (PFLOTRAN ADE). To simulate transport in PFLOTRAN, the fractures were upscaled to an Equivalent Continuous Porous Medium (ECPM) via a Python script mapDFN (Stein et al., 2017). dfnWorks outputs apertures, permeabilities, radii, the unit vector defining the normal vector to the fractures, and coordinates of the fracture center. These files along with parameters defining the domain and grid cell size for the ECPM were used as input for mapDFN. Upscaled anisotropic permeability, porosity, and tortuosity were then output based on the intersection of fractures within grid cells.

Table 2-3 includes the grid cell size used to create the ECPM for this comparison. The comparison can be seen in Figure 2 10, where the ECPM shows a similar trend to the DFN, although there are differences in the breakthrough times. The DFN with particle tracking shows an earlier breakthrough time than the ECPM, but the two solutions converge around the same time at the end of the simulation. Differences in results may be due to grid characterization, upscaling methods and fracture characterization. The ECPM modelled in PFLOTRAN may also experience more numerical dispersion than the DFN particle tracking results. More tests are being conducted to test the matrix diffusion ECPM method in PFLOTRAN further.

Table 2-4 Parameters for ECPM vs DFN matrix diffusion comparison

| **Parameter** | **Value** |
|---|---|
| Pressure (inlet x = -500) | 1.1 x $10^6$ Pa |
| Pressure (outlet, x = 500) | 1 x $10^6$ Pa |
| Porosity in fracture | 1.0 |
| Tortuosity in fracture | 1.0 |
| Matrix porosity | 0.005 |
| Matrix tortuosity | 0.2 |
| Matrix permeability | $10^{-18}$ $m^2$ |
| Diffusion coefficient in water | 1.6 x $10^{-9}$ $m^2/s$ |
| ECPM cell size | 20 m |

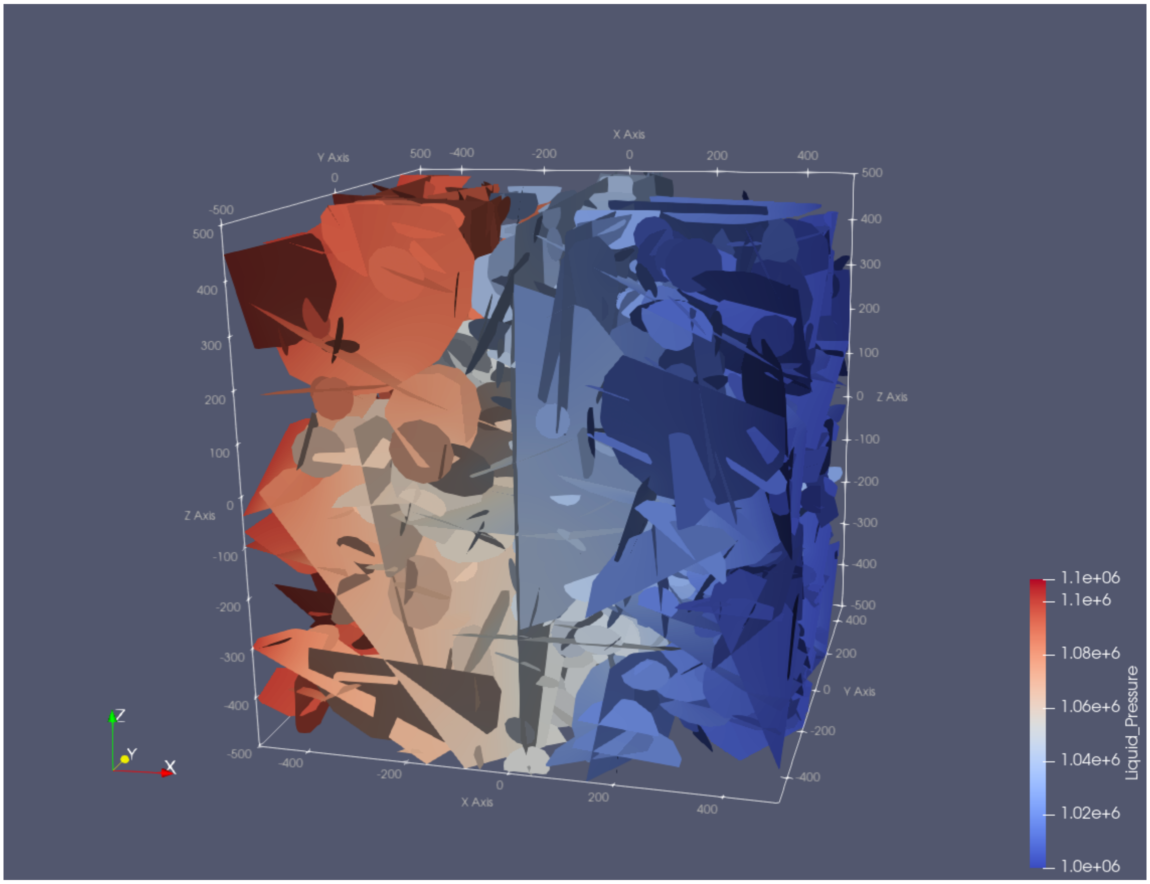

Figure 2-10 Four fracture plus stochastic fracture pressure solution

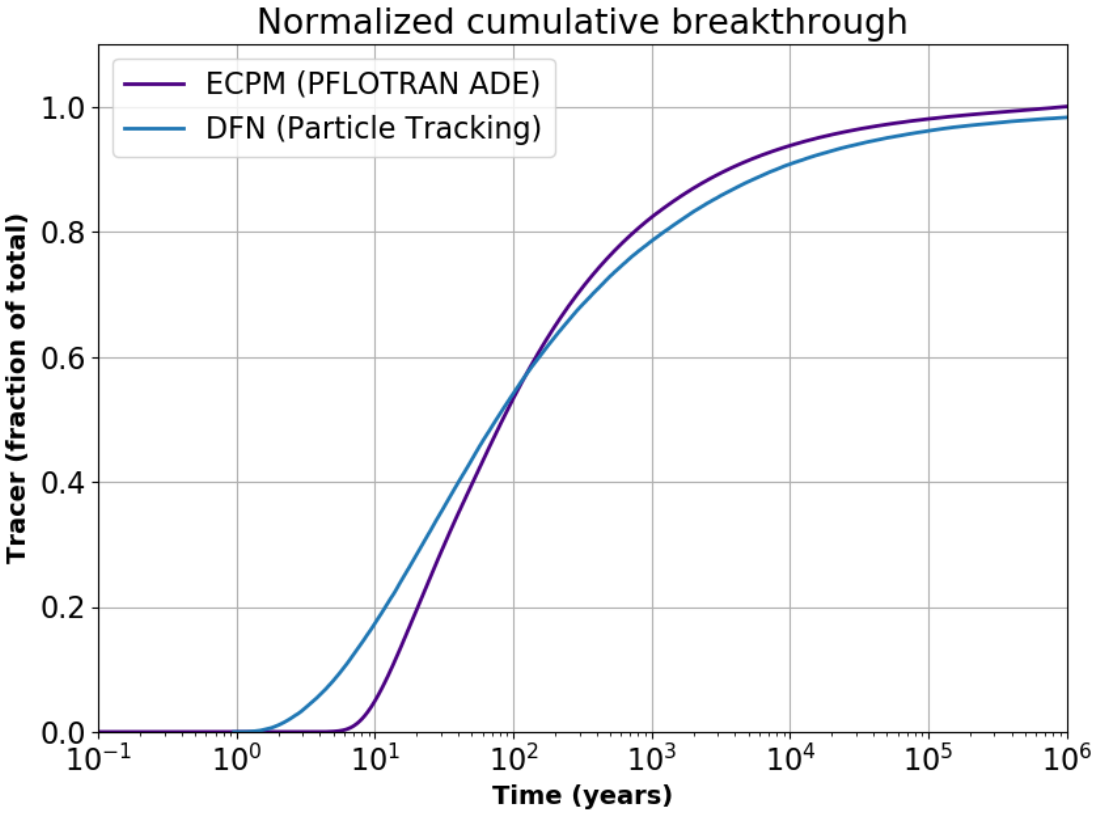

Figure 2-11 Breakthrough curve for four fractures with stochastic fracture ECPM using PFLOTRAN ADE with matrix diffusion and DFN using particle tracking with time domain random walk.

## 2.2.2 Design Document: Variable Mineral Surface Area

### *2.2.2.1 Motivation*

Precipitation and dissolution reactions of minerals with an aqueous solution are ubiquitous geochemical processes. The rate of reaction is proportional to the reactive mineral surface area and may be different for precipitation and dissolution. The surface area usually involves a distribution of grain sizes and shapes rather than a single value and is difficult to measure. Furthermore, the change in surface area with reaction is difficult to quantify. Phenomenological relations are typically employed in which the surface area is proportional to the mineral concentration raised to a power. Typically, values for the power range from zero to one. It may be used as a fit parameter or specific to crystal morphology with values 0 for constant surface area such as platy morphologies or wafer shaped geometry, 1/2 for rod shaped grains with reaction along the length of the rod, and 2/3 for cubical or spherical grains. A power of one or greater gives nonphysical results as explained below.

Difficulties implementing variable surface area arise when solving the mineral conservation equation. To the author’s knowledge, Kräutle et al. (2020) were the first to point out the ill-posed nature of incorporating variable mineral surface based on a power law relation in reactive transport equations. The difficulty appears with minerals that are initially not present in the system (secondary minerals) or minerals that have completely dissolved and later become supersaturated. Because their surface area is proportional to the mineral concentration, which becomes zero upon completely dissolving, they are unable to precipitate after becoming supersaturated.

#### 2.2.2.2 Problem Statement

Unlike sorption reactions which give rise to chromatographic separation in a column, and which generally give good agreement between models and experiment, precipitation/dissolution reactions are much more difficult to model. This is in part due to quantifying the reactive mineral surface area, the kinetic reaction rate being proportional to the surface area. Besides determining the initial mineral surface area through e.g., BET measurements, it is also necessary to quantify the evolution of surface area over time. Usually this is accomplished using a phenomenological power law relation for mineral surface area as a function of its concentration, one requirement being that the surface area must vanish as the mineral completely dissolves.

The purpose of this work is to investigate incorporation of variable mineral surface area based on a simple phenomenological power law relation in reactive transport codes. No attempt is made here to test the methodology against observation, but rather the sole purpose is to develop a mathematically consistent formulation that can account for both primary and secondary minerals as well as minerals that have completely dissolved and later in time become supersaturated.

#### 2.2.2.3 Overview of Reactive Transport Equations

A fully saturated porous medium is considered in which take place homogeneous aqueous complexing reactions and mineral precipitation and dissolution reactions. The reactions are assumed to be written in canonical form

$$\sum_j \nu_{ji} A_j \rightleftharpoons A_i, \qquad \text{Equation 2.2-78}$$

$$\sum_j \nu_{jm} A_j \rightleftharpoons M_m \qquad \text{Equation 2.2-79}$$

in terms of a set of aqueous primary species $A_j$ with stoichiometric coefficients $\nu_{ji}$ and $\nu_{jm}$. Secondary aqueous species are denoted by $A_i$ and assumed to be in local chemical equilibrium with concentrations governed by law of mass action equations. Minerals $M_m$ obey a kinetic rate law derived from transition state theory. The reactive transport equations have the form

$$\frac{\partial}{\partial t}\phi\Psi_j + \vec{\nabla}\cdot\vec{\Omega}_j \quad = -\sum_m \nu_{jm} I_m, \qquad \text{Equation 2.2-80}$$

and

$$\frac{\partial\phi_m}{\partial t} \quad = \overline{V}_m I_m, \qquad \text{Equation 2.2-81}$$

for the $j$th primary species and mth mineral conservation equation.

The various quantities appearing in these equations are defined as below. The total concentration and flux are defined as

$$\Psi_j = c_j + \textstyle\sum_i \nu_{ji}\, c_i,$$ Equation 2.2-82

$$\vec{\Omega}_j = \vec{F}_j + \textstyle\sum \nu_{ji} \vec{F}_i.$$ Equation 2.2-83

The individual species flux is given by

$$\vec{F}_l \quad = \vec{q} c_l - \phi D \vec{\nabla} c_l,$$ Equation 2.2-84

with Darcy velocity $\vec{q}$ and diffusion/dispersion coefficient $D$, in general a tensor. The concentration of $i$th secondary species in local equilibrium is derived from law of mass action

$$c_i \quad = \frac{K_i}{\gamma_i} \textstyle\prod_j (\gamma_j c_j)^{\nu_{ji}},$$ Equation 2.2-85

with equilibrium constant $K_i$, and activity coefficient $\gamma_i$. The reaction rate of $m$th mineral is based on transition state theory defined as

$$I_m = -k_m a_m (1 - K_m Q_m)\, \zeta_m,$$ Equation 2.2-86

$$Q_m = \textstyle\prod_j (\gamma_j c_j)^{\nu_{jm}},$$ Equation 2.2-87

where $Q_m$ is the activity product, $k_m$ is the rate constant and $K_m$ the equilibrium constant. The factor $\zeta_m$ is defined by

$$\zeta_m \quad = \begin{cases} 1, & \phi_m > 0 \text{ or } K_m Q_m > 1 \\ 0, & \text{otherwise} \end{cases},$$ Equation 2.2-88

and ensures that a mineral that is undersaturated but not present does not dissolve. Porosity (connected) is related to the mineral volume fractions by

$$\phi \quad = 1 - \textstyle\sum_m \phi_m\, .$$ Equation 2.2-89

#### *2.2.2.4 Variable Mineral Surface Area*

Minerals may be divided into primary minerals which are initially present in the host rock and secondary minerals which form because of reaction with the primary minerals and the aqueous solution. The change in surface area of primary minerals is typically based on a phenomenological power law relation of the form

$$a_m(\vec{r},\, t) \quad = a_m^0(\vec{r})\Big(\frac{\phi_m(\vec{r},t)}{\phi_m^0(\vec{r})}\Big)^{n_m}, \qquad \text{Equation 2.2-90}$$

where $a_m^0(\vec{r})$ and $\phi_m^0(\vec{r})$ are the initial mineral surface area and volume fraction that may be distributed spatially, for example, in a heterogeneous medium, $\phi_m(\vec{r},\, t)$ is the mineral volume fraction at time $t$ and position $\vec{r}$, and $n_m$ is an exponent. For secondary minerals this relation is not applicable since in this case $\phi_m^0 = 0$. Instead, the surface area is assumed to obey the relation

$$a_m \quad = \hat{a}_m\big(\phi_m(\vec{r},\, t)\big)^{n_m}, \qquad \text{Equation 2.2-91}$$

where $\hat{a}_m$ is a user specified constant with dimensions of specific surface area m$^2$/m$^3$. For a primary mineral $\hat{a}_m$ is related to the initial surface area by the equation

$$\hat{a}_m = a_m^0(\phi_m^0(\vec{r}))^{-n_m}. \qquad \text{Equation 2.2-92}$$

If a primary mineral completely dissolves at some location it is treated as a secondary mineral at that location and can precipitate if it later becomes supersaturated.

Explicitly incorporating Eqn. 2.2-91 for the surface area in the mineral conservation equation yields the expression

$$\frac{\partial\phi_m}{\partial t} \quad = \overline{V}_m\hat{a}_m(\phi_m)^{n_m}\hat{I}_m. \qquad \text{Equation 2.2-93}$$

where the reduced reaction rate $\hat{I}_m$ with units mol/m$^2$/s normalized to unit surface area is introduced given by

$$\hat{I}_m \quad = -k_m(1 - K_m Q_m)\, \zeta_m. \qquad \text{Equation 2.2-94}$$

It is a function of the primary species free-ion concentrations through the activity product $Q_m$. Generally, a prefactor accounting for the dependence of the rate on e.g., pH is also present but not included here for simplicity.

As pointed out by Kräutle et al. (2020) this formulation of the mineral conservation equation presents a problem in that the solution is not unique. One possible solution to this equation is $\phi_m \equiv 0$ if the mineral is supersaturated but is initially not present and therefore has zero surface area. This can be seen directly from the sequential finite difference form of Eqn. 2.2-93 formulated in terms of the reduced reaction rate at the new time step (a known quantity) and the mineral concentration at the previous time step to give:

$$\phi_m^{k+1} = \phi_m^k + \overline{V}_m \hat{a}_m (\phi_m^k)^{n_m} \hat{I}_m^{k+1} \Delta t_{k+1} \qquad \text{Equation 2.2-95}$$

It follows that if a mineral with $0 < n_m < 1$ is supersaturated ($I_m^{k+1} > 0$), and the mineral is not present at the preceding time step so that $\phi_m^k = 0$, then $\phi_m^{k+1} = 0$, and it is not possible for the mineral to precipitate even though it is supersaturated. The resolution to this issue is presented in the next section following the work of Kräutle et al. (2020).

### *2.2.2.5 Mineral Mass Transfer Equation*

**Integrated Form**

An explicit expression for the mineral concentration in terms of an integral over time of the reduced reaction rate can be obtained by writing the mineral mass transfer equation in the form

$$(\phi_m)^{-n_m} \frac{\partial \phi_m}{\partial t} = \overline{V}_m \hat{a}_m \hat{I}_m, \qquad \text{Equation 2.2-96}$$

where the power-law relation of the volume fraction has been moved to the left-hand side of the equation using separation of variables with $0 \leq n_m < 1$. Writing Eqn. 2.2-96 in differential form

$$d(\phi_m)^{1-n_m} = (1 - n_m)\overline{V}_m \hat{a}_m \hat{I}_m dt, \qquad \text{Equation 2.2-97}$$

and integrating over a time step $\Delta t$ gives the result

$$(\phi_m^{t+\Delta t})^{1-n_m} = (\phi_m^t)^{1-n_m} + (1 - n_m)\overline{V}_m \hat{a}_m \int_t^{t+\Delta t} \hat{I}_m(t')dt'. \qquad \text{Equation 2.2-98}$$

Solving for $\phi_m^{t+\Delta t}$ then yields the equation

$$\phi_m^{t+\Delta t} = [(\phi_m^t)^{1-n_m} + (1 - n_m)\overline{V}_m \hat{a}_m \int_t^{t+\Delta t} \hat{I}_m(t')dt']^{1/(1-n_m)}. \qquad \text{Equation 2.2-99}$$

For sufficiently small time steps $\Delta t$ such that

$$\int_t^{t+\Delta t} \hat{I}_m dt' \approx \hat{I}_m \Delta t, \qquad \text{Equation 2.2-100}$$

the reduced reaction rate can be pulled outside the integral to give

$$\phi_m^{t+\Delta t} = [(\phi_m^t)^{1-n_m} + (1-n_m)\overline{V}_m \hat{a}_m \hat{I}_m^{t+\Delta t} \Delta t]^{1/(1-n_m)}.$$ Equation 2.2-101

In this form of the mineral mass transfer equation if $\phi_m^k = 0$ and the mineral becomes supersaturated on the $k+1$st step, a generally nonzero result is obtained for $\phi_m^{k+1}$

$$\phi_m^{t+\Delta t} = [(1-n_m)\overline{V}_m \hat{a}_m \hat{I}_m^{t+\Delta t} \Delta t]^{1/(1-n_m)}.$$ Equation 2.2-102

Recall by assumption that $\hat{I}_m^{t+\Delta t} > 0$ and $0 \leq n_m < 1$. Finally, the updated porosity at the $k+1$st time step is obtained as

$$\phi^{k+1} = 1 - \sum_m \phi_m^{k+1}.$$ Equation 2.2-103

The porosity is a function of the free-ion primary species concentrations through the reduced reaction rate $\hat{I}_m^{k+1}$. In addition, changes in permeability and tortuosity are often related phenomenologically to powers of the porosity not considered further here. In Appendix A the effect of variable porosity for a single component system with first-order kinetics in a batch reactor is considered.

For the case $n_m = 1$ it follows that

$$\frac{\partial \phi_m}{\partial t} = \lambda_m \phi_m,$$ Equation 2.2-104

where $\lambda_m > 0$ for precipitation, $< 0$ for dissolution, and $= 0$ at equilibrium, is defined by

$$\lambda_m = \overline{V}_m \hat{a}_m \hat{I}_m.$$ Equation 2.2-105

The solution over a time step is given by

$$\phi_m^{k+1} = \phi_m^k e^{\lambda_m \Delta t}.$$ Equation 2.2-106

Accordingly, if $\phi_m^k = 0$, then it follows that $\phi_m^{k+1} = 0$ at the new time step, even if the mineral in question is supersaturated. Consequently, $n_m = 1$ is not a physically meaningful value. In general, for $n_m > 1$ a singularity occurs if the mineral concentration vanishes.

### Change of Variable

An alternative derivation of the mineral conservation equation was presented by Kräutle et al. (2020). These authors noticed that if a change of variable $\phi_m \rightarrow \xi_m$ is carried out by defining

$$\xi_m(\vec{r},t) \quad = (\phi_m(\vec{r},t))^{1-n_m}, \qquad \text{Equation 2.2-107}$$

at position vector $\vec{r}$ and time $t$, the factor $(\phi_m)^{n_m}$ appearing in the mineral conservation equation is eliminated and the constant surface area equation is retrieved within a factor of $1 - n_m$. Taking the time derivative of $\xi_m$ as defined above and substituting Eqn. 2.2-93 for $\partial\phi_m / \partial t$ yields

$$\frac{\partial\xi_m}{\partial t} = (1-n_m)(\phi_m)^{-n_m}\frac{\partial\phi_m}{\partial t}, \qquad \text{Equation 2.2-108}$$

$$= (1-n_m)(\phi_m)^{-n_m}\overline{V}_m\hat{a}_m(\phi_m)^{n_m}\hat{I}_m, \qquad \text{Equation 2.2-109}$$

$$= (1-n_m)\overline{V}_m\hat{a}_m\hat{I}_m, \qquad \text{Equation 2.2-110}$$

where in the latter expression the mineral volume fraction factor has been eliminated. Integrating over a time step then gives

$$\xi_m^{k+1} = \xi_m^k + (1-n_m)\overline{V}_m\hat{a}_m\int_t^{t+\Delta t}\hat{I}_m\,dt', \qquad \text{Equation 2.2-111}$$

$$\approx \xi_m^k + (1-n_m)\overline{V}_m\hat{a}_m\hat{I}_m\Delta t, \qquad \text{Equation 2.2-112}$$

valid for sufficiently small $\Delta t$. The inverse transformation is given by

$$\phi_m \quad = \xi_m^{1/(1-n_m)}. \qquad \text{Equation 2.2-113}$$

The porosity follows directly from the equation

$$\phi \quad = 1 - \sum_m \xi_m^{1/(1-n_m)}. \qquad \text{Equation 2.2-114}$$

### 2.2.2.6 Implementation in PFLOTRAN

Two approaches are feasible for implementing precipitation/dissolution reactions in PFLOTRAN: sequentially coupled solute transport and reaction and the mineral mass transfer, or fully coupled. Sequential coupling is the current approach used in PFLOTRAN with explicit finite difference for the solution of the mineral mass transfer equation based on Eqn. 2.2-95. Justification is based on the generally relatively slow change in solid concentration compared to the change in aqueous concentration resulting in formation of a stationary state—although this is not always the case. However, as demonstrated above this implementation is not adequate for describing precipitation with variable surface area. The sequential coupling approach would be the easiest to implement as it is similar to what is already done in PFLOTRAN involving replacing $\phi_m$ by the variable $\xi_m$ introduced by Kräutle et al. (2020).

In the fully coupled approach it is proposed to update the mineral concentration, tortuosity and porosity (and in problems involving flow, permeability) in PFLOTRAN according to the revised algorithm introduced above using the new variable $\xi_m$. The mineral volume fractions would be updated simultaneously with the solution to the solute transport equations using finite volume discretization with fully implicit or operator splitting time stepping.

It should be noted that:

- Different surface areas may be required in describing dissolution of a primary mineral and its precipitation after completely dissolving.
- The mineral surface area parameter $\hat{a}_m$ is somewhat arbitrary and ideally would be determined as a fit parameter. However, as the surface area increases the reaction rate approaches local equilibrium thereby becoming independent of the surface area.
- Negative mineral concentrations can result during dissolution when using the sequentially coupled approach as occurs in PFLOTRAN with the current implementation. This can lead to loss of mass during the simulation.

### 2.2.3 Thermal Characteristic Curves

New developments in thermal modeling were driven by a desire to broaden insight into post-closure criticality consequences by accommodating several phenomena affecting the dynamic temperature field between multiple emplacements of hot waste packages. These developments take a generalized form in thermal characteristic curves, which are extendable classes of thermal conductivity relationships relating state variables like temperature or water saturation to thermal conductivity.

PFLOTRAN now includes saturation- and temperature-dependent thermal conductivity by way of thermal characteristic curves (TCCs). This functionality was added to impart higher modeling fidelity for scenarios where significant thermal loading can lead to localized temperature anomalies in a repository. Heat dissipation is linked to the overall thermal conductivity, which can vary locally if there is significant local contrast in the temperature field and strong temperature dependence.

Additionally, consequence analysis of in-package criticality events occurring after direct disposal is an active area of research. During a criticality event, a local power spike in the waste form could result in significant perturbation to the local temperature field. Accurately capturing the capacity for the repository-host rock system to dissipate heat also affects material and geochemical properties that are temperature-dependent and potentially irreversible. With the heat emission from a critical event in the canister, the mineral composition of the surrounding buffer is liable to be affected, which would directly affect sealing performance in the repository. Given a smectite-rich buffer and the temperature-dependence of the smectite-to-illite (S-I) transition, it is important to have expanded thermal modeling capability to accurately represent the phenomena involved for a consequence analysis.

Internally, the use of TCCs resembles the pre-existing implementation of "characteristic curves," or combinations of capillary pressure and relative permeability functions. The liquid saturation and/or temperature of a grid cell is passed to the TCC subroutine, which is a derived-type member function selected for the functional form assigned to the material. The subroutine then evaluates thermal conductivity as well as the derivatives with respect to saturation and temperature. Extensibility from object-oriented programming allows for multiple regions in the repository to be defined by the same TCC, which replaces the specification by individual material in the previous PFLOTRAN implementation and facilitates problem construction for uncertainty analyses. The material-based assignment is backwards-compatible, but it cannot be used in the same input deck with TCCs.

The previous implementation of thermal conductivity ($\kappa_T$) for use with PFLOTRAN non-isothermal flow modes involved using wet ($\kappa_T^{wet}$) and dry ($\kappa_T^{dry}$) endpoint conductivity values in a function with saturation ($S_l$) from Somerton et al. (1974) as shown in Equation 2.2-115. In the context of the current version, this equation is still used as the default (*D*) for effective thermal conductivity.

$$\kappa_T^D(S_l) = \kappa_T^{dry} + \sqrt{S_l}\left(\kappa_T^{wet} - \kappa_T^{dry}\right) \qquad \text{Equation 2.2-115}$$

In thermo-hydrological (TH) mode, there is also an option to specify a frozen thermal conductivity ($\kappa_T^{fr}$) and related exponents ($\alpha$ and $\alpha_{fr}$) for use in the freezing sub-mode. As shown in Equation 2.2-116, the liquid saturation and ice saturation ($S_{ice}$) are used to evaluate the effective thermal conductivity in a partially unsaturated frozen medium, where $\varepsilon$ is a small number employed for numerical stability when calculating derivatives (Painter, 2011).

$$\begin{aligned}\kappa_T(S_l, S_{ice}) = {} & \kappa_T^{wet}(S_l + \epsilon)^{\alpha} + \kappa_T^{fr}(S_{ice} + \epsilon)^{\alpha_{fr}} \\ & + \kappa_T^{dry}\left[1 - (S_l + \epsilon)^{\alpha} - (S_{ice} + \epsilon)^{\alpha_{fr}}\right]\end{aligned} \qquad \text{Equation 2.2-116}$$

In the previous version of the code, for a given problem thermal conductivity parameters were specified by material property along with heat capacity and density, but there were no additional parameters to determine temperature-dependence. The new implementation creates flexibility to parameterize thermal conductivity as a function of other state variables, like temperature. Regardless, the effective thermal conductivity between two cells is applied at cell interfaces by computing a harmonically averaged thermal conductivity between the two cells. This average value is then used with the temperature difference between cells to evaluate the heat flux and, depending on the phases involved, the derivative of energies with respect to temperature and saturation.

In the new TCC feature, the standard function types employed to evaluate $\kappa_T$ are shown in Table 2-5. In most cases, a call to a temperature-dependent thermal conductivity function results in the evaluation of Equation 2.2-115 to determine saturation dependence and then calculate a temperature-dependent function using that result. The only exceptions are the constant TCC (Equation 2.2-117), which is neither saturation nor temperature dependent, and the frozen TCC, which has modified saturation dependence.

The constant TCC can be advantageous for uncertainty studies that need to isolate certain phenomena. For example, in a criticality consequence study, a close examination of intermittent water exfiltration from a flooded dual-purpose canister (DPC), would benefit from a buffer modeled with a constant $\kappa_T$. This would reduce temperature-driven effects in the material surrounding the DPC to isolate heat-emission effects on the water content. The function can also be used for engineered components that are not expected to exhibit strong variations in thermal conductivity with the expected temperature range.

The linear resistivity TCC (Equation 2.2-118) assumes that the reciprocal of thermal conductivity can be modeled as a linear function with temperature. This form was suggested by Birch and Clark (1940) and fitted empirically by Blesch et al. (1983) for granite, basalt, shale, and salt. The latter study was a far-field thermal analysis of a repository that intended to evaluate environmental impact based on temperature changes in various regions. In the linear resistivity function, $a_1$ is the resistivity shift parameter and $a_2$ is the scaling factor with the change in temperature. The temperature change is defined with respect to a reference temperature ($T_{ref}$), such that when $T_{ref} = 0$ °C, $\kappa_T^{dry}$ and $\kappa_T^{wet}$ are assumed to be evaluated at 0 °C as well.

The cubic polynomial TCC (Equation 2.2-119) adds three orders of temperature dependence to $\kappa_T$ and includes a reference temperature $T_{ref}$ with a default of 0°C. This polynomial form was used by Flynn and Watson (1969) to evaluate effective thermal conductivity in soils reaching temperatures up to 1,700 °C. This study was conducted in the context of reentry and earth-impact scenarios for space vehicles containing radioisotopes, and the soils that were sampled included limestone, granitic detritus, sand, and others within a particle diameter of 1.7 mm. The order of polynomial was chosen to reduce the residuals in a least-squares fit of test data. Third-order least squares polynomial fits were also used to describe effective thermal conductivities for BWR and PWR assemblies in Yucca Mountain studies (TRW Environmental Safety Systems 1996). A cubic polynomial can be applied to rock and buffer regions near a waste form susceptible to being affected by high temperature transients, or perhaps to regions intended to model spent nuclear fuel (SNF) assemblies. Laboratory analyses of salt samples from WIPP showed strong temperature dependence of thermal conductivity with an applied heat flux (Kuhlman et al. 2020). The $\kappa_T$ values decreased with temperature and appeared to conform to a cubic polynomial.

A power law TCC (Equation 2.2-120) is provided which employs an exponent ($\gamma$) and reference temperature $T_{ref}$. The default reference temperature is defined as absolute zero, or −273.15 °C, which implies $\kappa_T^{dry}$ and $\kappa_T^{wet}$ values being evaluated at 26.85 °C. The temperature change is normalized by 300 K and then raised to the exponent $\gamma$. This type of model is relevant to studies of crystals, ceramics, and engineering materials, and can be useful in characterizing heat transfer through the spent nuclear fuel, canister, and overpack.

Table 2-5 The standard thermal characteristic curve options in PFLOTRAN.

| Name | Application | Function |
|---|---|---|
| **Constant** | Non-porous media not subject to strong temperature gradients<br>Sensitivity studies | $\kappa_T = \kappa_T^C$ Equation 2.2-117 |
| **Default** | All soils not subject to strong temperature gradients | $\kappa_T^D(S_l) = \kappa_T^{dry} + \sqrt{S_l}\left(\kappa_T^{wet} - \kappa_T^{dry}\right)$ Repeat of *Equation 2.2-115* |
| **Linear Resistivity** | Host rock in far-field thermal analyses such as granite, basalt, and shale | $\kappa_T(S_l, T) = \frac{\kappa_T^D(S_l)}{a_1 + a_2(T - T_{ref})}$ Equation 2.2-118 |
| **Cubic Polynomial** | Elevated soil temperatures (e.g., high temperature transients, ground impact scenarios)<br>Backfilled SNF assemblies<br>WIPP salt | $\kappa_T(S_l, T) = \kappa_T^D(S_l) \cdot \left[1 + \beta_1(T - T_{ref}) + \beta_2(T - T_{ref})^2 + \beta_3(T - T_{ref})^3\right]$ Equation 2.2-119 |
| **Power Law** | Crystals, ceramics, and engineering materials (e.g., overpack, neutron absorbers) | $\kappa_T(S_l, T) = \kappa_T^D(S_l)\left(\frac{T - T_{ref}}{300}\right)^\gamma$ Equation 2.2-120 |
| **Frozen** | Permafrost modeling | $\kappa_T(S_l, S_{ice}) = \kappa_T^{wet}(S_l + \epsilon)^\alpha + \kappa_T^{fr}(S_{ice} + \epsilon)^{\alpha_{fr}} + \kappa_T^{dry}[1 - (S_l + \epsilon)^\alpha - (S_{ice} + \epsilon)^{\alpha_{fr}}]$ Repeat of *Equation 2.2-116* |

For backwards compatibility, a frozen TCC is defined that uses the functional forms for effective thermal conductivity in thermo-hydrologic (TH) mode (Equation 2.2-116). It is a derived type of the default TCC but utilizes an additional procedure for frozen thermal conductivity to account for ice saturation dependence. The model requires the dry and wet thermal conductivity and the exponent of the soil Kersten number α. α is defined in the base class for use by all curves (initialized as 1.0) to give the user control over flux behavior in TH mode. Frozen soil analysis requires definition of the frozen soil Kersten number exponent $\alpha_{fr}$, the frozen thermal conductivity $\kappa_T^{fr}$, and the name of the freezing model (provided in the documentation, Lichtner et al., 2018). The freezing analysis is restricted to TH mode, and when freezing is active, TCCs of the non-frozen type are not allowed. When freezing is inactive in TH mode, or when the frozen curve is used outside of TH modes, only the dry and wet components of the equation are used.

Altogether, the TCC feature was implemented with a new source code file that contained all variables and subroutines used to process TCC-related user input, evaluate effective thermal conductivity, and provide error messages. A list of inputs for the deployed TCCs are shown in Table 2-6 and an example is shown in Appendix B. The user can activate the TEST feature to print out a table of evaluated effective thermal conductivity values, along with $\frac{d\kappa_T}{dT}$ and $\frac{d\kappa_T}{dS_l}$, for a list of temperature and saturation coordinates. (Entries for ice saturation and $\frac{d\kappa_T}{dS_{ice}}$ are provided for the frozen curve.)

To preserve backwards-compatibility with PFLOTRAN v2, when the input format specifies $\kappa_T^{dry}$ and $\kappa_T^{wet}$ by material, a default TCC (Equation 2.2-115) is created and tied to these parameters. For frozen thermal conductivity in TH mode, $\kappa_T^{fr}$, $\alpha_{fr}$, and $\alpha$ are tied to a frozen curve. The legacy input format cannot be combined with the usage of TCCs in a given input file.

Table 2-6 User inputs for the standard thermal characteristic curves.

| User Input | Value(s) | Applicability |
|---|---|---|
| **THERMAL_CHARACTERISTIC_CURVES** | <name> | All |
| **THERMAL_CONDUCTIVITY_FUNCTION** | <TCC type> | All |
| **THERMAL_CONDUCTIVITY_CONSTANT** | $\kappa_T^C$ | CONSTANT |
| **THERMAL_CONDUCTIVITY_DRY** | $\kappa_T^{dry}$ | DEFAULT and below |
| **THERMAL_CONDUCTIVITY_WET** | $\kappa_T^{wet}$ | |
| **THERMAL_CONDUCTIVITY_FROZEN** | $\kappa_T^{fr}$ | FROZEN (TH mode only) |
| **KERSTEN_EXPONENT_FROZEN** | $\alpha_{fr}$ | |
| **ICE_MODEL** | <model> | |
| **KERSTEN_EXPONENT** | $\alpha$ | FROZEN |
| **REFERENCE_TEMPERATURE** | $T_{ref}$ | LINEAR_RESISTIVITY and below |
| **LINEAR_RESISTIVITY_COEFFICIENTS** | $[a_1, a_2]$ | LINEAR_RESISTIVITY |
| **CUBIC_POLYNOMIAL_COEFFICIENTS** | $[\beta_1, \beta_2, \beta_3]$ | CUBIC_POLYNOMIAL |
| **EXPONENT** | $\gamma$ | POWER |
| **END** | | |
| **TEST** | | All |
| **END** | | |

Verification of basic TCC functionality was provided in Price et al. (2020). When coupled to a temperature-dependent criticality heat source, temperature-dependent thermal conductivity will be an important mechanism for modulating the power output from a criticality event. Now that PFLOTRAN contains a flexibly structured implementation of TCCs, specialized functional forms can be added in a straightforward manner to meet the needs of process modelers studying different repository concepts.

### 2.2.4 Thermal Conductivity Anisotropy

The TCC feature accommodates directional dependence via optional anisotropy ratios. An anisotropy tensor may be specified for a TCC to modify dry and wet thermal conductivity values depending on the direction traversed in the material. This is intended to be useful for characterizing layered repository strata with different conductivity behavior, for example, in the x- and y- directions compared to the z-direction.

In addition, there is a new “composite” TCC that allows for conductivity along certain axes to be governed by separate models altogether. This was designed to accommodate the special thermal conductivity characteristics of packages containing SNF, such as a DPC, where different models are applied for the axial and radial directions to account for the lattice characteristics of the assemblies.

### 2.2.4.1 Model Development

Thermal conductivity is defined as a symmetric tensor **K** with six unique components $\kappa_{ij}$ and unit vectors $\hat{n}_i$, as shown in Equation 2.2-121.

$$\mathbf{K} = \begin{bmatrix} \kappa_{xx} & \kappa_{xy} & \kappa_{xz} \\ \kappa_{xy} & \kappa_{yy} & \kappa_{yz} \\ \kappa_{xz} & \kappa_{yz} & \kappa_{zz} \end{bmatrix} \qquad \text{Equation 2.2-121}$$

The thermal conductivity tensor relates the heat flux $\vec{q}$ to the temperature gradient ($\nabla T$ or $\vec{\theta}$**)** via Fourier's Law (Equation 2.2-122). Therefore, the component $\kappa_{xz}$ would characterize the heat flux induced in the *x* direction from the temperature gradient measured in the orthogonal *z* direction.

$$\begin{aligned} \vec{q} &= -\mathbf{K} \cdot \nabla \mathrm{T} = -\mathbf{K} \cdot \left( \frac{\partial T}{\partial x} \hat{n}_x + \frac{\partial T}{\partial y} \hat{n}_y + \frac{\partial T}{\partial z} \hat{n}_z \right) = -\mathbf{K} \cdot \left( \theta_x \hat{n}_x + \theta_y \hat{n}_y + \theta_z \hat{n}_z \right) \\ &= -\mathbf{K} \cdot \vec{\theta} \end{aligned} \qquad \text{Equation 2.2-122}$$

The directional thermal conductivity $\kappa_\theta$ is defined as the value of thermal conductivity in the direction of the gradient ( $\hat{\theta}$ ), as shown in Equation 2.2-123.

$$\kappa_\theta = \frac{\left| \vec{q} \cdot \hat{\theta} \right|}{\left| \vec{\theta} \right|} = \frac{1}{\left| \vec{\theta} \right|} \cdot \frac{\vec{q} \cdot \vec{\theta}}{\left| \vec{\theta} \right|} \qquad \text{Equation 2.2-123}$$

The heat flux is expanded in terms of the direction cosines in Equation 2.2-124, where $\phi_{\theta i}$ is the angle between $\vec{\theta}$ and $\hat{n}_i$ (where i = {x,y,z}, as exemplified in Figure 2-12) and $|\vec{\theta}|$ is the magnitude of the temperature gradient.

$$\vec{q} = -\begin{bmatrix} \kappa_{xx} & \kappa_{xy} & \kappa_{xz} \\ \kappa_{xy} & \kappa_{yy} & \kappa_{yz} \\ \kappa_{xz} & \kappa_{yz} & \kappa_{zz} \end{bmatrix} \cdot \begin{bmatrix} \left| \vec{\theta} \right| \cos \phi_{\theta x} \\ \left| \vec{\theta} \right| \cos \phi_{\theta y} \\ \left| \vec{\theta} \right| \cos \phi_{\theta z} \end{bmatrix} \qquad \text{Equation 2.2-124}$$

The result of the dot product in Equation 2.2-124 is shown in Equation 2.2-125.

$$\begin{aligned} \vec{q} = &-\left( \kappa_{xx} \left| \vec{\theta} \right| \cos \phi_{\theta x} + \kappa_{xy} \left| \vec{\theta} \right| \cos \phi_{\theta y} + \kappa_{xz} \left| \vec{\theta} \right| \cos \phi_{\theta z} \right) \hat{n}_x \\ &- \left( \kappa_{xy} \left| \vec{\theta} \right| \cos \phi_{\theta x} + \kappa_{yy} \left| \vec{\theta} \right| \cos \phi_{\theta y} + \kappa_{yz} \left| \vec{\theta} \right| \cos \phi_{\theta z} \right) \hat{n}_y \\ &- \left( \kappa_{xz} \left| \vec{\theta} \right| \cos \phi_{\theta x} + \kappa_{yz} \left| \vec{\theta} \right| \cos \phi_{\theta y} + \kappa_{zz} \left| \vec{\theta} \right| \cos \phi_{\theta z} \right) \hat{n}_z \end{aligned} \qquad \text{Equation 2.2-125}$$

The dot product of the heat flux and the temperature gradient is shown in Equation 2.2-126. When that result is applied to Equation 2.2-123, the directional conductivity is shown in Equation 2.2-127.

$$\begin{aligned}\vec{q}\cdot\vec{\theta} = &-\Big[\kappa_{xx}\big(|\vec{\theta}|\cos\phi_{\theta x}\big)^2 + \kappa_{xy}|\vec{\theta}|^2\cos\phi_{\theta y}\cos\phi_{\theta x} \\ &+ \kappa_{xz}|\vec{\theta}|^2\cos\phi_{\theta z}\cos\phi_{\theta x}\Big] \\ &-\Big[\kappa_{xy}|\vec{\theta}|^2\cos\phi_{\theta x}\cos\phi_{\theta y} + \kappa_{yy}\big(|\vec{\theta}|\cos\phi_{\theta y}\big)^2 \\ &+ \kappa_{yz}|\vec{\theta}|^2\cos\phi_{\theta z}\cos\phi_{\theta y}\Big] \\ &-\Big[\kappa_{xz}|\vec{\theta}|^2\cos\phi_{\theta x}\cos\phi_{\theta z} + \kappa_{yz}|\vec{\theta}|^2\cos\phi_{\theta y}\cos\phi_{\theta z} \\ &+ \kappa_{zz}\big(|\vec{\theta}|\cos\phi_{\theta z}\big)^2\Big]\end{aligned} \qquad \text{Equation 2.2-126}$$

$$\begin{aligned}\kappa_{\theta} = &\ \kappa_{xx}(\cos\phi_{\theta x})^2 + \kappa_{yy}\big(\cos\phi_{\theta y}\big)^2 + \kappa_{zz}(\cos\phi_{\theta z})^2 + 2\kappa_{xy}\cos\phi_{\theta x}\cos\phi_{\theta y} \\ &+ 2\kappa_{xz}\cos\phi_{\theta x}\cos\phi_{\theta z} + 2\kappa_{yz}\cos\phi_{\theta y}\cos\phi_{\theta z}\end{aligned} \qquad \text{Equation 2.2-127}$$

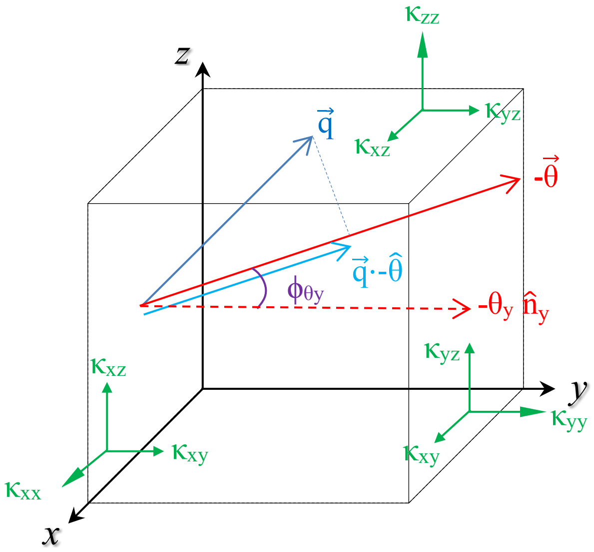

Figure 2-12 Diagram of a possible heat flux and temperature gradient alignment along with thermal conductivity tensor components.

In PFLOTRAN, given a cartesian grid system, the upwind and downwind cell faces will be normal to some unit vector in the *x*, *y,* or *z* direction. Therefore, in such a discretization, the gradient is defined using the temperature difference across the cell and the distance, so it must be aligned with the unit vector traversing the two opposite cellular faces. For example, when the cell is traversed by $\hat{n}_x$, $\cos\phi_{\theta x} = 1$ while $\cos\phi_{\theta y} = \cos\phi_{\theta z} = 0$, which cancels the terms with the off-diagonal tensor components. Only when the principal axes of the thermal conductivity tensor are misaligned with the cartesian grid, or else when a polyhedral grid or flexed hex mesh is used, can multiple direction cosines be nonzero and allow the off-diagonal components to be usable. If the grid is always oriented along the principal axes of conductivity, the off-diagonal elements will be zero.

The eigenvectors ($\Lambda_1$, $\Lambda_2$, $\Lambda_3$) of Equation 2.2-121 yield the principal axes of the heat flux and the associated eigenvalues ($\lambda_1$, $\lambda_2$, $\lambda_3$) represent the extreme values. Since the tensor is symmetric, if the unit vectors $\hat{n}_i$ are rotated to align with $\Lambda_i$, **K** can be represented as a diagonal matrix in $\lambda_i$ with basis $\Lambda_i$, as shown in Equation 2.2-128. If only diagonal components are specified by the user, those components are the eigenvalues and the eigenvectors are the original unit vectors in *x*, *y*, and *z*. Therefore, it is acceptable to specify anisotropy ratios of one since the extreme values will always be the user-specified wet and dry values. However, the eigenvalues for a full tensor may result in extreme values exceeding the user-specified values of $\kappa_T$. Furthermore, the tensor must be positive semi-definite (Powers 2004). Therefore, the user must choose anisotropy ratios such that $\lambda_i \geq 0$ and $\lambda_i \leq \kappa_T$ (wet or dry).

$$\mathbf{K}' = \begin{bmatrix} \lambda_1 & 0 & 0 \\ 0 & \lambda_2 & 0 \\ 0 & 0 & \lambda_3 \end{bmatrix} \qquad \text{Equation 2.2-128}$$

### *2.2.4.2 Anisotropy Implementation*

The anisotropy routines are triggered when the user specifies anisotropy ratios ($f_{ij}$) in the input deck for the default thermal characteristic curve or its temperature-dependent derived-types, as shown Table 2-7. Currently, $\kappa_T^{dry}$ and $\kappa_T^{wet}$ are still specified as usual, and as of this report, the user cannot specify wet and dry anisotropic components in a piecemeal manner. Rather, ratios are used to modify both wet and dry values when the tensor operations are called. The upwind and downwind thermal conductivities are modified by these tensor operations right before the effective thermal conductivity functions are called to evaluate average dry and wet thermal conductivities.

To ensure that previous regression tests with isotropic thermal conductivity are unperturbed, the anisotropy routines check if the user has inadvertently specified a diagonal, isotropic tensor. If that is true, the tensor operations are skipped to maintain the previous computational speed, as mathematically, the tensor operation would not affect the upwind/downwind values of $\kappa_T$. If the user specifies one off-diagonal component, they are required to initialize the other two components as well. If no off-diagonal components are initialized, they are set to zero. All diagonal components must be initialized, and if no components are specified at all, the previous functionality with isotropic thermal conductivities is not affected. When a user specifies a full tensor, the eigenvalues are checked to ensure that the tensor is positive semi-definite. There is also a warning if eigenvalues may cause the user input thermal conductivity values to be exceeded along the tensor's principal axes.

Table 2-7 User inputs for thermal conductivity anisotropy.

| User Input | Value | Applicability and Implementation |
|---|---|---|
| **THERMAL_CHARACTERISTIC_CURVES** | <name> | |
| **THERMAL_CONDUCTIVITY_FUNCTION** | <func> | DEFAULT and derived types |
| **THERMAL_CONDUCTIVITY_DRY** | $\kappa_T^{dry}$ | Instance modified after tensor operation |
| **THERMAL_CONDUCTIVITY_WET** | $\kappa_T^{wet}$ | Instance modified after tensor operation |
| **ANISOTROPY_RATIO_X** | $f_{xx}$ | $\kappa_{xx}^{dry}=f_{xx}\kappa_T^{dry}$, $\kappa_{xx}^{wet}=f_{xx}\kappa_T^{wet}$ |
| **ANISOTROPY_RATIO_Y** | $f_{yy}$ | $\kappa_{yy}^{dry}=f_{yy}\kappa_T^{dry}$, $\kappa_{yy}^{wet}=f_{yy}\kappa_T^{wet}$ |
| **ANISOTROPY_RATIO_Z** | $f_{zz}$ | $\kappa_{zz}^{dry}=f_{zz}\kappa_T^{dry}$, $\kappa_{zz}^{wet}=f_{zz}\kappa_T^{wet}$ |
| **ANISOTROPY_RATIO_XY** | $f_{xy}$ | $\kappa_{xy}^{dry}=f_{xy}\kappa_T^{dry}$, $\kappa_{xy}^{wet}=f_{xy}\kappa_T^{wet}$ |
| **ANISOTROPY_RATIO_XZ** | $f_{xz}$ | $\kappa_{xz}^{dry}=f_{xz}\kappa_T^{dry}$, $\kappa_{xz}^{wet}=f_{xz}\kappa_T^{wet}$ |
| **ANISOTROPY_RATIO_YZ** | $f_{yz}$ | $\kappa_{yz}^{dry}=f_{yz}\kappa_T^{dry}$, $\kappa_{yz}^{wet}=f_{yz}\kappa_T^{wet}$ |
| **END** | | |
| **TEST** | | DEFAULT and derived types |
| **END** | | |

#### 2.2.4.3 Composite Curve

A composite curve has been defined that applies previously defined TCCs along specific principal axes. This development was motivated by the need to incorporate different models for the transverse and axial extents of a DPC for criticality studies. The composite TCC uses scaling parameters derived from the unit vectors of the gridded domain, which in turn modify and sum the results of the constituent functions. The composite TCC is specified in the input deck downstream of the constituent functions according to Table 2-8. The test feature has not been implemented for this curve due to direction-dependence.

For example, if "cct_radial" and "cct_axial" are defined upstream in the input deck, the first can be applied in the X and Y directions and the second along the Z direction in a composite TCC named "dpc_1". When the TCC for “dpc_1” is called, a weighted average of all directional thermal conductivities is given depending on the unit vector involved, preserving all temperature and saturation-dependencies of the constituent functions.

The anisotropy ratio capability does not conflict and can also be used with the composite TCC if such a level of detail is desired. It is recommended that the constituent curves do not have anisotropy ratios of their own to avoid a non-physical result.

Table 2-8 User inputs for a composite TCC.

| User Input | Value | Applicability and Implementation |
|---|---|---|
| **THERMAL_CHARACTERISTIC_CURVES** | <name> | |
| **THERMAL_CONDUCTIVITY_FUNCTION** | <func> | COMPOSITE |
| **COMPOSITE_X** | <name> | A previously-defined TCC applied along the x-axis |
| **COMPOSITE_Y** | <name> | A previously-defined TCC applied along the y-axis |
| **COMPOSITE_Z** | <name> | A previously-defined TCC applied along the z-axis |
| **END** | | |
| **END** | | |

### 2.2.5 Special Thermal Conductivity Models

#### 2.2.5.1 Assembly-Specific Models

Thermal models have been developed for the radial and axial extents of a DPC, as discussed in Price et al. (2020). The radial model $\kappa_T^{radial}$ uses the format of the default TCC but represents the dry and wet components with special functions. The dry conductivity is represented with a temperature-dependent power law derived from backfilled assembly measurements (TRW Environmental Safety Systems, 1996). This model assumes that thermal radiation controls heat transfer in a dry assembly and that thermal conductivity may be represented with a power law using a temperature coefficient $\alpha_0$, an exponent $\alpha_1$, and a scaling factor $\kappa_{T,0}^{dry}$, as shown in Equation 2.2-129.

$$\kappa_T^{dry}(T) = \kappa_{T,0}^{dry} + \alpha_0 T^{\alpha_1} \qquad \text{Equation 2.2-129}$$

Over time, canisters may be liable to fail and allow for the influx of water, which can flood the assemblies. The model for $\kappa_T^{wet}$ is derived from a model on the effective thermal conductivity of an array of cylinders surrounded by stagnant water (Cheng and Hsu, 1999). Such an analysis could apply to the transverse direction across assemblies in a DPC when this reference model is modified to account for their square cross sections. $\kappa_T^{wet}$ can be estimated from the thermal conductivity of flooding groundwater ($\kappa_T^{H_2O}$), the thermal conductivity of solid components like the fuel pins ($\kappa_T^S$), and the porosity of the assembly ($\phi$), as shown in Equation 2.2-130.

$$\kappa_T^{wet}(\phi) = \kappa_T^{H_2O}\left[1 - \sqrt{1-\phi} + \frac{\sqrt{1-\phi}}{1 + \left(\frac{\kappa_T^{H_2O}}{\kappa_T^S} - 1\right)\sqrt{1-\phi}}\right] \quad \text{Equation 2.2-130}$$

The dry and wet components are then combined into the default-type analysis to describe the radial thermal conductivity of a DPC, as shown in Equation 2.2-131.

$$\kappa_T^{radial}(S_l, T, \phi) = \kappa_T^{dry}(T) + \sqrt{S_l}\left[\kappa_T^{wet}(\phi) - \kappa_T^{dry}(T)\right] \quad \text{Equation 2.2-131}$$

A related function assumes parallel heat conduction of solid assembly components and water along the *axial* extent of a DPC. The assembly porosity is used to separate solid and water components of thermal conductivity, where the water component is multiplied by the liquid saturation. This assumes that the thermal conductivity component of air, which comprises the volume fraction $\phi(1 - S_l)$, is negligibly small. Therefore, the model is only dependent on liquid saturation and $\phi$, as shown in Equation 2.2-132.

$$\kappa_T^{axial}(S_l, \phi) = (1-\phi)\kappa_T^S + \phi\kappa_T^{H_2O}S_l \quad \text{Equation 2.2-132}$$

The models are defined in the input deck according to Table 2-5. In general, they require specification of the thermal conductivities for water and the assembly solids as well as the assembly porosity. The radial function requires additional input of the dry-state temperature coefficient and exponent as well as the reference value of dry thermal conductivity. The user may also use Equation 2.2-129 or Equation 2.2-130 independently as standalone functions by specifying those individual TCCs and optionally including constant $\kappa_T^{wet}$ or $\kappa_T^{dry}$, respectively, to impart saturation dependence via the default relationship.

Table 2-9 User inputs for assembly-specific thermal characteristic curves.

| User Input | Value(s) | Applicability |
|---|---|---|
| **THERMAL_CHARACTERISTIC_CURVES** | <name> | All |
| **THERMAL_CONDUCTIVITY_FUNCTION** | <TCC type> | All |
| **THERMAL_CONDUCTIVITY_WATER** | $\kappa_T^{H_2O}$ | ASM_AXIAL/ASM_RADIAL/ASM_WATER_FILLED |
| **THERMAL_CONDUCTIVITY_SOLID** | $\kappa_T^S$ | ASM_AXIAL/ASM_RADIAL/ASM_WATER_FILLED |
| **POROSITY_ASSEMBLY** | $\varphi$ | ASM_AXIAL/ASM_RADIAL/ASM_WATER_FILLED |
| **ASM_DRY_COEFFICIENT** | $\alpha_0$ | ASM_RADIAL/ASM_DRY |
| **ASM_DRY_EXPONENT** | $\alpha_1$ | ASM_RADIAL/ASM_DRY |
| **THERMAL_CONDUCTIVITY_DRY** | $\kappa_T^{dry}$ | ASM_RADIAL/ASM_DRY/ASM_WATER_FILLED* |
| **THERMAL_CONDUCTIVITY_WET** | $\kappa_T^{wet}$ | ASM_DRY* |
| **END** | | |
| **TEST** | | All |
| **END** | | |

*** Optional to impart saturation-dependence in standalone functions**

As mentioned in Section 2.2.3, directional variation in a waste form containing spent nuclear fuel can be simulated by incorporating the axial and radial models into a composite TCC. The sub-functions for this TCC would be specified depending on the orientation of the waste form centerline with respect to the main axes of the coordinate system.

## 2.2.6 Smectite-to-Illite Transition

In a repository, the waste package is surrounded by an EBS containing a buffer of bentonite which provides an effective barrier to radionuclide transport due to low hydraulic conductivity and favorable swelling characteristics. Bentonite is comprised largely of the montmorillonite mineral of the smectite group, which has an articulated, laminar structure that allows for the adsorption of water and subsequent expansion. Thermodynamic equilibrium of the smectite can be affected by the silica reactivity and potassium concentration in the repository environment (Karnland & Birgersson, 2006). A potassium cation ($K^+$) can act as a counter-ion and affect the net-negative layer charge of the smectite. If quartz ($SiO_2$) can precipitate (crystallize) in the presence of potassium, there is reduced water interaction and reduced swelling from the interlayer collapse in smectite as it transforms to illite. This loss of swelling capacity and plasticity from the smectite-to-illite transition is susceptible to inducing volume shrinkage and increased permeability in the buffer. There is also a counteracting effect from increased radionuclide sorption on illite. This mineral transition is found to be correlated with temperature, so the transition can be driven by elevated waste package temperatures during a criticality event.

### *2.2.6.1 Model and implementation*

PFLOTRAN has reactive transport modeling capabilities that could potentially be used to account for the reagents of the S-I transition, including quartz, potassium, sodium, etc. Rather than introduce physical changes in materials via the reactive transport side of the code, a surrogate model can be used on the flow side to handle material transformations (including the S-I transition) and remove dependence on chemical parameters.

In this new model, the approach assumes that the transition from smectite to illite can be directly translated into a change in the original permeability and sorption characteristics. The scale of this change would have to be estimated a priori as part of the surrogate model. Furthermore, it has to be assumed that the geochemical conditions needed for illitization are present either at time zero or when the threshold temperature is exceeded.

Alteration of the buffer permeability is considered part of an irreversible time- and temperature-dependent mineral transition. The rate of illitization is temperature-dependent and the reaction only takes place when the temperature of a grid cell is above the user-specified threshold (default of 0 °C). The rate of illitization is used to determine the fractional increase in illite in the material in a given time step. In a sense, the surrogate model incorporates the effects of mineral phase transitions without detailed reactive transport calculations and without modifying the gridded domain despite the decrease in buffer swelling capacity.

The time rate of change of smectite into illite is taken from the Huang et al. (1993) study and shown in Equation 2.2-133 for a given time step *i+1*.

$$-\frac{df_S}{dt}\bigg|^{i+1} = \begin{cases} [K^+] \cdot \left(f_S^i\right)^2 \cdot A \exp\left(-\frac{E_a}{\mathcal{R} \cdot T^{i+1}}\right) & T^{i+1} \geq T_{th} \\ 0 & T^{i+1} < T_{th} \end{cases}$$ Equation 2.2-133

The equation is based on the potassium cation concentration [$K^+$] in mol/L and the previous smectite fraction $f_S^i$, where $A$ is the frequency term in L/mol-s, $E_a$ is the activation energy in J/mol, $\mathcal{R}$ is the ideal gas constant, $T^{i+1}$ is the temperature in Kelvin of the grid cell, and $T_{th}$ is the threshold temperature below which the reaction does not take place. The value of [$K^+$] is currently implemented as a fixed input value and is not evaluated from transport. The expression implies that at steady-state temperature, the rate of illitization is reduced as more smectite is replaced with illite.

By integrating Equation 2.2-133 over the time period, the smectite fraction is evaluated in Equation 2.2-134.

$$f_S^{i+1} = \frac{f_S^i}{1 - [K^+] \cdot A \exp\left(-\frac{E_a}{\mathcal{R} \cdot T^{i+1}}\right) \cdot \left(t^{i+1} - t^i\right) \cdot f_S^i}$$ Equation 2.2-134

The illite fraction is defined in Equation 2.2-135 as the complement of the smectite fraction. For this reason, the code only keeps track of $f_S$ as a variable for checkpointing and output.

$$f_I^{i+1} = 1 - f_S^{i+1}$$ Equation 2.2-135

The change in a given permeability component $k_j^{i+1}$ at time step *i+1* as a result of illitization is computed with Equation 2.2-136 using the proportional change in the smectite fraction and a shift factor $C_k$ along with the original permeability tensor $k_j^0$.

$$k_j^{i+1} = k_j^0 \left[1 + \left(\frac{f_I^{i+1} - f_I^0}{f_S^0}\right) \cdot C_k\right]$$ Equation 2.2-136

This suggests that when all the original smectite is transformed to illite, the permeability has been modified by a factor of $1+C_k$. The original permeability is employed as opposed to a recursive solution to maintain the relevance of $C_k$ if a simulation needs to be restarted. This reference permeability tensor is saved within the illitization object before it is replaced with the checkpoint value in the auxiliary variables. Also, given the intermittent nature of the function's temperature dependence (via the temperature threshold), Equation 2.2-136 ensures that the permeability does not change if the mineral fractions do not change over a given time step.

#### 2.2.6.2 Test problem

A simple problem was devised in PFLOTRAN to test the S-I model given the times and temperatures needed for the mineral transformation. The test domain is a 4 by 4 by 20-meter water-saturated block of soil with a porosity of 25%, tortuosity of 50%, permeability of $10^{-12}$ m$^2$, and hydrostatic pressure of 1 MPa. The soil has an initial temperature of 20 °C, a solid density of 2,650 kg/m$^3$, and heat capacity of 830 J/kg-K. It is discretized into 1 m$^3$ grid blocks and has a boundary condition at the northern face with water at 5 MPa and 260 °C. A 1-meter-thick layer of smectite-rich bentonite buffer exists 2 meters into the soil from the northern face, as shown in Figure 2-13.

The buffer is split into "Buffer 1" on the east with an initial permeability of $10^{-20}$ m$^2$ and "Buffer 2" on the west with an initial permeability of $10^{-16}$ m$^2$. The two buffer regions have unique initial smectite fractions but otherwise have the same material properties, including a porosity of 35%, solid density of 2,700 kg/m$^3$, heat capacity of 830 J/kg-K, and a default TCC from 0.6 to 1.5 W/m-K. There is 90% initial smectite in Buffer 1 and 75% in Buffer 2, with a reaction threshold temperature of 40°C in the first region and 60 °C in the second. The activation energy is defined as $1.18\times10^5$ J/mol, the frequency term is $8.08\times10^4$ L/mol-s, and the potassium concentration is $2.16\times10^{-3}$ M. The permeability in each material is set to increase by 1000-fold when the fraction of illite reaches 100% (i.e. $C_k = 999$).

Results for temperature and permeability over time are shown in Figure 2-14 for Buffer 2 grid cells. The boundary condition introduces a temperature gradient that heats the region beyond the threshold temperature of 60 °C around 0.0244 years (9 days). A maximum steady-state temperature of 260 °C is reached by 94.9 years, while the fastest rate-of-change of the permeability from the illitization reaction occurs at around 11.7 years. A significant fraction of smectite is transformed to illite by $10^4$ years, with a final illite fraction of 99.5% from the original 25%. This corresponds to increase in permeability to $9.94\times10^{-14}$ m$^2$ from the original $10^{-16}$ m$^2$. Likewise, in Buffer 1, the permeability increases from $10^{-20}$ m$^2$ to $9.95\times10^{-18}$ m$^2$ with a final illite fraction of 99.5% compared to the original 10%. These results demonstrate the asymptotic behavior expected from Equation 2.2-134 and Equation 2.2-135 as the smectite fraction decreases over time. This is plotted visually in Figure 2-15, where the smectite quantities in the two buffer regions eventually align despite different initial conditions.

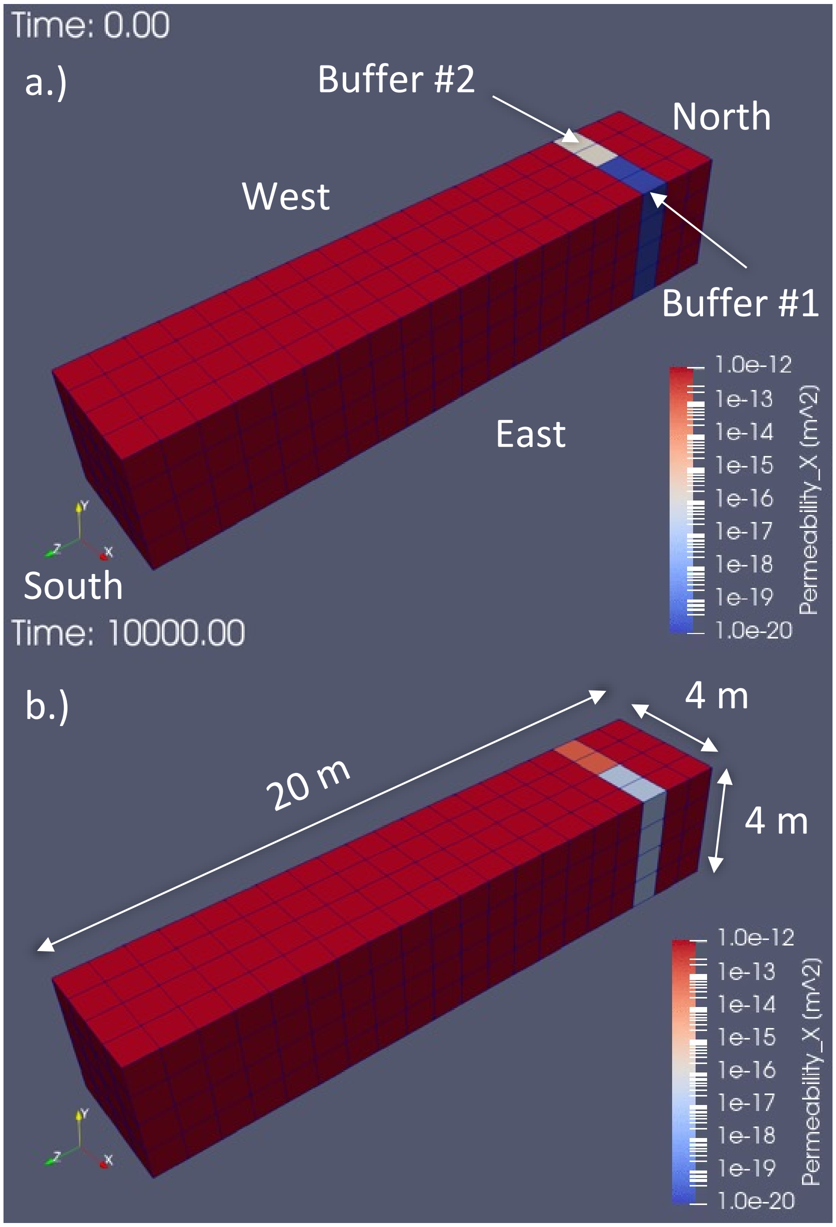

Figure 2-13 Test domain showing change in permeability in the buffer from a.) 0 years to b.) $10^4$ years.

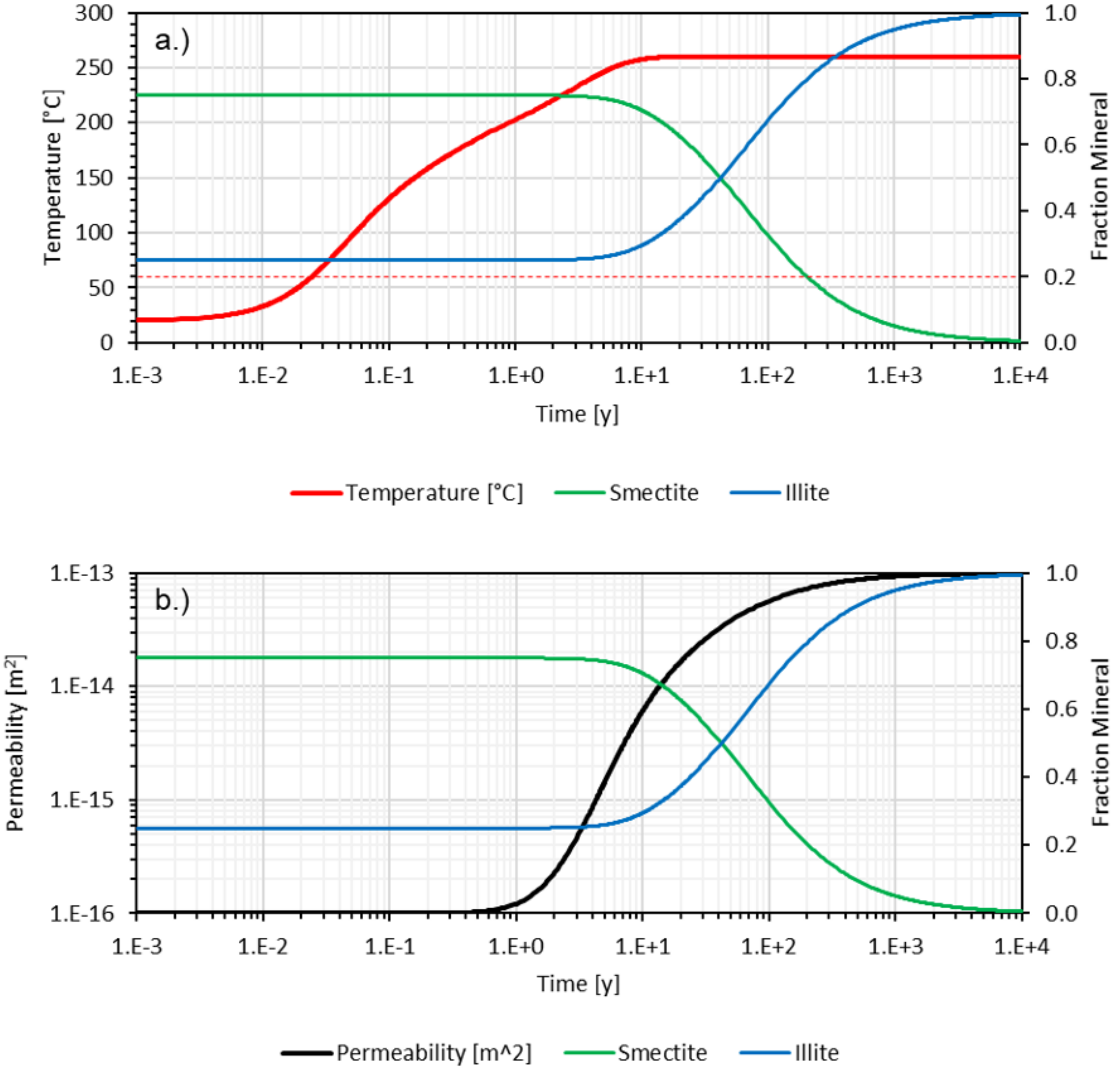

Figure 2-14 (a.) Temperature and (b.) permeability over time for grid cells undergoing smectite to illite transition in Buffer #2 in the test problem.

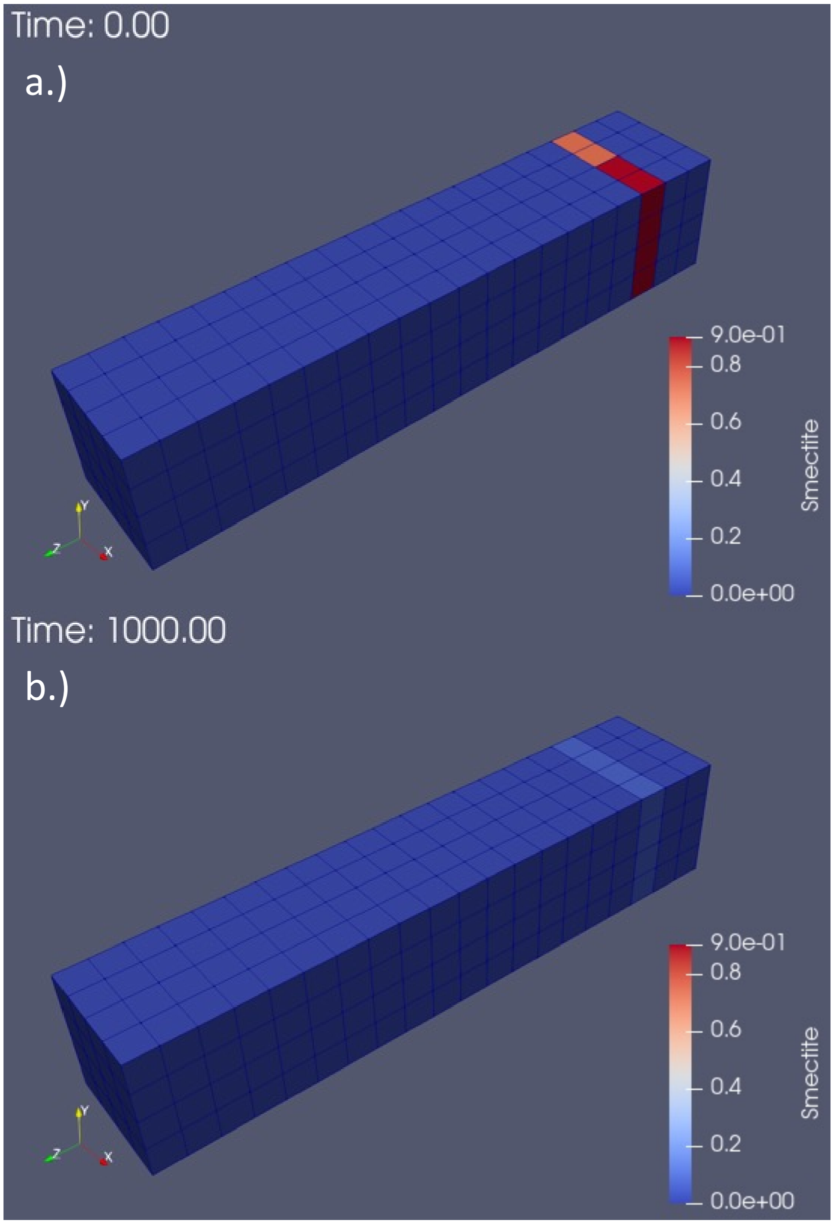

Figure 2-15 Smectite fractions at a) 0 years and b) $10^3$ years using a scale from 0% to 90%.

#### 2.2.6.3 *Future work*

When the plots were generated in this section, the illitization feature formed its own module in the same hierarchy as characteristic curves and TCCs. It was applied within GENERAL mode (two-phase, two component flow plus energy conservation) during the modification of those auxiliary variables. The overall programming will be expanded into a generalized module for material transformations that extend beyond the effects from illitization, with illitization being just one type of process that can affect the system permeability.

The illitization type can be expanded with additional models. Another model for the illitization rate is provided by J. Cuadros & J. Linares, 1996 and is shown in Equation 2.2-137. In this expression, the potassium concentration is modified with the exponent $m$ and the order for the smectite fraction is raised to order $n$. The rate constant $k$ is also a temperature-dependent Arrhenius term.

$$-\frac{df_S}{dt} = [K^+]^m {f_S}^n \cdot k(T)$$

Equation 2.2-137

Using the time step notation from earlier, the time-integrated value for the smectite fraction is shown for two solutions of $n$ in Equation 2.2-138. When employing $m = 1$ and $n = 2$, the solution for the Huang *et al.*, 1993 is obtained, demonstrating that the Cuadros and Linares model is a generalization to arbitrary order. Therefore, including such an option will expand modeling parameterization and impart more realism to a simulation. It can also be convenient for fitting to on-site data for a given performance assessment.

$$f_S^{i+1} = \left\{[K^+]^m \cdot k(T) \cdot (n-1)\left(t^{i+1} - t^i\right) + \left(f_S^i\right)^{1-n}\right\}^{1/1-n}, n > 1$$

$$f_S^{i+1} = f_S^i \cdot \exp\left\{-k(T) \cdot [K^+]^m \cdot \left(t^{i+1} - t^i\right)\right\}, n = 1$$

Equation 2.2-138

## 2.2.7 Criticality Sub-module

### *2.2.7.1 Neutronics Surrogate Modeling*

PFLOTRAN now has the capability to integrate the heat source term from criticality events in multiple waste forms in a repository simulation. Rather than perform internal neutron transport and kinetics calculations for each waste form, neutronics surrogate models are used instead to define the source term given the evolving hydrological conditions in the system. This requires an a priori understanding of the conditions needed to reach a critical configuration in the waste form, the thermal-hydraulic constraints defining the total power output from sustained chain reactions, and the total duration.

The waste form process model allows for the definition of criticality mechanism sub-blocks to define steady-state criticality events. Information included within the sub-blocks includes the criticality start and end times and definitions for decay heat, nuclide inventory, and the heat of criticality. The decay heat may be defined via a time-dependent lookup table generated from a depletion code, which in turn relies on the specific characteristics. Likewise, external results from a depletion calculation may be used to override the implicit Bateman solution for radionuclide inventory calculated in the UFD Decay process model.

PFLOTRAN now features a lookup table for the heat of criticality from a steady-state criticality event. ORNL has provided results from coupled neutronics and thermal-hydraulics simulations on the power output from steady-state criticality for a given waste package boundary temperature. By applying the waste form temperature and criticality start time to interpolation, the feature allows for the specification of temperature-dependent heat emission during a steady-state criticality event.

Before implementing a temperature-dependent source term, an iterative process is needed between the PFLOTRAN and neutronics analyses to find convergence in the system constraints. This usually begins with an understanding of the start time for criticality to provide the original inventory constraint. There is also an understanding of how long the event lasts after succumbing to reactivity feedback effects from burnup, heating, loss of moderator, or loss of critical geometry. PFLOTRAN can then be run with constant power levels from criticality over the specified time period to find steady-state hydrological conditions that can refine a coupled neutronics/thermal hydraulics analysis. Often, to describe the worst-case scenario, the power level is selected to be the highest output at which some liquid phase remains (e.g., the liquid phase is not entirely boiled off in the saturated shale system). Continued correspondence between ORNL and SNL has refined the concurrence of repository conditions and the thermodynamic state in the neutronics calculations

Critical levels of water saturation and water density can be specified that determine the limits below which criticality cannot be sustained, which then temporarily halts the heat emission from criticality and isolates the source term to decay heat. The critical water saturation is meant to be representative of the groundwater flood level in a waste package, which is likely to vary in an unsaturated alluvium repository. There exists a water level in the void space of the canister below which neutron multiplication drops below unity. The critical water density is more applicable to a saturated argillite repository, where the hydrostatic pressure can expand the liquid phase to a greater breadth of temperatures, leaving the canister largely flooded after breaching. Therefore, criticality would be subject to decreasing density in the moderator as a negative reactivity feedback mechanism.

There can be multiple criticality mechanisms within the process model but currently only one criticality mechanism can be defined per waste form. Multiple criticality events per waste form are slated for further work to model transient criticality perturbations and user-defined periodic criticality. However, multiple waste packages can be modeled with unique temperature-dependent power output, distribution of failure times, and criticality duration, which provides great flexibility to the performance assessment.

### 2.2.7.2 Zircaloy Spacer Grid Degradation

**Overview**

PFLOTRAN now features a spacer grid degradation option for waste packages containing spent nuclear fuel. This is a time, temperature, and saturation-dependent corrosion model that monitors the fraction of non-corroded Zircaloy in the SNF assemblies, or the "spacer grid vitality." Its purpose is to introduce a corrosion model that in turn provides a criticality termination mechanism for steady-state criticality in SNF. When the spacer grids (Figure 2-16) have extensively degraded, the fuel rods are assumed to lose their critical configuration from spatial self-shielding effects and reduced moderation from interstitial water upon rod collapse/consolidation.

The feature is implemented at the same hierarchy as the waste form mechanism and criticality mechanism within the waste form process model. It requires input of the total mass and surface area of all assemblies in the package, along with governing rate parameters. Since the model treats the corrosion phenomenon globally within the waste package with no fidelity for individual assembly characteristics, the user has to employ averaged values for the assemblies in the package. When the spacer grid vitality falls below 1% of the original total mass, all criticality events associated with the waste package are permanently ceased due to an assumed loss of critical configuration.

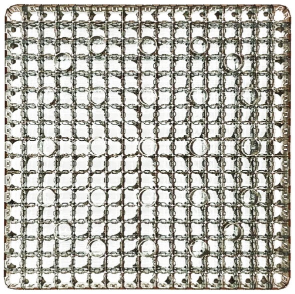

Figure 2-16 A Zircaloy spacer grid for a 17×17 PWR assembly.

**Model**

The spacer grid vitality ($V$) is determined using the corrosion rate ($R$) for time steps $t^i$ to $t^{i+1}$ and a total initial grid mass $M_0^{SG}$, as shown in Equation 2.2-139.

$$V^{i+1} = V^i - \frac{R^{i+1} \cdot \left(t^{i+1} - t^i\right)}{M_0^{SG}}$$ Equation 2.2-139

To account for the role of water level in a system with evolving saturation (e.g. unsaturated alluvium) a saturation-dependent ramp function can be used to alter the corrosion rate given partial inundation of the assemblies. This saturation-dependent ratio $f(\bar{S}_l)$ for water level correction is defined in Equation 2.2-140, where $S_l^{exp}$ is the saturation for which the spacer grids are considered fully inundated with water.

$$f\left(\bar{S}_l^{i+1}\right) = \begin{cases} \dfrac{\bar{S}_l^{i+1}}{S_l^{exp}} & \bar{S}_l^{i+1} < S_l^{exp} \\ 1 & \bar{S}_l^{i+1} \geq S_l^{exp} \end{cases}$$ Equation 2.2-140

The corrosion rate is governed by an Arrhenius term with constant $\mathcal{C}$, activation energy $Q$, and the average waste package temperature $\bar{T}$. This term is further modified with the cumulative spacer grid surface area $A_0^{SG}$ and $f(\bar{S}_l)$, as shown in Equation 2.2-141.

$$R^{i+1} = f\left(\bar{S}_l^{i+1}\right) \cdot A_0^{SG} \cdot \mathcal{C} \exp\left(-\frac{Q}{\mathcal{R} \cdot \bar{T}^{i+1}}\right) \qquad \text{Equation 2.2-141}$$

The spacer grid degradation model is intended to be combined with the neutronics surrogate model and illitization model to test interplay between the heat of criticality and the physical properties of the engineered barrier system. In addition, the new thermal modeling capabilities would be incorporated to demonstrate potential anisotropy effects within the larger heat transfer context.

### Test Problem

A simple test problem was constructed to verify that the new model can successfully terminate steady-state criticality events in multiple waste forms. Since representative corrosion parameters would require long simulation times for the effects to be realized, artificially elevated parameters were employed for purposes of inspection. The test domain is a 4 by 4 by 20-meter water-saturated block of soil with a porosity of 25%, tortuosity of 1.0, permeability of $10^{-12}$ m$^2$, and hydrostatic pressure of 1 atm. It is discretized into 1 m$^3$ grid blocks and has a boundary condition at the northern face (concurrent with the origin) with water at 1 atm and 100 °C. The soil has an initial temperature of 20 °C, a density of 2,650 kg/m$^3$, and heat capacity of 830 J/kg-K. Thermal conductivity is governed by a default TCC from 5.5 to 7.0 W/m-K and the characteristic curve uses a Van Genuchten relationship for saturation and Mualem relationship for liquid and gas permeability.

Within the soil there are three regions defining waste forms (WF) of 4 m$^3$ volume at $z$ = 3-5 m, 10-12 m, and 14-16 m, where all are defined at $x$ = 2-4 m and $y$ = 2-4 m (see Figure 2-17). The waste form characteristics, as defined in the waste form process model block, are shown in Table 2-10, where the waste packages are numbered along the $+z$ axis. They all have unique breach times, waste form mechanisms, and criticality mechanisms, and WF #1 and #2 also feature a spacer grid degradation mechanism. Of the criticality mechanisms, the start and end times are unique and overlap for some extent of time. They all feature the same time-dependent decay heat dataset, which, for the short time period of the simulation, provides an essentially constant power output of 1 kW. Constant heats of criticality are employed for ss_crit_1 and ss_crit_3, while ss_crit_2 employs a temperature-dependent lookup table with a maximum of 4 kW (plotted in Figure 2-18) to test the mix of specifications. A critical water saturation is defined within each mechanism, while a critical water density is further specified for WF #1 and #3. As mentioned previously, the components of the spacer degradation mechanisms for WF #1 and #2 were selected to terminate steady-state criticality within the simulation period of 90 days. Therefore, the choices for $\mathcal{C}$ are very high and those for $Q$ are low. Saturation dependence is active for spc_02 by specifying an $S_l^{exp}$ of 80%, while it is inactive for spc_01.

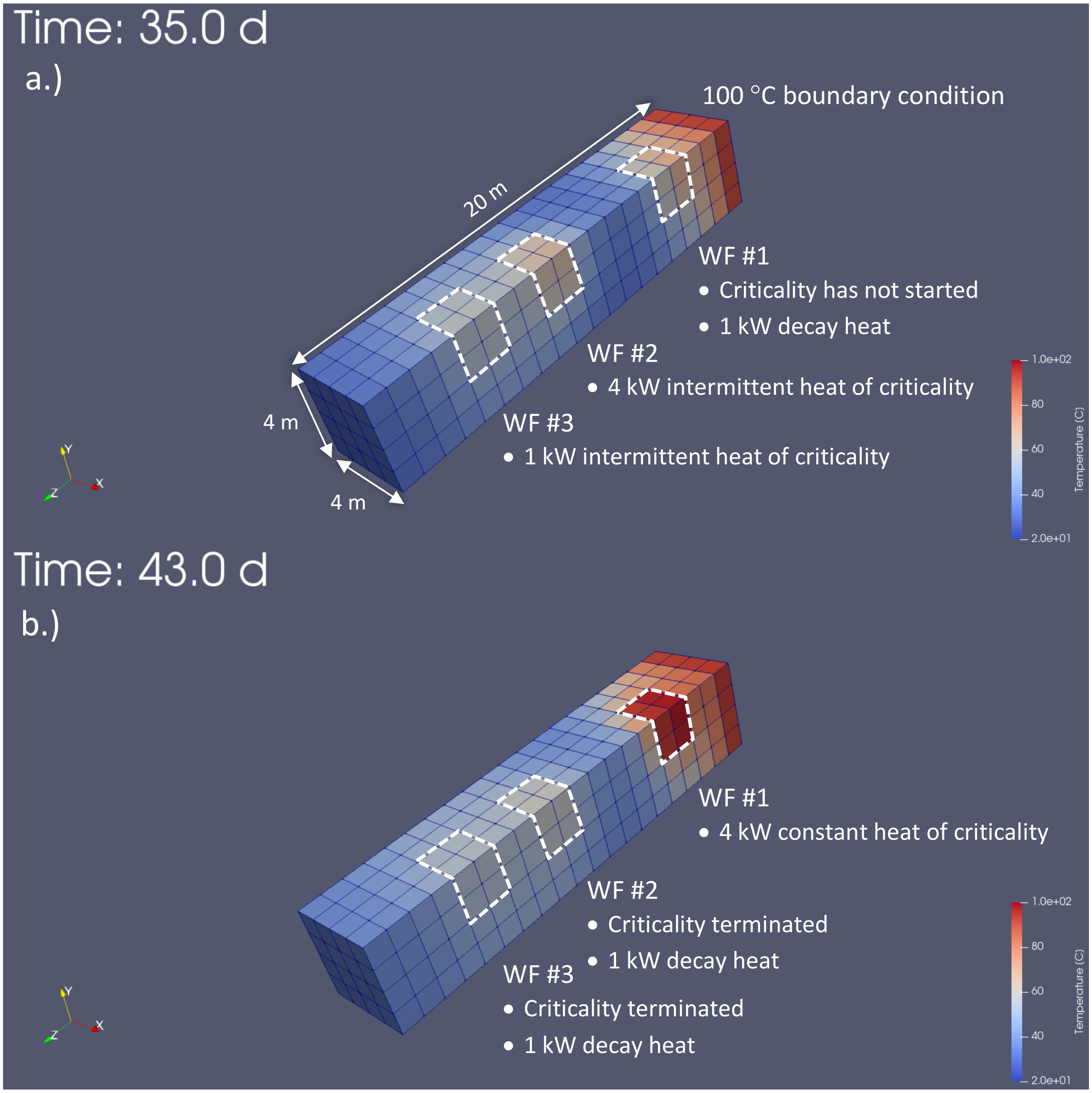

100 °C boundary condition

WF #1
- Criticality has not started
- 1 kW decay heat

WF #2
- 4 kW intermittent heat of criticality

WF #3
- 1 kW intermittent heat of criticality

WF #1
- 4 kW constant heat of criticality

WF #2
- Criticality terminated
- 1 kW decay heat

WF #3
- Criticality terminated
- 1 kW decay heat

Figure 2-17 Diagram of test problem showing temperature at a.) 35.0 d and b.) 45.0 d.

Table 2-10 The parameters employed for the Zircaloy spacer grid degradation test problem.

| PFLOTRAN input | WF #1 | WF #2 | WF #3 | Units |
|---|---|---|---|---|
| **WASTE_FORM** | | | | |
| **REGION** | wf1 | wf2 | wf3 | |
| **CANISTER_BREACH_TIME** | 5.0d+0 | 1.0d+0 | 2.5d+0 | d |
| **MECHANISM_NAME** | DNSF | CUSTOM | GLASS | |
| **CRITICALITY_MECHANISM_NAME** | ss_crit_1 | ss_crit_2 | ss_crit_3 | |
| **SPACER_MECHANISM_NAME** | spc_01 | spc_02 | N/A | |
| **END** | | | | |
| | | | | |
| **CRITICALITY_MECH** | | | | |
| **NAME** | ss_crit_1 | ss_crit_2 | ss_crit_3 | |
| **CRIT_START** | 4.0d+1 | 3.0d+1 | 5.0d+0 | d |
| **CRIT_END** | 7.0d+1 | 6.0d+1 | 9.0d+1 | d |
| **CRITICAL_WATER_SATURATION** | 6.0d-1 | 7.0d-1 | 3.0d-1 | |
| **CRITICAL_WATER_DENSITY** | 8.5d+2 | N/A | 9.0d+2 | $kg/m^3$ |
| **HEAT_OF_CRITICALITY** | | | | |
| **(C)ONSTANT_POWER/(D)ATASET** | (C) 4.0d+0 | (D) Figure 2-18 | (C) 1.0d+0 | kW |
| **END** | | | | |
| **END** | | | | |
| | | | | |
| **SPACER_DEGRADATION_MECHANISM** | | | | |
| **NAME** | spc_01 | spc_02 | N/A | |
| **Q** | 5.75d+04 | 5.70d+04 | | J/mol |
| **MASS** $(M_0^{SG})$ | 8.00d+04 | 1.00d+05 | | g |
| **SURFACE_AREA** $(A_0^{SG})$ | 1.00d+03 | 2.20d+03 | | dm^2 |
| **EXPOSURE_LEVEL** $(S_l^{exp})$ | 0.00d+00 | 8.00d-01 | | |
| **C** | 2.50d+07 | 3.50d+07 | | mg/s-dm$^2$ |
| **END** | | | | |

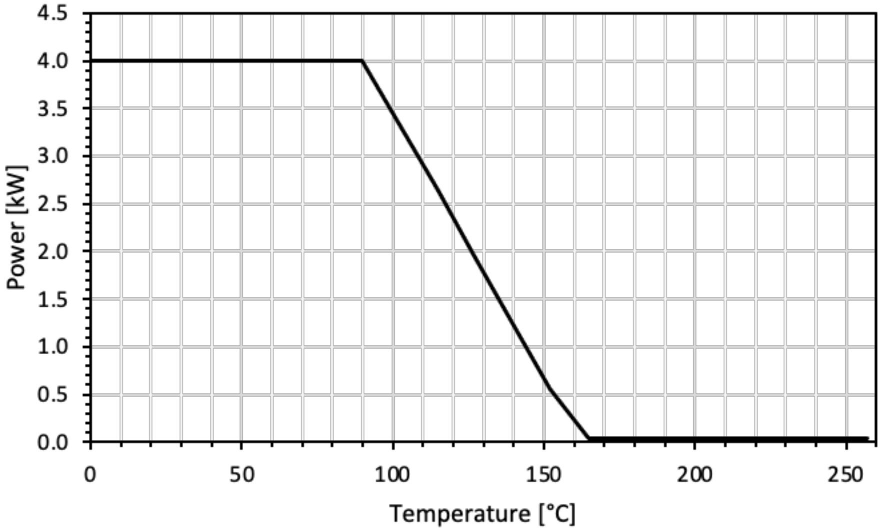

Figure 2-18 Heat of criticality for given temperature during the steady-state criticality event.

**Results**

Information on the criticality source term and spacer grid vitality were reported through print statements and extracted from the standard output using a Perl script, as such output options were not available as of this report. Figure 2-19 shows the spacer grid vitality within WF #1 and #2 along with their average temperatures. The vitality decreases monotonically with time as the average temperature increases in each waste package, which is indicative of a linearly increasing rate from Equation 2.2-141. However, the rates of degradation are observed to increase noticeably when the average temperature rises in each waste package. The degradation rate for WF #2 is less severe because it is reduced by the saturation-dependent term, where the exposure limit of 80% is crossed at 31 days. After 31 days, $S_l$ decreases to about 69% and $f(\bar{S}_l) \approx 0.87$.

Figure 2-20 shows the spacer grid vitality and the heat of criticality along with important time markers including the breach times of the waste packages, the original start and end times of criticality, and the actual times when criticality is terminated. The vitality is confirmed to remain at 1.0 until the packages are breached. The heat of criticality in WF #1 remains at 4 kW until the spacer grid vitality falls below 1% at 43.1 days, preempting the original end time of 70 days for the steady-state event. The region containing WF #1 remains saturated, so the critical water saturation has no effect. However, in WF #2, the soil becomes unsaturated during the criticality event, leading to intermittent criticality oscillating between 0 and 4 kW. Despite the intermittent heat output, the loss of vitality can terminate the criticality event at 35.7 days before the original end time of 60 days. It should be noted that although the heat of criticality in WF #2 was determined through a lookup table, the region did not get hot enough to require an interpolation of different powers; therefore, only the 4 kW maximum in the table is observed.

Figure 2-17 shows the temperature of the gridded domain at two different times. The increase in temperatures in the region defined for WF #1 from 35 d to 43 d is visually demonstrative of the effects of the criticality event. Likewise, the decrease in temperatures of the region defined for WF #2 in the same time frame is indicative of the loss of criticality from spacer grid degradation, where the source term is restricted to decay heat (1 kW). The same phenomenon applies to WF #3 (as will be demonstrated with vitality data) although this is visually indeterminate since the contribution from criticality is only 1 kW.

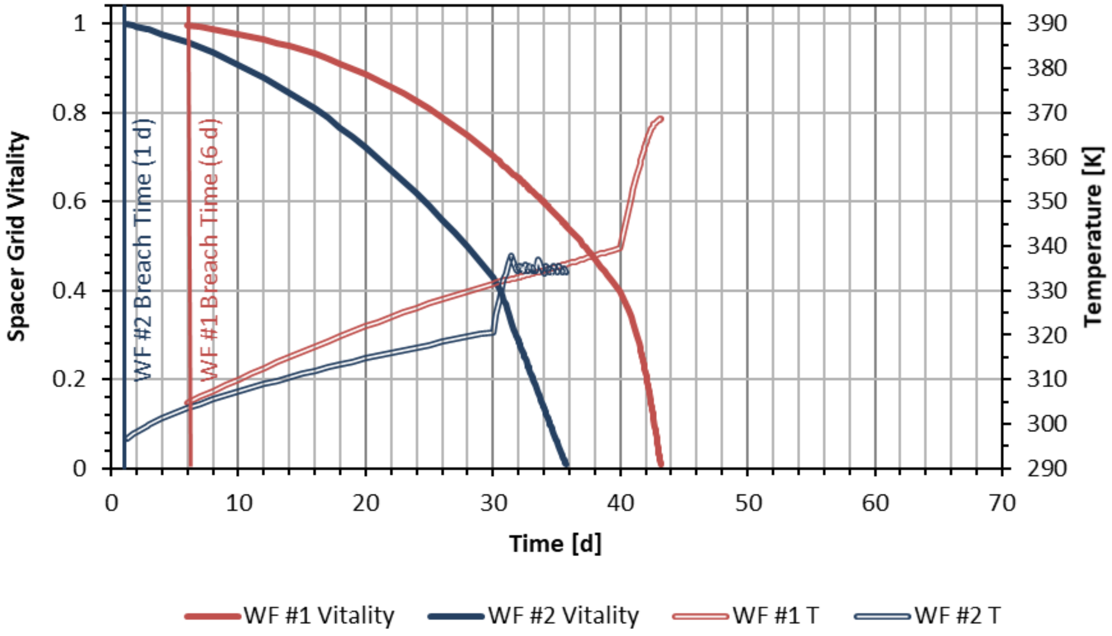

Figure 2-19 Spacer grid vitality and average waste form temperature over time.

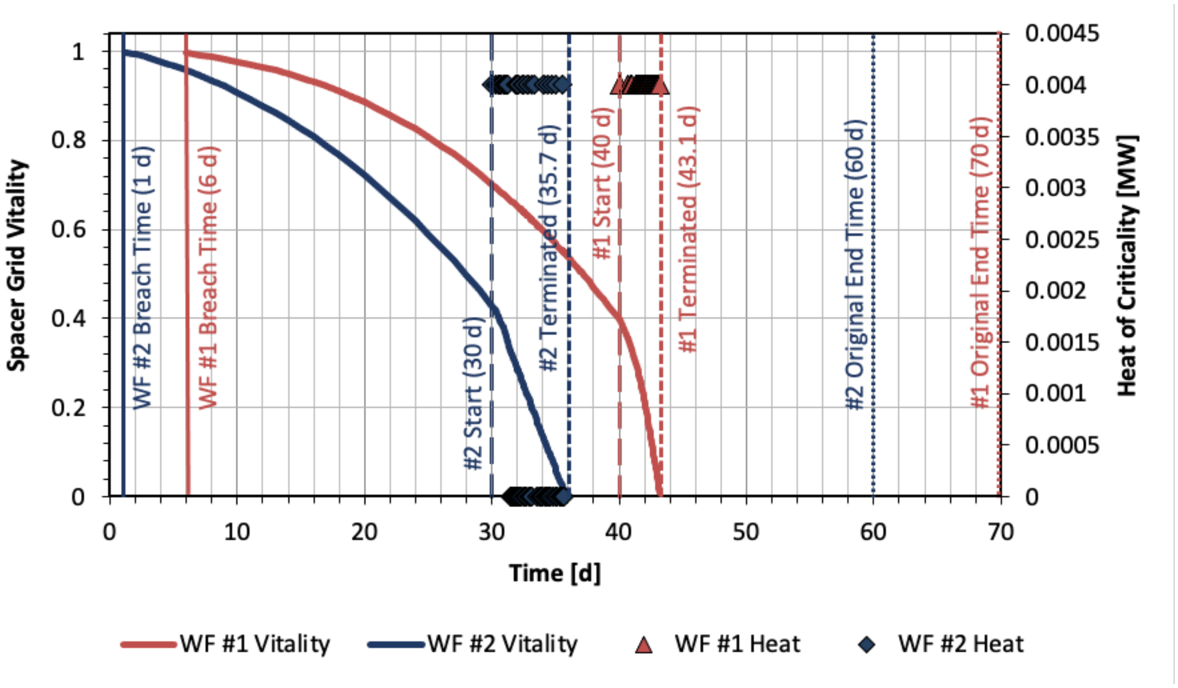

Figure 2-20 Spacer grid vitality and the heat of criticality over time along with time markers for breach time, criticality termination, and the original criticality end time.

Because of the boundary conditions employed, the water densities in the inner half of the domain (from the origin) fluctuate while retaining some level of water saturation, as shown in Figure 2-21. The liquid densities in the soil do not fall below 960 kg/m$^3$, so the critical water density limits specified for ss_crit_1 and ss_crit_3 in Table 2-10 are never triggered. However, the liquid saturation fluctuates throughout the outer half of the domain in the $+z$ direction, where the medium becomes unsaturated to as low as 18%. Therefore, the average liquid saturation levels of the waste forms in this region (WF #2 and #3) appear to impart an intermittent effect to criticality events.

The intermittent power output, as influenced by liquid saturation, is plotted in Figure 2-22. For WF #2, intermittent power output occurs as $S_l$ bifurcates about the critical limit of 70% until the loss of vitality terminates the event. For WF #3 (which has no spacer grid mechanism), an intermittent 1 kW criticality occurs around 31.5 days when the 30% limit is met. At 38 days, the steady loss of saturation effectively terminates the criticality event before the original end time of 90 days.

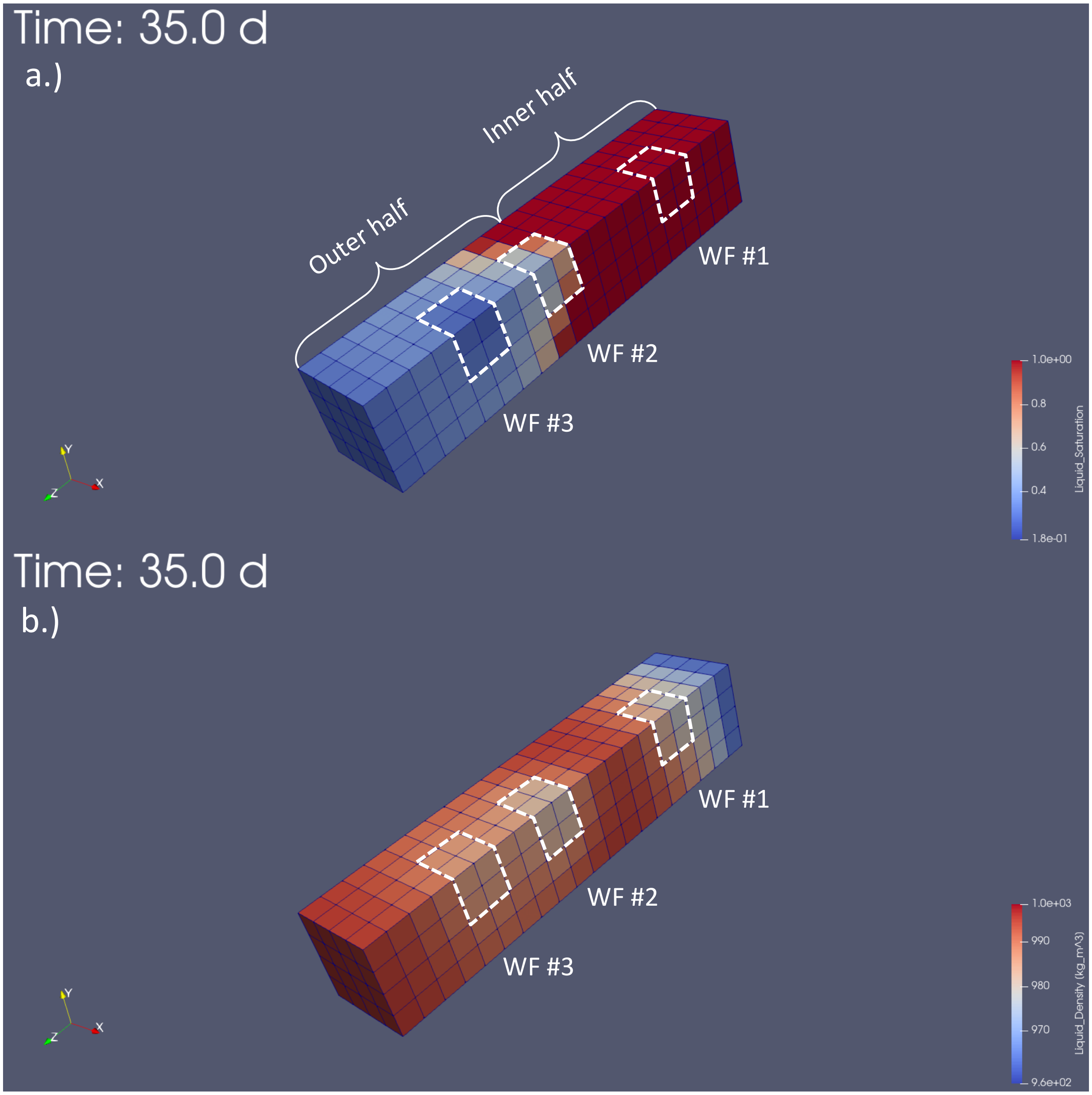

Figure 2-21 The a.) liquid saturation and b.) liquid density at 35 days, when WF #3 nears its critical water saturation and WF#2 oscillates along its critical water saturation.

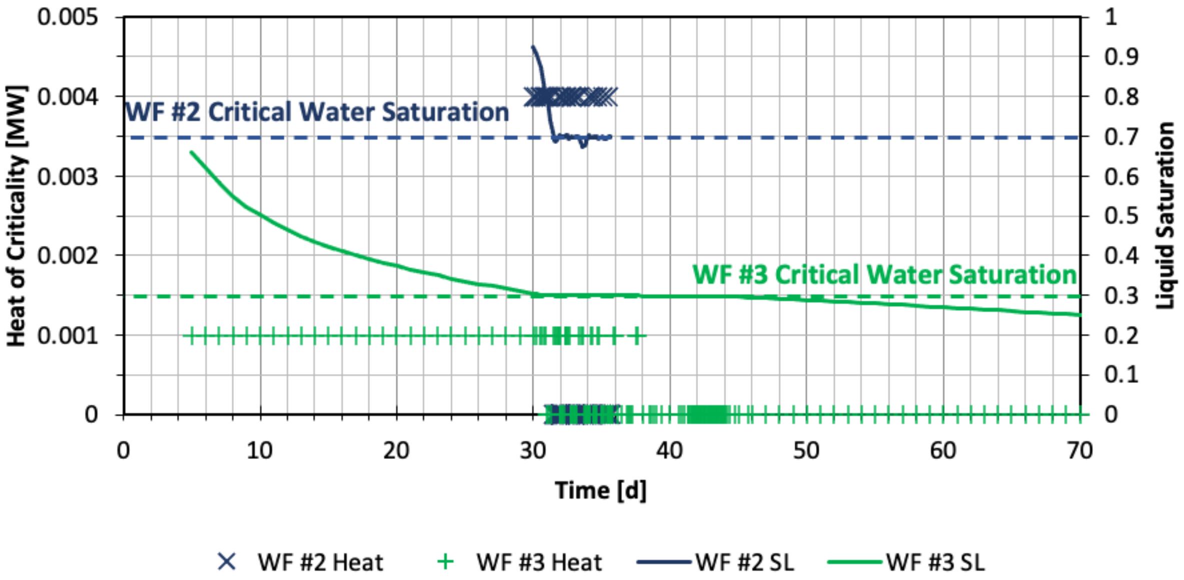

Figure 2-22 Spacer grid vitality and the liquid saturation over time along with lines indicating critical water saturations.

#### 2.2.7.3 *Integrative Test Problem*

**Setup**

A test problem was created to integrate the various new thermal and criticality modeling features in a repository context. It consists of a single DPC emplacement in saturated shale at a depth of 500 m and hydrostatic pressure of 5 MPa. The DPC is surrounded radially by a stainless steel overpack which in turn is surrounded by a 2.1 m thick layer of bentonite buffer. Outside of the buffer is a disturbed rock zone of 1.9-meter extent, which is adjacent to the larger body of shale. Ten-meter plugs of bentonite are modeled on the axial extents of the DPC to represent the buffer separating neighboring waste packages in a repository tunnel (not modeled). The top of the domain lies at 462.5 m below the surface where the geothermal gradient of 20°C/km results in a temperature of 30.719 °C, while the hydrostatic pressure is 4.726 MPa.

Altogether, the model domain is 25 m along the $y$ axis for the axial extent, and 35 m along the $x$ axis and 75 m along the $z$ axis for the radial extent, as shown in Figure 2-23. The mesh was created in Cubit using an input file derived from a quarter-symmetry model employed in earlier base-case simulations (Price et al., 2019). However, full symmetry was employed to assess whether the full set of conduction pathways (i.e., all interfacial vectors) could be successfully utilized by the newly developed TCCs incorporating anisotropy. General dimensions for the DPC were borrowed from a Holtec MPC-32 for the HI-STORM system (Greene et al., 2013) with a length of 5 m and radius of 0.870 m. The cylindrical geometries of the DPC, overpack, and buffer were modeled as 16-sided polygons for meshing purposes. The buffer is separated into two annuli to incorporate different levels of fidelity, with finer discretization applied near the overpack.

The materials applied to each region are shown in Table 2-11 along with their initial properties. The density and heat capacity of the DPC are represented as a mass average of the contents, i.e., the fuel, cladding, spacer grids, basket, canister, and infiltrated water. A default-type TCC is used for all materials except for the DPC, which employs the composite TCC described in Table 2-12 to differentiate between radial and axial behavior. The porosity for the DPC material is the same as that used for the assembly models in the composite TCC. The shale and bentonite are governed by a Leijnse compressibility function with a soil compressibility of $1.6\times10^{8}$, and their tortuosities are modeled as functions of porosity. The buffer is the only material to include S-I transition effects on the permeability, where the illitization model is described in Table 2-13. Here, the values for $A$ and $E_a$ are borrowed from Huang et al. (1993), $[K^+]$ is representative of Opalinus clay (see Chp. 8 in Price et al., 2020), and $C_k$ and $T_{th}$ are discretionary. Sorption effects from the transition were not included in the simulation. The characteristic curves for all materials employed the LCPC unsaturated extension and loop-invariant precomputation, which will be discussed in Section 2.3.1.

A steady-state criticality event occurs in the DPC beginning at 9000 years with a designated end time of 500,000 years. A critical water saturation of 74.8% is defined to be roughly equivalent to the water level of 103.61 cm in the void space of an MPC-32. A critical water density of 905.8 kg/m$^3$ is specified based on Table 4.1 in Davidson et al. (2020). The time-dependent decay heat dataset was borrowed from Price et al. (2019) where there is an initial, maximum output of 4 kW, as shown in Figure 2-24. The heat of criticality is governed either by a constant of 4 kW or the temperature-dependent lookup table plotted in Figure 2-18. The lookup table is devised to have a maximum, steady power output of 4 kW from 0 °C to 90 °C followed by a linearly decreasing power output from 90 °C to 165 °C. The latter range is meant to emulate temperature-driven reactivity feedback effects such as Doppler broadening and thermal expansion of the fuel.

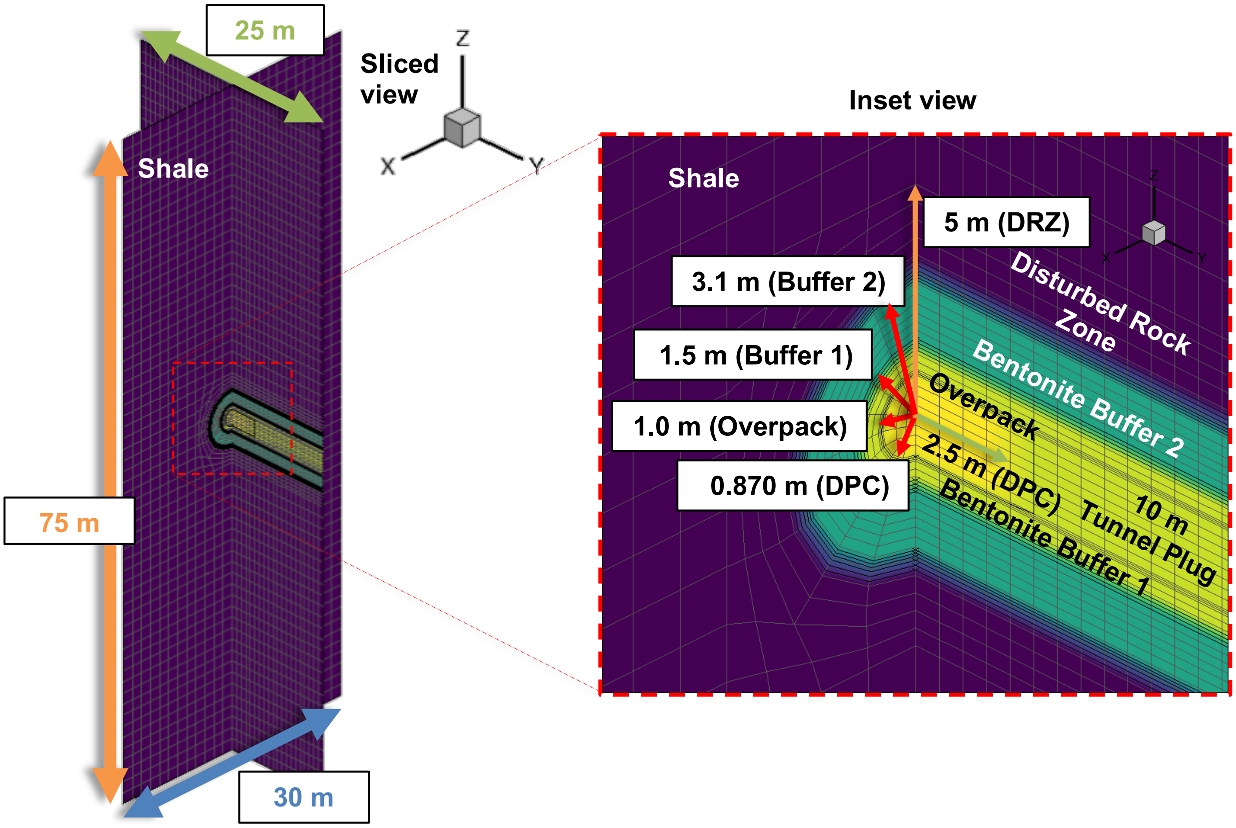

Figure 2-23 Cross sectional views of full-geometry gridded domain in saturated shale.

Table 2-11 The regions in the gridded domain along with initial material properties.

| **Regions** | **Material** | $\varphi$ | $\tau$ | $\rho$ **(kg/m$^3$)** | $c_p$ **(J/kg-K)** | $\kappa$ **(m$^2$)** | **S-I** | **TCC (W/m-K)** |
|---|---|---|---|---|---|---|---|---|
| **all (host rock, DRZ)** | shale | 0.20 | $\varphi^{1.4}$ | 2700 | 830 | $10^{-19}$ | no | D: 0.6-1.2 |
| **buffer (radial, plugs)** | bentonite | 0.35 | $\varphi^{1.4}$ | 2700 | 830 | $10^{-20}$ | yes | D: 0.6-1.5 |
| **overpack** | stainless steel | 0.10 | 1.0 | 7930 | 513.2 | $10^{-16}$ | no | D: 16.7 |
| **wp (DPC)** | Avg. of contents | 0.50 | 1.0 | 3273 | 298 | $10^{-16}$ | no | See Table 2-12 |

Table 2-12 The parameters used to define the TCC for the DPC (cct_dpc_1).

| **PFLOTRAN Input** | **Value(s)** | **Units** |
|---|---|---|
| **THERMAL_CHARACTERISTIC_CURVES** | cct_dpc_axial | |
| **THERMAL_CONDUCTIVITY_FUNCTION** | ASM_AXIAL | |
| **THERMAL_CONDUCTIVITY_WATER** | 0.6190D+0 | W/m-°C |
| **THERMAL_CONDUCTIVITY_SOLID** | 1.4516D+1 | W/m-°C |
| **POROSITY_ASSEMBLY** | 5.0000D-1 | |
| **END** | | |
| **END** | | |
| | | |
| **THERMAL_CHARACTERISTIC_CURVES** | cct_dpc_radial | |
| **THERMAL_CONDUCTIVITY_FUNCTION** | ASM_RADIAL | |
| **THERMAL_CONDUCTIVITY_DRY** | 0.1430D+0 | W/m-°C |
| **THERMAL_CONDUCTIVITY_WATER** | 0.6190D+0 | W/m-°C |
| **THERMAL_CONDUCTIVITY_SOLID** | 1.4516D+1 | W/m-°C |
| **ASM_DRY_COEFFICIENT** | 3.8300D-5 | |
| **ASM_DRY_EXPONENT** | 1.6700D+0 | |
| **POROSITY_ASSEMBLY** | 5.0000D-1 | |
| **END** | | |
| **END** | | |
| | | |
| **THERMAL_CHARACTERISTIC_CURVES** | cct_dpc_1 | |
| **THERMAL_CONDUCTIVITY_FUNCTION** | COMPOSITE | |
| **COMPOSITE_X** | cct_dpc_radial | |
| **COMPOSITE_Y** | cct_dpc_axial | |
| **COMPOSITE_Z** | cct_dpc_radial | |
| **END** | | |
| **END** | | |

Table 2-13 The parameters employed for the illitization model in the buffer material.

| PFLOTRAN input | Value | Units | Parameter |
|---|---|---|---|
| **ILLITIZATION** | ilt_buffer | | |
| **ILLITIZATION_FUNCTION** | DEFAULT | | |
| **THRESHOLD_TEMPERATURE** | 2.50000d+1 | C | $T_{th}$ |
| **EA** | 1.17152d+5 | J/mol | $E_a$ |
| **FREQ** | 8.08000d+4 | L/mol-s | $A$ |
| **K_CONC** | 2.16000d-3 | M | $[K^+]$ |
| **SMECTITE_INITIAL** | 0.95000d+0 | | $f_{S,0}$ |
| **SHIFT_PERM** | 9.99000d+2 | | $C_k$ |
| **END** | | | |
| **TEST** | | | |
| **END** | | | |

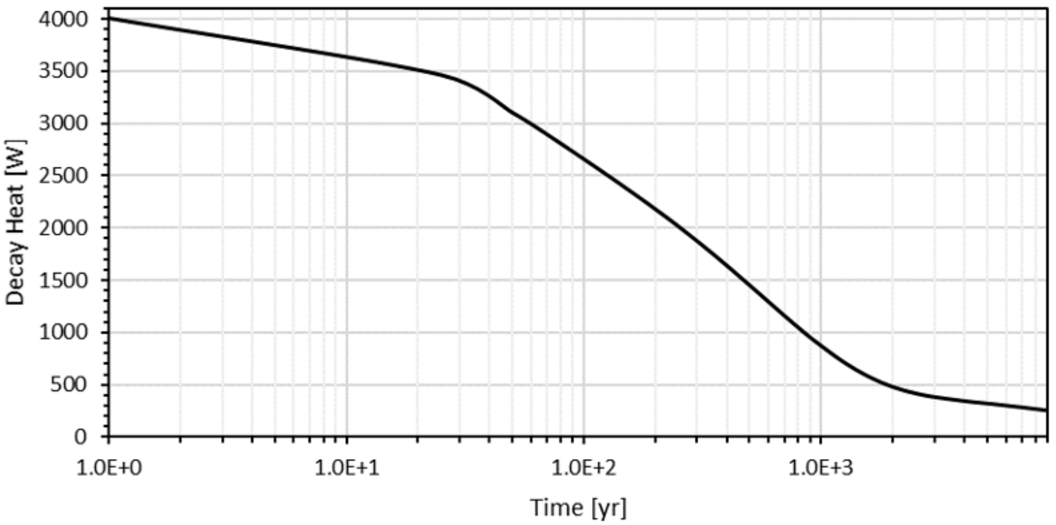

Figure 2-24 Decay heat over time in the DPC up to the start of criticality.

The DPC is governed by the spacer grid degradation model described in Table 2-14. The total mass and surface area of spacer grids is based on 32 Westinghouse PWR assemblies, with 12 grids per assembly. The exposure level of 99.3317% is based on the water level at the tops of the uppermost fuel rods in the basket as approximated from images of the MPC-32. The pre-exponential constant and activation energy are taken from the second stage linear corrosion data provided in Hillner et al. (2000). An output variable for spacer grid vitality was not available at the time of this report, so the vitality was reported manually with print statements extracted from the standard output using a Perl script. To isolate different modeling improvements, simulations were run according to the test matrix in Table 2-15, where improvements were gradually added to the problem setup.

Table 2-14 The parameters employed for the Zircaloy spacer grid degradation model in the DPC.

| PFLOTRAN input | Value | Units | Parameter |
|---|---|---|---|
| **SPACER_DEGRADATION_MECHANISM** | | | |
| **NAME** | spc_01 | | |
| **MASS** | 1.67040D+05 | g | $M_0^{SG}$ |
| **SURFACE_AREA** | 2.37309D+04 | dm^2 | $A_0^{SG}$ |
| **EXPOSURE_LEVEL** | 9.93317D-01 | | $S_l^{exp}$ |
| **C** | 3.47000D+07 | mg/day-dm$^2$ | $C$ |
| **Q** | 2.26750D+04 | cal/mol | $Q$ |
| **END** | | | |

Table 2-15 The test cases for the integrated problem.

| Test | Heat of Criticality | DPC Anisotropy | Spacer Grid Degradation | Buffer Illitization |
|---|---|---|---|---|
| **0** | Constant 4 kW | Off | Off | Off |
| **1** | Constant 4 kW | On | Off | Off |
| **2** | Constant 4 kW | On | On | Off |
| **3** | Constant 4 kW | On | On | On |
| **4** | Lookup table, 4 kW max | On | On | On |

### Anisotropy

Tests 0 and 1 were devised to test the effects of the new composite TCC in PFLOTRAN. In Test 0, the DPC is represented by a constant TCC with the thermal conductivity of stainless steel; therefore, thermal conductivity is independent of saturation and temperature and is isotropic. In Test 1, the composite TCC from Table 2-12 is used to govern conduction along the radial and axial extents of the DPC in the mesh, and both saturation and temperature dependence are preserved.

Figure 2-25 shows temperature contours from the results of both tests at 9010 years (the first time step after the start of the criticality event). The use of the composite TCC, while imparting more realism to the problem, results in a less conductive waste package compared to the isotropic treatment. The center of the DPC remains hotter and exceeds 175 °C. Since the isotropic case is more conductive, a given temperature contour extends further into space. From the axial plots, the contours appear to be more contracted into the radial direction, while there is stronger similarity in the axial ($y$) direction. Altogether, the use of the new thermal conductivity model has been demonstrated to be successful.

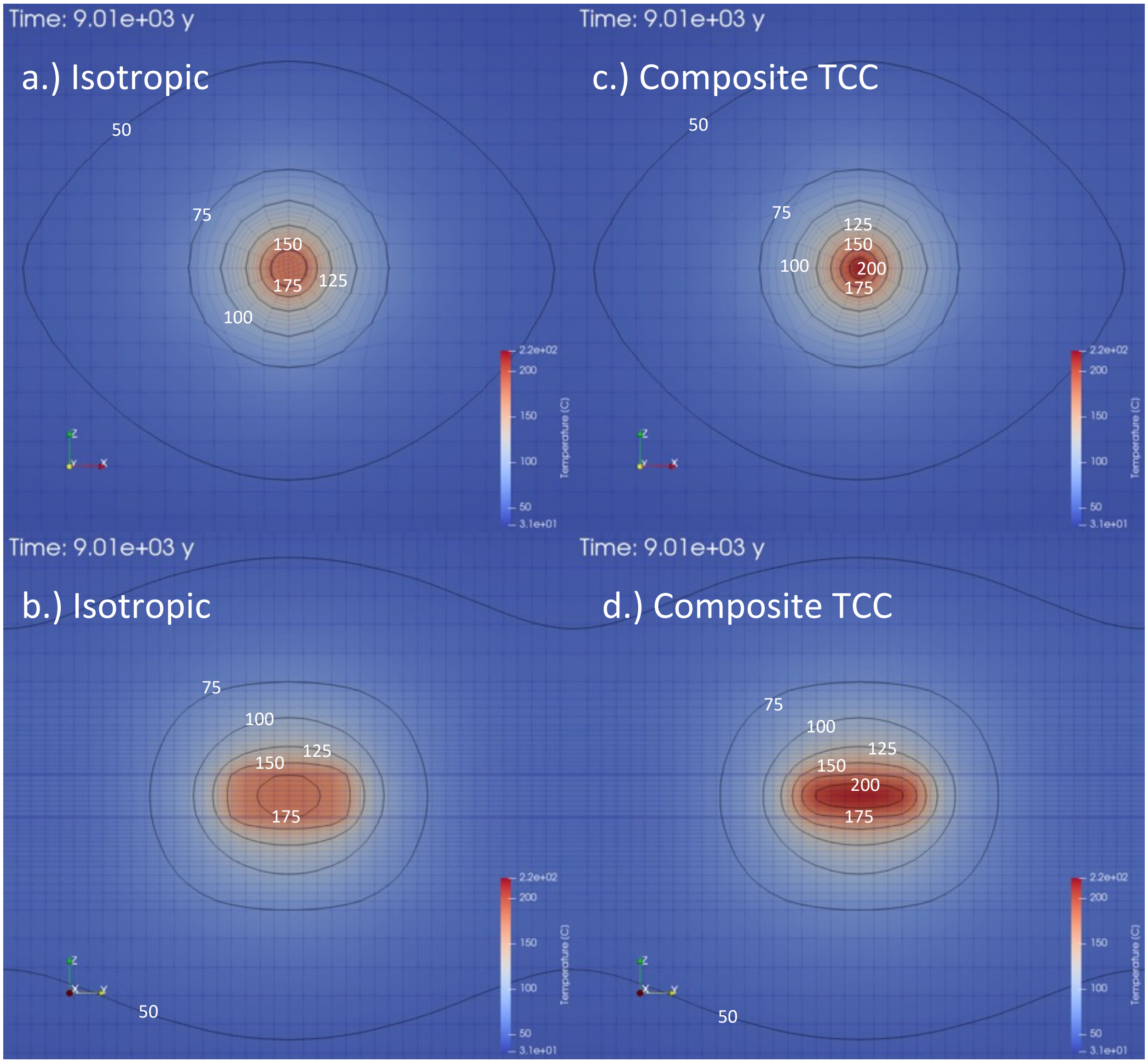

Figure 2-25 Temperature contours for the radial and axial directions of the isotropic test case (a-b) and the anisotropic test case (c-d) with the composite TCC at 9100 years.

### Illitization

Tests 2 and 3 were devised to demonstrate the effects of the illitization model. Test 3 demonstrated that the permeability of the buffer can be modified successfully and affect the results of the simulation. **Error! Reference source not found.** shows the permeability and total concentration of I-129 around the DPC for both tests at 9,200 years. The permeability in Test 3 is shown to increase from the thermal effects of decay heat and criticality, while that of Test 2 remains constant. The Test 3 system demonstrates increased flow through the buffer, which causes I-129 to become less concentrated near the waste emplacement and more diffused in the radial direction.

Tests 2 and 3 failed too soon into the simulation to demonstrate the full extent of permeability changes and corresponding changes on nuclide transport. These failures were caused by solver difficulties during water boiling and rock dryout in the system, which can be addressed with various improvements currently under development that will be discussed in Section 2.3. Results for permeability are therefore shown for Test 4, which was able to proceed to completion at $10^6$ years. Figure 2-26 shows that the permeability indeed increases in the temperature-affected region in the buffer near the DPC, reaching approximately $10^{-17}$ m$^2$ from the original $10^{-20}$ m$^2$.

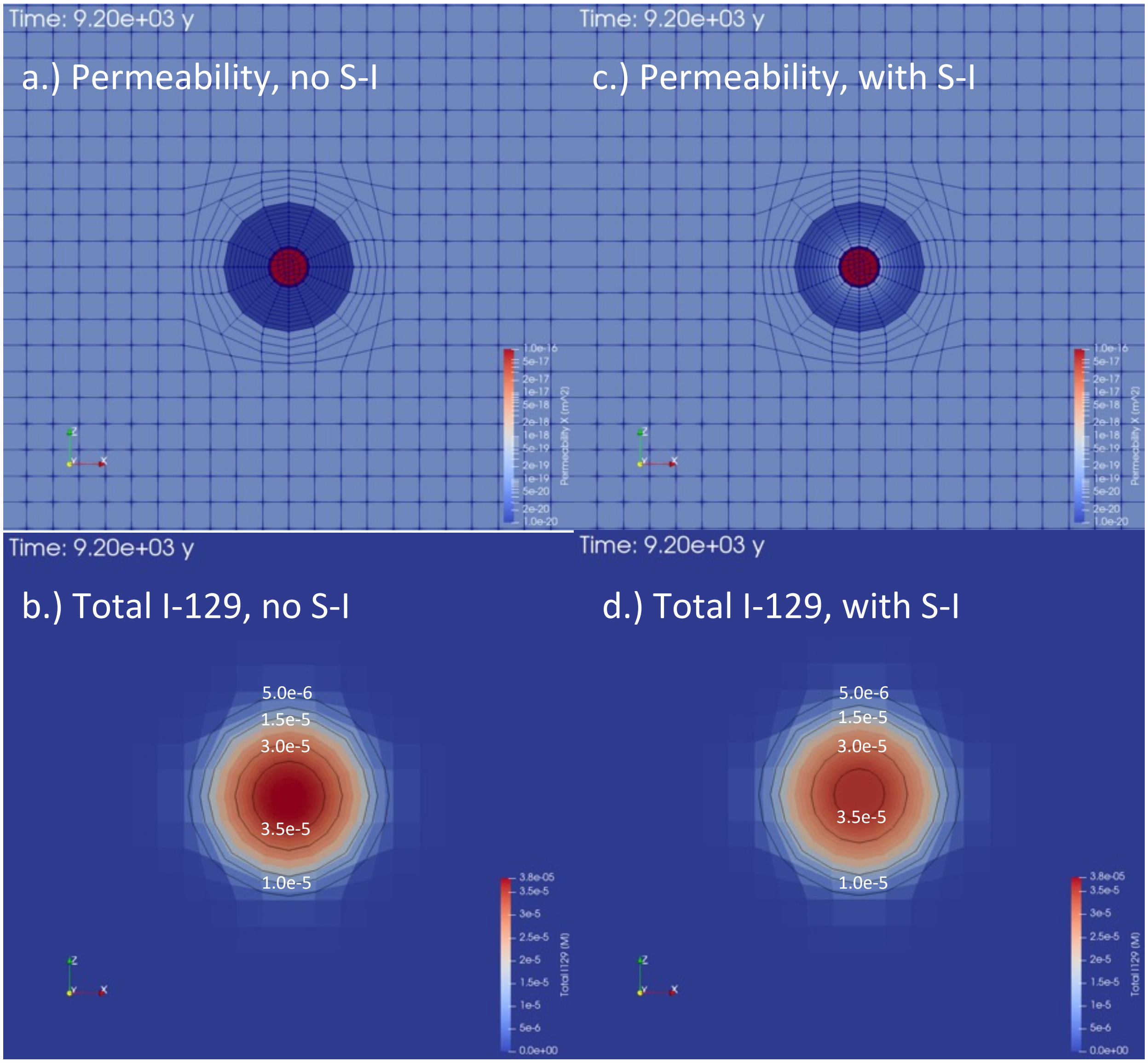

Figure 2-26 Permeability (m$^2$) and total I-129 concentration (mol/L) for Test 2 (a-b) and Test 3 (c-d) at 9,200 years.

### Use of Lookup Table

Tests 3 and 4 were devised to demonstrate the effects of the lookup table option for the heat of criticality. Both tests were successful at demonstrating that the critical water density feature can temporarily halt criticality and introduce intermittent heat emission. However, for Test 3, this effect was not enough to dampen the source term to prevent drying of the system and simulation failure at 9,200 years. In Figure 2-27, this is demonstrated by the relatively higher temperatures and lower liquid densities in the constant heat treatment compared to the lookup table. The lookup table employs reduced power output in the range of temperatures above 90 °C, thus allowing the additional effects from Doppler broadening and thermal expansion to reduce thermal loading in the engineered barrier system. These combined effects allowed Test 4 to not dry out and run to the end of the simulation time.

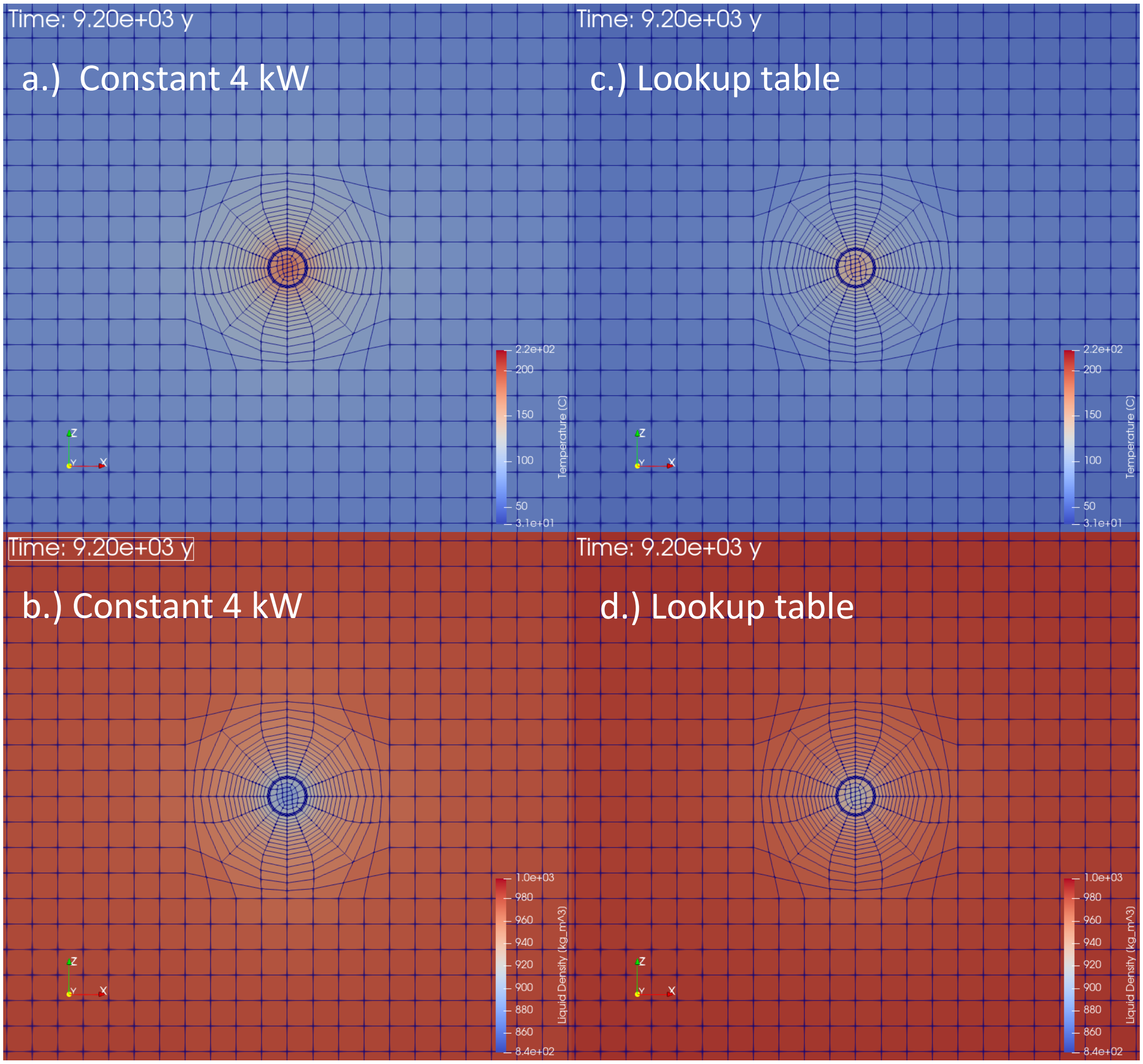

Figure 2-27 Temperature and liquid density for Test 3 (a-b) and Test 4 (c-d) at 9,200 years.

**Spacer Grid Degradation**

While Tests 1 and 2 were devised to inspect the role of spacer grid vitality, they both failed before the full extent of degradation could be realized. Only Test 4 was able to proceed through the full criticality period. Figure 2-28 shows the spacer grid vitality over time in Test 4, where 25% of the spacer grid mass is affected by $7.4\times10^4$ yr, 50% at at $1.8\times10^5$ yr, and 75% by $3.0\times10^5$ yr. Ultimately, the failure criterion of 1% is surpassed at $4.3\times10^5$ yr, preempting the user-defined criticality end time of $5.0\times10^5$ yr and limiting heat emission to approximately 10 W from decay.

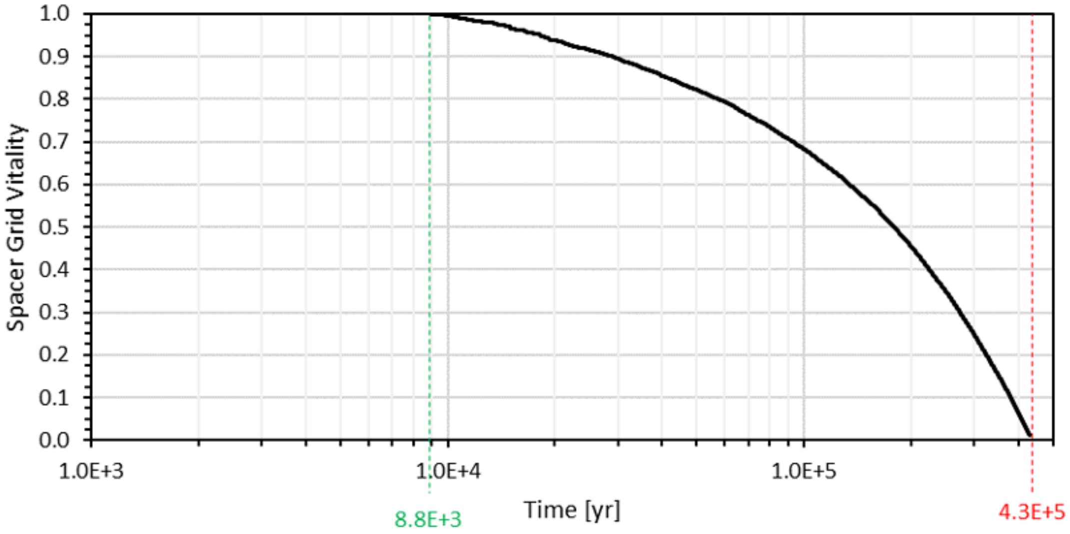

Figure 2-28 Spacer grid vitality from the canister breach time to the failure time of $4.3\times10^5$ years during the test employing the criticality heat lookup table.

## 2.3 Performance Improvements

### 2.3.1 Characteristic Curve Smoothing

Two of the most widely utilized capillary pressure curves, Brooks-Corey (1964) and van Genuchten (1980), exhibit physically unrealistic behavior at low degrees of water saturation. In both cases, these empirical curve fits project capillary pressure to approach infinity at a "residual" or "irreducible" saturation. For example, in the van Genuchten (1980) model, capillary pressure $P_c$ is defined for a given wetting phase saturation $S_w$ above residual saturation $S_r$ as follows:

$$\frac{S_w - S_r}{1 - S_r} = (1 + (\alpha P_c)^n)^{-m}. \qquad \text{Equation 2.3-1}$$

Here $\alpha$, $m$, and $n$ are empirically determined constants unique to the material. Below residual saturation, the van Genuchten model for capillary pressure is undefined.

The second characteristic curve relates relative permeability of the liquid and gas phases to the degree of saturation. In the Burdine (1953) and Mualem (1976) relative permeability models, liquid permeability is found by integrating the inverse of capillary pressure. Because capillary pressure in the Brooks-Corey and van Genuchten models approaches infinity at the residual, relative permeability approaches zero at the same limit. Thus, water saturation at residual saturation is irreducible by mechanical drainage. Water saturation can nevertheless be reduced below "irreducible" by evaporative processes, as evaporation is independent of permeability. In particular, the decay heat of the waste packages in an unsaturated geologic repository has the potential to drive water content below irreducible in the proximity of the waste.

In previous versions of PFLOTRAN, the capillary pressure curve was abruptly limited to a specifiable maximum capillary pressure. Thus, if the capillary pressure model predicted an unallowably high value of capillary pressure, it was overwritten with the designated maximum value. While this accomplished the goal of limiting capillary pressure to reasonable numbers and provides a simple model below residual saturation, it also has the effect of introducing a corner when the capillary pressure curve intersects the designated maximum. Discontinuous derivatives, such as at a corner, will result in slowly or non-convergent behavior when using Newton's method, even though the function value is itself continuous. Alternative numerical methods, such as the secant or Trust Region are necessary to solve these problems.

However, the existence of a corner is not rooted in any physical theory but is rather a numerical anomaly of two imperfect empirical models. Here, extensions to the van Genuchten capillary pressure below residual saturation were implemented primarily to improve computational efficiency, but also have a theoretical basis.

#### *2.3.1.1 Capillary Pressure below Residual*

The conventional definitions of capillary pressure states that the capillary pressure $P_c$ is the difference in pressure between the nonwetting $P_{nw}$ and wetting $P_w$ phases (Bear 1972).

$$P_c = P_{nw} - P_w \qquad \text{Equation 2.3-2}$$

This definition contains an apparent paradox as the capillary pressure is limited to the pressure of the non-wetting phase, lest the wetting fluid be at negative absolute pressures (Gray and Hassanizadeh 1991). Yet, for water in geologic materials, capillary pressure frequently exceeds the non-wetting atmospheric pressure. At the same time, it is assumed that the density of the wetting fluid remains constant despite being at vacuum or negative pressures. If the wetting fluid were truly under zero or negative hydrostatic pressure in the thermodynamic sense, the fluid would expand within capillaries. In reality, the capillary pressure is an anisotropic tensor quantity and cannot be fully described in terms of a scalar thermodynamic pressure (Kralchevsky et al. 1994).

Using Gibbs (1961) theory of capillarity, water flows to reduce the free energy of the system. Typically, flow occurs from regions of high pressure to low pressure to lower mechanical potential, but total free energy can be balanced by other mechanisms, for instance gravitational potential. Water can rise in a capillary tube not because the mechanical pressure in the capillary is significantly lower but because water is at a lower chemical potential in proximity of a wetted solid surface. The term matrix potential is also used in this framework to avoid connoting changes in the scalar thermodynamic pressure. Here, capillary pressure considered to be equivalent to matrix potential, but the capillary pressure nomenclature will be maintained for consistency.

#### *2.3.1.2 Capillary Pressure Extensions*

There have been numerous suggested extensions or replacements to the van Genuchten model of capillary pressure below the residual as previously reported by Webb (2000), Sun et al (2010), and others. Models such as Rossi and Nimmo (1994) replace the entirety of the curve to avoid piecewise junctions but represent an entirely new class of capillary pressure functions rather than a modification to van Genuchten.

The typical extension is either linear or exponential (also known as logarithmic for its inverse). The linear extension has the advantage of preserving a slightly larger domain for the original empirical curve fit but has not been shown to fit oven dried sample data. The exponential extension is consistent with the data of Campbell and Shiozawa (1992). However, this represents a limited sample size of primarily silicate rocks and may not be applicable to all geologic materials. The true behavior in a heterogeneous mixture of mineral surfaces has not yet been studied.

If either a linear or exponential extension is chosen, there is a single degree of freedom to enforce continuous values and derivatives. Thus, either the maximum capillary pressure at oven-dry conditions or the saturation at the piecewise junction point can be specified. In this update to PFLOTRAN, either method of specification is permitted using the existing keyword MAXIMUM_CAPILLARY_PRESSURE or the new keyword LIQUID_JUNCTION_SATURATION. Additionally, a quadratic extension option is provided that is specified by giving both parameters. To preclude degenerate capillary pressure values and numerical instabilities as a result, the quadratic extension is only permitted if the resulting parabola is monotonic over the domain. The quadratic fit preserves more of the empirical curve fit than either the linear or exponential extensions. Table 2-16 lists the unsaturated extension specifications options for the van Genuchten capillary pressure model. The acronyms utilized in Sun et al (2010) were utilized for the constant, exponential, and linear extensions.

Table 2-16 Implemented van Genuchten unsaturated extension specification statements. F=Flat or constant, E=Exponential, L=Linear, CPC=Capillary-Pressure Cap, NOC=NO Cap.

| **Keyword** | **Extension** | **MAXIMUM_CAPILLARY_PRESSURE** | **LIQUID_JUNCTION_SATURATION** |
|---|---|---|---|
| NONE | None | | |
| FCPC | Constant | X | |
| FNOC | Constant | | X |
| ECPC | Exponential | X | |
| ENOC | Exponential | | X |
| LCPC | Linear | X | |
| LNOC | Linear | | X |
| QUAD | Quadratic | X | X |

The previous default MAXIMUM_CAPILLARY_PRESSURE value of 1 GPa / $10^9$ Pa was retained. This value is within the range of values calculated by Webb (2000). A default value of 5% effective saturation was adopted for LIQUID_JUNCTION_SATURATION, which is consistent with the default behavior in the code NUFT (Nonisothermal Unsaturated Flow and Transport) developed by Lawrence Livermore National Laboratory (Sun et al 2010). Both defaults are utilized in the quadratic extension if not specified otherwise. To illustrate these options, the constant, linear, and exponential extensions to the van Genuchten model with default parameters are plotted in Figure 2-29.

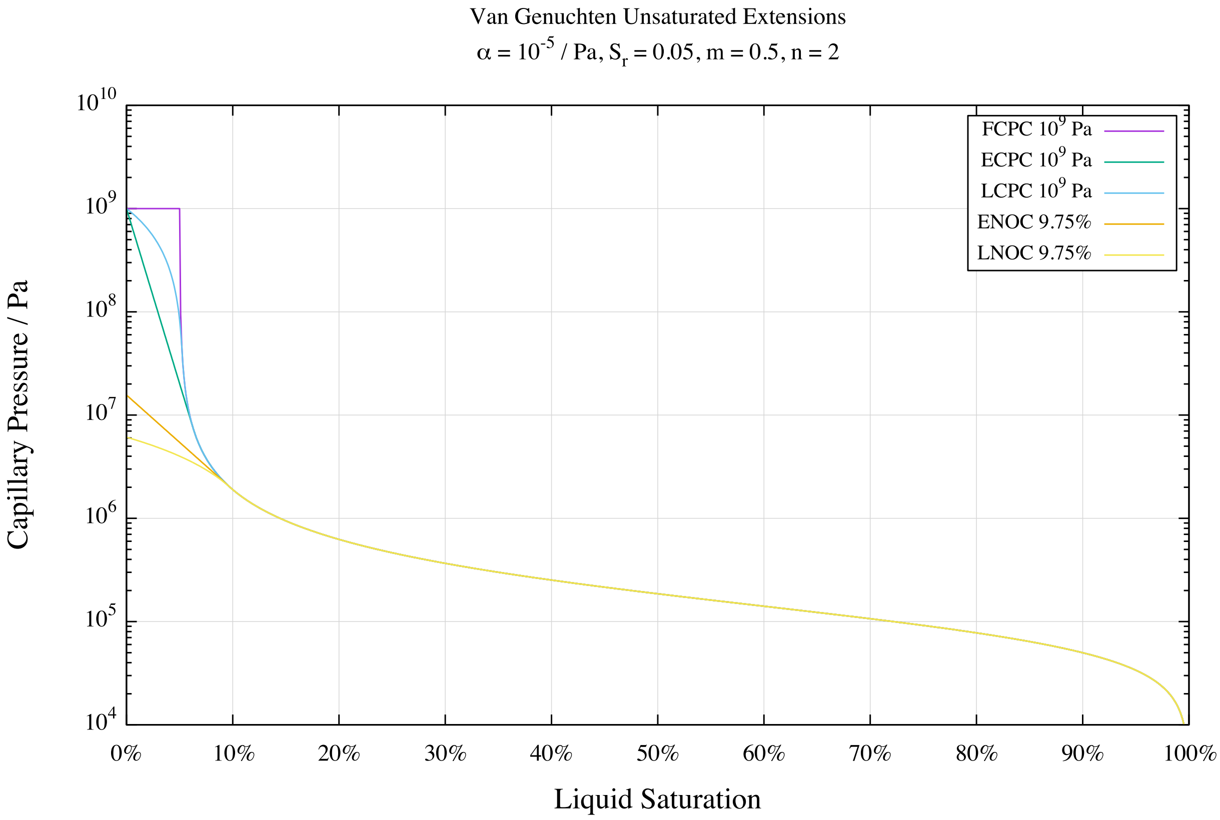

Figure 2-29 Van Genuchten capillary pressure function employing various extensions at the unsaturated limit

There are a few necessary constrains on these parameters to ensure the resulting function is continuously differentiable. If the LIQUID_JUNCTION_SATURATION is specified, it must logically exceed the LIQUID_RESIDUAL_SATURATION to avoid an undefined region in the in the van Genuchten model.

Similarly, there is a minimum MAXIMUM_CAPILLARY_PRESSURE that is determined by the parameters ALPHA and M. The minimal value can be determined by extrapolating a linear or exponential extension from the inflection point (in linear or logarithmic space, respectively) of the ordinary van Genuchten curve. If the specified capillary pressure limit does not exceed this minimum, the simulation will abort at input deck read time.

### *2.3.1.3 Relative Permeability*

Relative permeability of the wetting and non-wetting phases is frequently calculated by either the Burdine or Mualem models. In both models, the relative permeability of the wetting phase is calculated, in part, by integrating the inverse of capillary pressure with respect to current saturation. In the Burdine model, relative permeability of the wetting phase, $k_{rw}$, with respect to saturation $S_w$ follows:

$$k_{rw}(S_w) = \left(\frac{S_w - S_r}{1 - S_r}\right)^2 \frac{\int_0^1 \frac{dS_w}{P_c^2}}{\int_0^1 \frac{dS_w}{P_c^2}}. \qquad \text{Equation 2.3-3}$$

Here, $S_r$ is the residual saturation. The Mualem model is similar but varyies in the weighting of the parameters.

$$k_{rw}(S_w) = \sqrt{\frac{S_w - S_r}{1 - S_r}} \left[\frac{\int_0^1 \frac{dS_w}{P_c}}{\int_0^1 \frac{dS_w}{P_c}}\right]^2 \qquad \text{Equation 2.3-4}$$

Using capillary pressure model in Equation 2.3-1, van Genunchten (1980) demonstrated that both the Burdine and Mualem relative permeability functions have a closed form analytic solution for certain values of $m$ and $n$. In particular, the Burdine model is closed form if $m = 1 - 2/n$. Similarly, the Mualem model is closed form if $m = 1 - 1/n$. For most other combinations of $m$ and $n$, the relative permeability integrals result in the incomplete beta function, which must be evaluated using a numerical approximation. Thus, there is a significant computational advantage to having a closed form solution to these integrals by constraining n and m rather than finding the best possible fit for capillary pressure or relative permeability. The use of the constraint $m = 1 - 1/n$ for the closed-form Mualem integral has become nearly synonymous with the van Genuchten model and is the only current option for capillary pressure in PFLOTRAN. The option to choose the Burdine constraint, so that the capillary pressure and relative permeability models are self-consistent, is being included in a future update.

Additionally, because the unsaturated extensions implemented here are intended to deviate from the classic VG curve only near the residual limit, where the capillary pressure is exceedingly high, the choice of unsaturated extension will negligibly affect the estimated relative permeability from either model. As both the Burdine (1953) and Mualem (1976) models were developed assuming bulk flow, there is insufficient evidence these are applicable to film flow which is expected to dominate below residual saturation. Thus, at present, the relative permeability functions are independent of the unsaturated extension to capillary pressure and the relative permeability of the wetted phase remains zero below residual saturation.

#### *2.3.1.4 Loop-Invariant Parameters*

To speed performance of the Van Genuchten curves with any extension, precomputation of loop-invariant parameters is now explicit. A set of canonical independent parameters is specified to construct the van Genuchten saturation function object, whose member functions are invoked at run-time derived values. Values that are independent of any particular saturation are cached in the object and are available for rapid computation of capillary pressure or relative permeability. Performance gains using this technique vary as some compilers, notable Intel Fortran, are capable of performing this optimization for simple calculations. However, performance improvement is significant in debug mode with any compiler.

Explicit precomputation is essential when intermediate parameters are complex. This is notably the case when calculating the piecewise junction point when a maximum capillary pressure is specified. Determination of the linear or exponential extension requires iteratively solving a system of non-linear equations and thereby cannot be reasonably performed during each function call. However, as it is a loop-invariant parameter, it is only necessary to conduct the iterative solution once per simulation at input deck read time. The results are then internally cached for later use. Furthermore, by precomputing the junction saturation, the piecewise function branch can be selected earlier in the function call. This then avoids expensive exponentiation operations in the ordinary van Genuchten domain when the piecewise extension is applicable.

To enable loop-invariant precomputation, the new keyword LOOP_INVARIANT must be invoked. Because precomputation is essential for the unsaturated extensions, all the aforementioned unsaturated extensions require that the loop invariant option be enabled.

#### 2.3.1.5 Saturated Limit

The derivative of the van Genuchten capillary pressure at full liquid saturation is, analytically, infinite. In previous versions of PFLOTRAN, this singularity was handled by returning a zero derivative. In the LOOP_INVARIANT version of van Genuchten, the derivative at the saturation limit has been replaced with a finite difference approximation. Because floating point arithmetic is discrete, the Fortran intrinsic epsilon is utilized to minimize the domain of the approximation. Because the van Genuchten capillary pressure at saturation is exactly equal to zero at saturation, the finite difference approximation is implemented as follows:

$$\lim_{\epsilon \to 0^+} \frac{dP_c(1-\epsilon)}{d(1-\epsilon)} \to \frac{P_c(1)-P_c(1-\epsilon)}{1-(1-\epsilon)} = -\frac{P_c(1-\epsilon)}{\epsilon} \qquad \text{Equation 2.3-5}$$

Replacing the discontinuous analytic derivative at the saturated limit with a finite approximation is expected to improve the rate of convergence in saturated systems. This approximation is invoked only when water saturation exceeds $1-\epsilon$. The exact value of epsilon will vary by system, but for a 64-bit IEEE floating point value, epsilon is approximately $1.2\text{x}10^{-7}$. The analytic derivative over the rest of the saturation domain remains calculated as before.

### 2.3.2 Linear Solvers

This year, significant development effort was invested in optimizing linear solver capabilities. Specifically, this effort was undertaken for miscible/immiscible, isothermal/nonisothermal, multiphase flow problems. Such systems are described in PFLOTRAN by solving a coupled system of PDE's describing conservation of water and air mass. For this system of equations, two primary unknows are required to be solved for at each timestep; these primary unknowns are liquid pressure and gas saturation and are represented by the vector $\boldsymbol{x}$ in the following equation, which describes the Newton-Raphson nonlinear solution search method:

$$J d\boldsymbol{x} = -R \qquad \text{Equation 2.3-6}$$

where $J$ is the Jacobian matrix, and R is the residual vector. The Jacobian matrix, linearized by the Newton-Raphson method, is composed of the derivatives of the discrete form of the pressure and saturation governing equations with respect to the primary dependent variables. Each grid cell has two unknowns, $p_w$ and $s_g$, and generates a 2 × 2 Jacobian block as:

$$\begin{bmatrix} \dfrac{\partial F_w}{\partial p_w} & \dfrac{\partial F_w}{\partial s_g} \\ \dfrac{\partial F_g}{\partial p_w} & \dfrac{\partial F_g}{\partial s_g} \end{bmatrix}_n \begin{bmatrix} \delta p_w \\ \delta s_g \end{bmatrix} = - \begin{bmatrix} F_w \\ F_g \end{bmatrix}_n . \qquad \text{Equation 2.3-7}$$

where $F_w$ and $F_g$ are residuals of the two unknowns. As one can imagine, increasing the number of grid cells will quickly increase the size of the system of equations. According to Valgrind (Nethercote et al., 2007), a code profiler, for a given problem in PFLOTRAN, approximately 31% of computation time is spent on solving the linear system, 18% is spent calculating the residuals, and 51% is spent on computing the Jacobian. The later section will focus on the 31%, the performance of the linear system solver, to improve the overall computation time. Later sections will also describe improvements to the nonlinear solver for better-optimized step and direction of the solution update to reduce the overall number of nonlinear iterations, which will reduce the number of linear solves, Jacobian computations, and residual calculations.

#### Constrained Pressure Residual Preconditioner for Linear Solver

When running simulations of large-scale engineered systems involving heterogeneous porous media, traditional Krylov solver methods (e.g., BiCGSTAB and ILU; Saad et al., 1993) can fail to find a solution. Because of the elliptic PDE nature of the pressure governing equation, one possible approach to address Krylov solver failure is to implement a CPR 2-stage type preconditioner. Preconditioners accelerate a linear solver's computational performance by transforming the original system into a more relaxed system of linear equations.

PFLOTRAN's default solver is the BiCGSTAB solver and ILU(0) preconditioner (Saad et al., 1993). This combination is deficient for large-scale repository simulations. To overcome this deficiency, advanced linear solver techniques needed to be added to the code. Advancements in computational performance for these types of problems have been achieved through a number of efforts elsewhere in the porous media flow simulation community. These include algorithms like Hammersley-Ponting (Ponting et al., 2008) and Bui (Bui et al., 2017), which apply a two-stage combinative CPR AMG preconditioner. To apply CPR efficiently, this approach applies two different methods to decouple the pressure matrix from the global matrix and is named quasi-implicit pressure, explicit saturation, or QIMPES (LaCroix et al., 2001) and alternate block factorization, or ABF (Bank et al., 1989). The Flexible Generalized Minimal Residual method, or FGMRES, is preferred over traditional GMRES or BiCGSTAB because it can accommodate changing preconditioners, like CPR.

Therefore, a combination of FGMRES, CPR, and ABF seems to be effective for simulation domains with large contrast in permeability and unstructured grids, because the preconditioner maintains communications with decomposed domain ghost grid cells unlike block Jacobi with ILU preconditioner which are the most widely used preconditioners in porous media flow simulations. The combination of these preconditioner, linear, and nonlinear solvers has been effective in very complex constitutive models, heterogeneous domains, and unstructured grids.

### 2.3.3 Nonlinear Solvers

Let's say there is a function $F$ describing the governing conservation equations for flow in porous media. The sum of accumulation, flux, and sources/sinks must equal zero for mass conservation; thus, the goal of a solver is to solve $F(x) = 0$. To achieve this for nonlinear systems, iteration is required, and we reach the iterative solution $u^*$ by using Newton's method that satisfies $F(x^*) \approx 0$. The idea is to begin with an initial guess $x_0$ and approximate the function $F$ by solving the linearized system of equations. Then using the zero of this linear model as the second guess, the next iteration $k = 1$ is computed. The process is repeated until the satisfactory convergence criteria are met.

The linear model is constructed when we expand $F$ about $x_k$ in a Taylor series and truncate after the linear term. We get:

$$F(x) \approx F(x_k) + F'(x_k)(x - x_k) = F_{linear}(x). \qquad \text{Equation 2.3-8}$$

The goal now is to solver $F_{linear}(x_{k+1}) = 0$, which gives the equation

$$F'(x_k)s_k = -F(x_k) \qquad \text{Equation 2.3-9}$$

where $s_k = \mathit{\Delta} x = (x_{k+1} - x_k)$, which is the Newton direction and step, and $F'(x_k)$ is the Jacobian $J(x_k)$. When the linear system of equations is solved, the norms are calculated to see if $||F(x_{k+1})||$ is less than $||F(x_k)||$. Optimization problems commonly use the 2-norm as the measurement, and the definition of the 2-norm of $F(x)$ is

$$||F(x)||_2 := \left(\int F(x)^2 dx\right)^{1/2} \qquad \text{Equation 2.3-10}$$

and discretely written as

$$||F(x)||_2 = (\sum_{i=1}^{n} F_i\,(x)^2)^{1/2}. \qquad \text{Equation 2.3-11}$$

If we are looking for the solution of $||F(x)||_2 = 0$, we are really looking for the minimum of a quadratic function such as

$$f(x) := \frac{1}{2}||F(x)||_2^2 : \mathbb{R}^n \to \mathbb{R}. \qquad \text{Equation 2.3-12}$$

Finding the minimum of this function achieves the global unconstrained minimization

$$\min_{x \in \mathbb{R}} \{f(x) = \frac{1}{2} F(x)^T F(x)\}. \qquad \text{Equation 2.3-13}$$

#### *2.3.3.1 Newton trust-region dogleg Cauchy (NTRDC) Nonlinear Solver*

A new type of nonlinear solver, called Newton Trust-Region Dogleg Cauchy (NTRDC), has been implemented into PETSc, PFLOTRAN's parallel solver toolkit. The solver is still under testing and so is considered an unofficial capability for PETSc, but it is expected to be released in an upcoming version. NTRDC is more capable of resolving complex nonlinear constitutive models than traditional Newton-Raphson solvers. NTRDC can optimize the solution from the linear solver further by re-evaluating the residuals within its inner-iteration algorithm in a similar manner to line-search backtracking but much more intelligently. In contrast to Newton's method, which only guarantees local convergence and will fail with discontinuous constitutive models, NTRDC guarantees global convergence and handles discontinuities. NTRDC has an inner iteration optimization problem to solve to determine the most proper size of the trust region. Eq. 2.3-16 is the trust region sub-problem.

$$m_k(\vec{p}) = f_k + g_k^T \vec{p} + \frac{1}{2}\vec{p}^{\,T} B_k \vec{p} \quad s.t. \quad ||\vec{p}\,|| <= \Delta_k \qquad \text{Equation 2.3-14}$$

where $k$ is the iteration number, $\vec{p}$ is the solution update inside of the inner iteration (distinct from $\vec{x}$), $\Delta_k$ is the $k$th trust region radius, $f = \frac{1}{2}F^T F$ , $g_k = J^T F$, and $B_k = J^T J$ which approximates the Hessian matrix. Here we're trying to minimize the function $m_k(\vec{p})$. If the ratio $\rho$ of actual improvement (numerator) to the predicted improvement (denominator) in Eq. 2.3-17 is satisfied, then $\vec{p}$ is the improvement direction and step of the solution $\vec{x}$:

$$\rho_k = \frac{f(x_k) - f(x_k + p_k)}{m_k(0) - m_k(p_k)} \qquad \text{Equation 2.3-15}$$

If $\rho >= \eta_1$, then the inner iteration of the TR sub-problem is solved and the algorithm moves on to the next outer Newton iteration. If $\rho >= \eta_3$, then the trust region is expanded for the next Newton iteration, if $\rho <= \eta_2$ the trust region is shrunk. If $\rho$ is in between $\eta_2$ and $\eta_3$, then it keeps the trust region size. $t_1$ and $t_2$ are the factors that are determine how to scale (shrink or expand, respectively) the trust region.

Typical values for these input parameters are $0 \leq \eta_1 = 0.001 \leq \eta_2$, $\eta_2 = 0.25$, $\eta_3 = 0.75$, shrinking factor $t_1 = 0.25$, and expanding factor $t_2 = 2.0$.

If the Newton solution update generates $\rho < \eta_1$, the Cauchy Point (CP) method attempts to improve the solution update in the NTRDC solver. CP takes the steepest descent direction and the step size of the solution update which is dependent on the trust region $\Delta$. The CP solution update is written as

$$s_k = -\frac{||\nabla f_k||^2}{\nabla f_k^T B_k \nabla f_k} \nabla f_k. \qquad \text{Equation 2.3-16}$$

If neither CP nor the Newton solution update satisfies the trust region, then the algorithm combines both solutions in ratio by solving the quadratic equation for $\tau$:

$$\Delta = ||s_k^{cy} + \tau(s_k^{nt} - s_k^{cy})||_2. \qquad \text{Equation 2.3-17}$$

Here $cy$ and $nt$ are the Cauchy and Newton solution update, respectively.

#### 2.3.3.2 Scaling Solution Vector for Isothermal Immiscible Two-phase Flow

Proper scaling of the solution update vector and Jacobian is helpful for any advanced nonlinear solvers that measure L2 norms to determine whether the Newton solution update direction and step-size are suitable for optimization. For the Newton Trust Region Dogleg Cauchy method (NTRDC, described below) the entire inner iteration must be properly scaled to truly take advantage of the robustness of the algorithm. In our simulator, the pressure unknown variable is in the units of Pa and saturation unknown variable is dimensionless between 0 and 1. This means the solution update vector has two discrete ranges of values: for example, a new pressure update could arbitrarily range between, e.g., 0 and 1000 Pa (though it is not technically bounded), while a new saturation update could range between, e.g., 0 and 0.1 in the simulation domain for this hypothetical nonlinear iteration. The L2 norm is defined as

$$||\vec{x}||_2 = \sqrt{x_{1,p}^2 + x_{1,s}^2 + x_{2,p}^2 + x_{2,s}^2 + \ldots + x_{n,p}^2 + x_{n,s}^2}. \qquad \text{Equation 2.3-18}$$

In the given example, one can see that pressure values on the order of hundreds in the solution update vector can completely diminish saturation values on the order of one one-hundredths, making the L2 norm an ineffective constraint for the nonlinear solvers. Therefore, the two quantities must be scaled properly by measuring the infinity norm of each quantity and normalizing, so both quantities in the solution range between 0 and 1.

$$p_\infty = ||\vec{x}_p||_\infty = \max|x_{i,p}| \text{ and } s_\infty = ||\vec{x}_s||_\infty = \max|x_{i,s}| \qquad \text{Equation 2.3-19}$$

All the pressure values in the solution update are scaled by $p_\infty$, the saturation values are scaled by $s_\infty$, and the Jacobian is column scaled by the stride vector, $[p_\infty, s_\infty, ..., p_\infty, s_\infty]$. The effect of scaling is discussed in the numerical experiment section.

#### *2.3.3.3 Accommodating Primary Variable Switching in Nonlinear Solvers*

The nonisothermal miscible multiphase flow simulator requires primary variable switching to represent three different states with three different governing equations and unknowns: liquid phase, two-phase, and gas phase. The nonlinear solver must resolve the solution and determine each grid cell's state in the domain within the physical boundaries. Sometimes the solution can converge in one set of states, but because the calculated unknowns are beyond the physical boundaries, it must change to a different set of states and retry to converge in that state. For example, if the converged solution is such that liquid saturation drops to zero, then the state of the grid cell must transition into the gas phase from the two-phase state. We implemented two algorithms that integrate with the NTRDC nonlinear solver so that primary variable switching is handled properly. If the phase state is not controlled in the inner iteration of the NTRDC solver, the solver will fail to converge trying to find a solution in an undetermined phase state.

### 2.3.4 Numerical Experiments

#### *2.3.4.1 Immiscible Isothermal Two-phase Flow Performance Improvements*

**Description of Numerical Simulation Case Study**

Three test case scenarios were performed on the same domain with different numerical difficulty for simulating immiscible isothermal flow. The Easy Case simulates an undisturbed bedded salt nuclear waste repository without disruption from closure through the 10,000-year simulation period. There are material changes throughout the domain as the run-of-mine salt closures reconsolidate and the disturbed salt rock above and below the excavated regions self-heals, returning the porosity and permeability to near the intact salt values.

The Mid Case simulates all the Easy Case material changes but includes a hypothetical human intrusion event where the borehole is drilled into the repository at 1000 years after the simulation begins. In this scenario, the time step size changes from months or years to minutes to simulate the transient flow process through an intruding borehole that has very high permeability compared to the salt rock formation. Such scenarios cause a dramatic perturbation in temporal, spatial, and permeability scales.

The Hard Case includes two events: one borehole intrusion into the repository at 350 years and a second borehole intrusion through the repository into an over-pressured brine reservoir at 1000 years. This event can potentially flood the under-saturated waste repository.

The domain has a total of 460,020 grid cells or 920,040 unknowns and consists of 41 different rock/soil types with 12 different capillary pressure and relative permeability relations (Council, 1996) (Frederick, 2020). The simulation also includes gas source terms generated from the degradation of plastics and rubbers, corrosion of steel drums, and radiolysis of water. More nonlinearities are introduced by the interbed fracture model and salt creep closure model (Day, 2012). In this section, all simulation results at 10,000 years for 20 selected grid cells in important regions are verified and confirmed against each other within 0.5% of relative error. Convergence tolerances and all the other parameters in the simulation inputs are the same in all simulations. We next report results comparing default PFLOTRAN solvers against the tailored preconditioner and the new nonlinear solver.

### Traditional vs. Tailored Linear Solvers and Preconditioners

We applied two different methods to decouple the pressure matrix from the global matrix: Quasi-IMPES and ABF. The nonlinear solver used in this section is the traditional Newton-Raphson (Newton). The linear solvers used are BiCGSTAB for ILU preconditioner and FGMRES for CPR-Quasi-IMPES (FCQ) and CPR-ABF (FCA) preconditioner. For the Easy Case, Table 2-17 shows the wall-clock computation time using 2 compute nodes or 32 cores on SNL's Skybridge HPC cluster that hosts Intel Xeon Processor E5-2670 2.60 GHz, 20M Cache. The traditional BCGS takes 42 hours to complete the 10,000-year simulation of the undisturbed scenario (the Easy Case) while the tailored FCQ takes 12 hours and FCA takes 1.24 hours, an impressive 35 times improvement. Table 2-17 also demonstrates that BCGS had 28 million linear iterations and 76 thousand nonlinear iterations while FCA had 125 times fewer linear iterations and 5 times fewer nonlinear iterations. When comparing the number of iterations, it is important to note that the two-stage CPR preconditioner already includes ILU step which means each iteration for FCA is more computationally demanding than BCGS; hence, the larger difference in the number of linear iterations than the overall computation times. FCQ is no longer mentioned in the following results as FCA performance is much better than FCQ. FCQ did not perform much better than BCGS-ILU.

Table 2-17 The overall computation time with Newton, Easy case, 32 cores.

| | **BCGS-ILU** | **FCQ** | **FCA** |
|---|---|---|---|
| **Computation Time [hours]** | 42 | 12.5 | 1.24 |
| **Time Steps** | 47057 | 10985 | 4633 |
| **Nonlinear Iterations** | 76874 | 26184 | 15468 |
| **Linear Iterations** | 28443067 | 5162562 | 227268 |
| **Time Step Cuts** | | | |
| **Linear Solver Fail** | 14741 | 2509 | 33 |
| **Max Nonlinear Iteration** | 284 | 554 | 801 |
| **Intentional Time Step Cut** | 84 | 294 | 588 |

Table 2-18 shows the performance of BCGS and FCA Mid Case, which is more difficult to solve than the Easy Case. It required twice as many cores (64 cores) to complete the simulation in a similar computation time. The traditional solvers took 35.7 hours and FCA solver and preconditioner combination took 1.2 hours. Again, this is nearly a 30 times improvement in computation time.

The Hard Case was only completed by FCA and it took 41 hours with 32 cores to complete compared to 1.2 hours of the Easy Case with 32 cores. Table 2-19 demonstrates that this case is a much more difficult simulation to run. The traditional solver did not finish this case in 4 days with 128 cores and there is no valid data point to present in the figure. The Hard Case computation time is reduced further by applying the new nonlinear solver and solution scaling in the later section.

Table 2-18 The overall computation time with Newton, Mid case, 64 cores.

| | **BCGS-ILU** | **FCA** |
|---|---|---|
| **Computation Time [hours]** | 35.7 | 1.2 |
| **Time Steps** | 35015 | 5735 |
| **Nonlinear Iterations** | 72837 | 22608 |
| **Linear Iterations** | 51864686 | 487028 |

Table 2-19 The overall computation time with Newton, Hard case, 32 cores.

| | **BCGS-ILU** | **FCA** |
|---|---|---|
| **Computation Time [hours]** | Did not finish | 41.1 |
| **Time Steps** | N/A | 36649 |
| **Nonlinear Iterations** | N/A | 119362 |
| **Linear Iterations** | N/A | 17118859 |

**Newton vs NTRDC Nonlinear Solver**

In the previous section, we demonstrated how the tailored preconditioner-linear solver combinations can improve the overall computation performance while using the same Newton solver. Here, we compare the performance difference between the new nonlinear solver NTRDC to Newton using the same traditional linear solver BCGS-ILU. NTRDC-AutoScale is used for the comparison because it is the most robust way to utilize the NTRDC algorithm.

Table 2-20 The overall computation time with BCGS-ILU, Mid case, 64 cores.

| | **Newton** | **NTRDC-AS** |
|---|---|---|
| **Computation Time [hours]** | 35.7 | 4.96 |
| **Time Steps** | 35015 | 26195 |
| **Nonlinear Iterations** | 72837 | 102968 |
| **Linear Iterations** | 51864686 | 3709002 |
| **Time Step Cuts** | | |
| **Linear Solver Fail** | 10102 | 0 |
| **Max Nonlinear Iteration** | 900 | 4505 |
| **Intentional Time Step Cut** | 178 | 55 |

Table 2-20 shows that the nonlinear solver improvement alone can have a significant impact on the performance of the simulation. The Mid Case with 64 cores shows that NTRDC was about 7 times faster than Newton, but it had more nonlinear iterations than Newton.

The linear solver takes 31%, the residual calculation takes 18% and Jacobian computation takes 51% of the computation time for the Newton solver. NTRDC has the computational effort distribution of 23%, 21%, and 56% for the linear solver, residual calculation, and Jacobian calculation, respectively. The changes in effort ratio for NTRDC number of linear iterations for linear solve has reduced and the inner iteration residual calculation for nonlinear solve has increased. Also, the Jacobian computational effort ratio is increased because the linear solver computational effort has reduced significantly.

### Effects of Scaling Solution Vector

This analysis shows the importance of scaling down the solution update vector for pressure in the range of saturation. We hypothesized that if the solution update vector is not properly scaled and normalized between two unknown variables, pressure, and saturation, then the pressure dominates the optimization criterion which might result in a low-accuracy solution for saturation. Thus, if the two unknown quantities are scaled properly, it should be possible to minimize both saturation and pressure using the NTRDC algorithm and enhance its computational performance (Table 2-21).

Table 2-21 The overall computation time with FGMRES-ABF, Hard case, 32 cores.

| | **Newton** | **NTRDC** | **NTRDC-AS** |
|---|---|---|---|
| **Computation Time [hours]** | 41.1 | 44.7 | 14.3 |
| **Time Steps** | 36649 | 37772 | 26433 |
| **Nonlinear Iterations** | 119362 | 106937 | 118043 |
| **Linear Iterations** | 17118859 | 16499512 | 3277347 |

The impact of nonlinear solver scaling is maximized for the Hard Case which has the most nonlinearity in the simulation. Table 2-21 shows that NTRDC-AS has about 3 times the overall computation time reduction compared to NTRDC and Newton. Not only that, NTRDC without scaling optimizes for pressure more than saturation; therefore, it degrades in performance compared to Newton in this case. The next section has the best improvements seen with combinations of NTRDC-AS and FCA.

### Largest Improvements with Tailored Linear and Nonlinear Solvers

Table 2-22 shows the two best cases with the best improvements in computation time compared with the traditional solvers. Unfortunately, it was not possible to assess the Hard Case, because the simulation did not complete after 2 days with 64 cores or 128 cores for the traditional solver. The combinations of CPR-ABF preconditioner for GMRES and NTRDC nonlinear solver resulted in the shortest computation time with 32 cores for the Easy Case: 42 hours for the traditional solver, BCGS and Newton, reduced to 0.9 hours for the efficient solvers, which is 47 times faster. Interestingly, GMRES performed slightly better than FGMRES (approximately 5%). The number of linear iterations decreased from 28,443,067 to 107,950 approximately 263 times, and the number of nonlinear iterations decreased from 76,874 to 9,787. Recall that each iteration of the traditional linear solve and nonlinear iterations are computationally much cheaper than the efficient solvers, but the efficient solvers' robustness and accuracy on each iteration enable them to outperform overall. The Mid Case required more computational resources for the traditional solver, so the comparison was made using 64 cores; in this case, the efficient solvers of FGMRES and NTRDC outperformed the traditional solvers by 40 times with computation time reduction from 35.7 hours to 0.9 hours. The number of linear iterations dropped from 51,864,686 to 348,019 approximately 149 times, and the number of nonlinear iterations dropped from 72,837 to 12,647.

Table 2-22 The best improvement overall computation time.

| **Easy Case, 32 cores** | **Default** | **GMRES-CPR-ABF-NTRDC-AS** |
|---|---|---|
| **Computation Time [hours]** | 42.0 | 0.935 |
| **Time Steps** | 47057 | 3075 |
| **Nonlinear Iterations** | 76874 | 9787 |
| **Linear Iterations** | 28443067 | 107950 |

| **Mid Case, 64 cores** | **Default** | **FGMRES-CPR-ABF-NTRDC-AS** |
|---|---|---|
| **Computation Time [hours]** | 35.7 | 0.924 |
| **Time Steps** | 35015 | 3616 |
| **Nonlinear Iterations** | 72837 | 12647 |
| **Linear Iterations** | 51864686 | 348019 |

#### *2.3.4.2 Non-isothermal Miscible Two-phase Flow Performance Improvements*

**Description of Non-isothermal Miscible Case Study**

One interesting reference case from GDSA is the UZ alluvium reference case which assumes a hypothetical mined repository in unsaturated alluvium located approximately 255 m below the land surface, accessed by a ramp, and containing 70,000 metric tons heavy metal of commercial spent nuclear fuel (Sevougian et al., 2017; Sevougian et al., 2019a). It also assumes a small amount of precipitation, a regional head gradient, and a variably saturated model domain to a depth of around 500 m with water saturated media below. The initial condition of the simulation domain starts with unsaturated two-phase condition above 500 m and fully saturated liquid state below 500 m. The heat from the spent nuclear fuel waste packages can generate peak temperatures ranging from 150 °C to 350 °C to potentially boil off water to vapor even at elevated pressures. Since this is a hypothetical repository, there is more freedom in choosing characteristics of the repository such as diameter of the drift where waste packages reside, thermal conductivity of back-fill material, host rock characteristics, waste package spacing, and drift spacing. Figure 2-30 illustrates the concept of the full-scale repository.

The model is generated by a CUBIT (Blacker et al., 1994) refinement algorithm where the mesh generator refines grid cells by a third every time the algorithm is applied. The mesh was generated from the far-field inward.

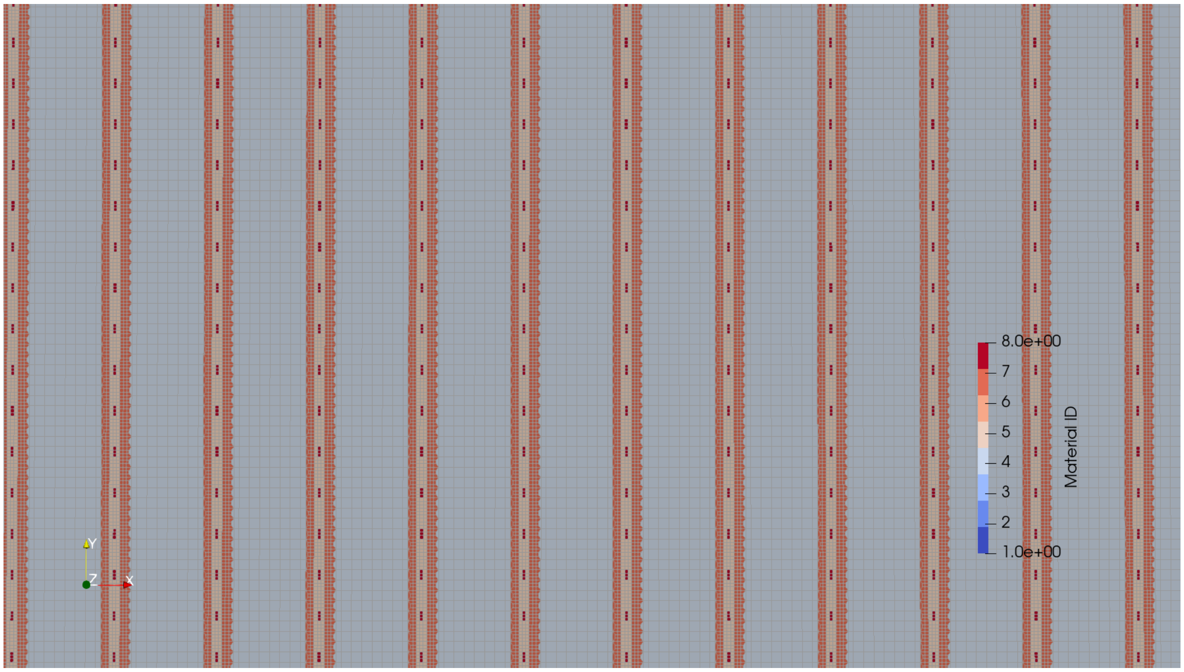

Figure 2-30 Top view of the field-scale hypothetical waste repository zoomed into the waste area. The dark red (8) is the waste packages, the light orange (5) is the drifts back-filled with engineered barriers, the dark orange (7) is the damaged rock zone, and the white (4) is the host rock of the repository (Sevougian et al., 2019).

### Heat Generating Waste Power Levels

There are three sets of power levels of the nuclear waste packages. Twelve pressurized water reactor (PWR) assembly packages, 24 PWR packages and 37 PWR packages. The higher the number assemblies in the waste packages, they generate more power and cause higher peak temperatures for the waste repository simulations. The initial power output is the highest at the initial condition and the radionuclides in the waste packages decay away, generating less power over very long periods of time. Figure 2-31 shows that even at 10,000 years all three waste packages generate power.

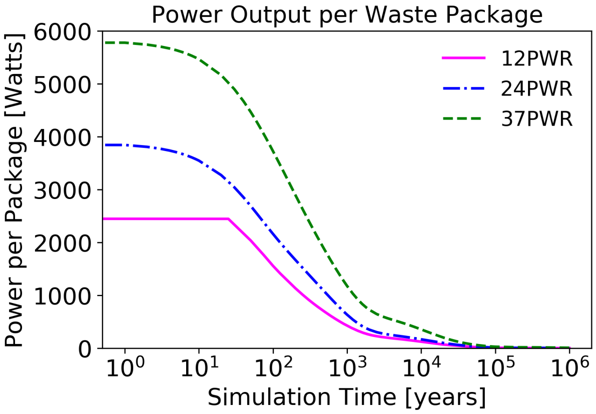

Figure 2-31 The plot shows power generation per nuclear packages from radionuclides decay heat over time. There are three types of waste packages in the numerical experiments. Each waste packages contain number of pressurized water reactor fuel assemblies. The waste packages are hotter and generate power longer with more fuel assemblies.

### Grid Refinement Levels

There are three different discretizations for the model: $6.4x10^4$, $1.043x10^5$, and $2.4x10^6$ grid cells, namely the homogeneous, coarsened, and fully-refined model. The top of Figure 2-32 shows all three discretizations in one image for better comparison. Originally, the fully-refined model was created to run with PFLOTRAN; however, the Newton solver was too slow to simulate for 1 million years which is the regulatory goal for commercial spent fuel nuclear waste repositories. The Newton solver was at merely 50 years of simulation using 1024 cores for 48 hours on SNL's Skybridge HPC cluster that hosts Intel Xeon Processor E5-2670 2.60 GHz, 20M Cache. The domain was coarsened gradually until the simulation would run in a reasonable amount of time to debug the issue with the 12-PWR power source. Larger 24-PWR and 37-PWR power sources could only finish in the homogeneous models. These coarsened and fully refined models were only able to complete after the NTRDC development and implementation was completed. The coarser grid is not only more manageable for the linear solver with fewer grid cells, but the nonlinearity is relaxed with lower peak temperature compared to the fully-refined model and reduces the number of state changes and reaching the kink of the van Genuchten curve near residual gas saturation.

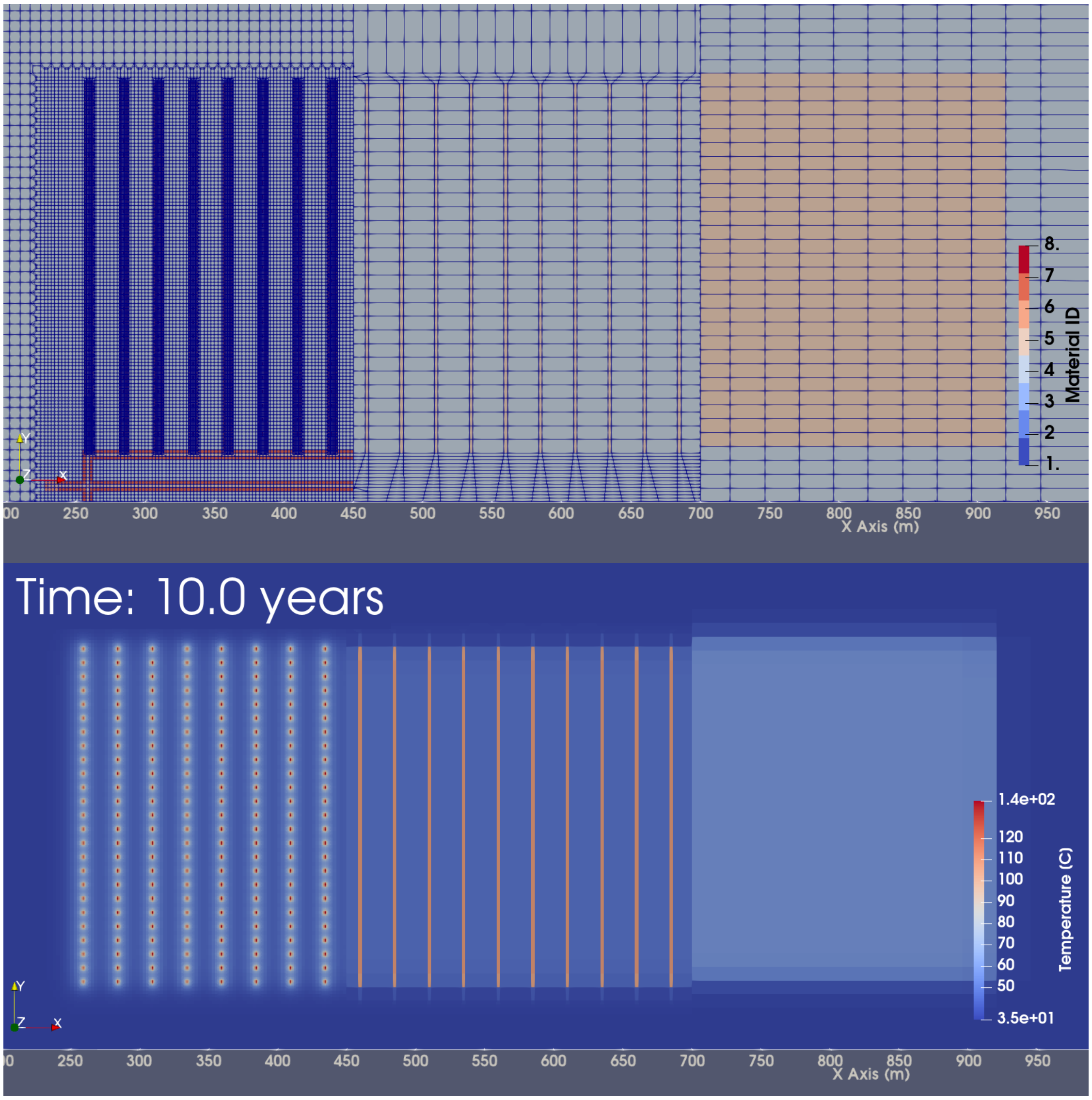

Figure 2-32 Fully-refined model (top-left, 7.2x$10^6$ unknowns), Coarsened model (top-middle, 3.13x$10^5$ unknowns), and homogeneous model (top-right, 1.9x$10^5$ unknowns). In the coarsened model, the drifts and the damaged rock zone are lumped with waste packages as a larger volume, therefore, decreasing the power density and the peak temperatures (bottom). The homogeneous model lumps further having the entire region as the backfill material.

### Non-Boiling Simulations

The homogeneous domain with 24-PWR power source reaches the domain peak temperature of 80 degrees C at an atmospheric pressure and water does not boil into the gas phase state below the liquid residual saturation of the van Genuchten curve where the discontinuity exists. In this case, all three solvers, Newton (NT), Newton trust-region (NTR), and Newton trust-region dogleg Cauchy (NTRDC) performed consistently (Table 2-23). The Newton solver surprisingly has the least number of time step cuts and nonlinear iterations, but some of the linear systems of equations are ill-conditioned causing more linear iterations and linear solver failures impacting the overall computation time.

Table 2-23 The overall computation time: homogeneous, 24 PWR, non-boiling, 190k unknowns (2 cores).

| | NT | NTR | NTRDC |
|---|---|---|---|
| **Computation Time [mins]** | 28.39 | 27.1 | 31.0 |
| **Time Steps** | 350 | 382 | 418 |
| **Nonlinear Iterations** | 704 | 749 | 1032 |
| **Linear Iterations** | 116896 | 96961 | 98202 |

### Boiling Simulations

The homogeneous domain with a 37 PWR power source reaches the domain peak temperature of 120 degrees C at an atmospheric pressure and does boil into the gas phase state for many grid cells reaching the kink at the liquid residual saturation of the van Genuchten curve. Table 2-24 clearly demonstrates that the trust-region variant nonlinear solvers perform better at resolving the discontinuity of the van Genuchten curves when reaching near the boiling point or below the residual liquid saturation. The Newton solver takes about 2 times longer, 6.6 hours, to complete the simulation compared to 2.6 to 3.2 hours of the trust-region variants. The number of nonphysical nonlinear solutions dominated the number as the reasons for Newton time step cuts. The trust-region variants were able to detect the difficult nonlinearities early in the time steps to prevent further calculations and cut the time steps early. In contrast, the Newton solver has about 4 times more nonlinear iterations (about 120,000 compared to 30,000) leading to more unnecessary linear iterations which were later discarded by the nonphysical solutions even though all three methods have similar number of the total time steps between 11,000 to 13,500.

Table 2-24 The overall computation time: homogeneous, 37 PWR, boiling, 190k unknowns (16 cores).

| | NT | NTR | NTRDC |
|---|---|---|---|
| **Computation Time [hours]** | 6.64 | 3.06 | 2.76 |
| **Time Steps** | 12157 | 12736 | 11342 |
| **Nonlinear Iterations** | 125959 | 32970 | 29641 |
| **Linear Iterations** | 4058709 | 1844465 | 1668355 |

### Boiling Simulations with extended van Genuchten curve

Sun et al. (2010) discusses how typical van Genuchten curve parameters are not calibrated for strongly heat-driven conditions like our numerical experiment simulations where the conditions reach for boiling and rock dryout occurs. As previously discussed in Section 2.3.1.2, various unsaturated extensions have been proposed to replace the abrupt corner inherent in the flat capped maximum capillary pressure (FCPC) model. Conventional Newton solvers can be non-convergent at corners. The various exponential and linear models rectify this by requiring a smooth derivative, stabilizing Newton's method. As shown in Table 2-25, the ECPC, ENOC, and LCPC unsaturated extensions allow the NT solver to complete the simulation within 35 minutes whereas the original FCPC extension with a corner did not converge within 48 hours on 16 cores.

Table 2-25 The extended VG, coarsened, 24-PWR, 313k unknowns (16 cores).

| NT | FCPC (original) | ECPC | ENOC | LCPC |
|---|---|---|---|---|
| **Computation Time [mins]** | Did not finish | 31.8 | 34.1 | 33.8 |
| **Time Steps** | N/A | 1469 | 1535 | 1502 |
| **Nonlinear Iterations** | N/A | 3427 | 3736 | 3832 |
| **Linear Iterations** | N/A | 494707 | 526974 | 505648 |

The Newton Trust Region Dogleg Cauchy (NTRDC) solver can complete the simulation with the original FCPC, as well as with the exponential or linear extensions. However, as shown in Table 2-26, there is still a considerable performance improvement when utilizing smooth unsaturated capillary pressure models. That is, the original extension completed the simulations in 551 minutes whereas all other options complete in under 24 minutes. On average, the computation time for models experiencing dryout was observed to be reduced by a factor of approximately 25.

Table 2-26 The extended VG, coarsened, 24-PWR, 313k unknowns (16 cores).

| NTRDC | FCPC (original) | ECPC | ENOC | LCPC |
|---|---|---|---|---|
| **Computation Time [mins]** | 551 | 18.3 | 20.1 | 19.4 |
| **Time Steps** | 10405 | 1503 | 1589 | 1539 |
| **Nonlinear Iterations** | 77052 | 1662 | 1720 | 1830 |
| **Linear Iterations** | 1330198 | 271559 | 284439 | 280203 |

When comparing the NT and NTRDC methods with equivalent unsaturated extensions, the NTRDC outperforms the NT solver in all cases tested. In the cases tested here, the NTRDC method reduced computation time of equivalent smooth capillary pressure options by 40% compared to equivalent NT simulations. Consequently, NTRDC is complementary to the capillary pressure smoothing. The reduction in computation time occurs as fewer nonlinear and linear iterations are necessary per timestep for NTRDC. Thus, for both reasons of stability and performance, the NTRDC method developed and describes has advantages over the NT method for simulations approaching dryout.

### Fully Refined Simulations

The fully-refined 12 PWR model has approximately $7.2 \times 10^6$ degrees of freedom (unknowns) or $2.4 \times 10^6$ grid cells in the domain. The 100,000-year simulation experiences $2.2 \times 10^6$ phase state changes in grid cells with NTRDC solver starting the simulation from the room temperature to peak temperature of 140 degrees C. The grid cells can change states in between liquid phase and two-phase state or two-phase and gas phase state. The phase state changes are non-smooth phenomena because of primary variable switching and the Newton algorithm fails to resolve the nonlinearity even with the extended van Genuchten curves. The Newton solver reached a simulation time of 237.4 years after the 96 hours of the computation time with 144 cores. The simulation had already reached 442k nonlinear iterations and $4.7 \times 10^6$ linear iterations. On the other hand, Table 2-27 shows that NTR and NTRDC completes the simulation just under 23 hours with 5,000 nonlinear iterations (does not include inner iterations) and around $6 \times 10^6$ linear iterations. They had no problem resolving the difficult nonlinearity in the beginning of the simulation where the waste packages heat up to the peak temperature and cools down in the first 1,000 years of the simulation. The Newton solver had nearly 40,000 time step cuts in the first 96 hours of the simulation with 144 cores whereas NTR and NTRDC only had about 1,500 time step cuts throughout the whole simulation. This test case perfectly demonstrated the superiority of the trust-region methods over the Newton-Raphson method, and the behavior of the solvers were the same for fully-refined 24-PWR and 37-PWR cases where the peak temperatures are even higher.

Table 2-27 The overall computation time: fully-refined, 12-PWR, 7.2x$10^6$ unknowns (144 cores).

| | **NT** | **NTR** | **NTRDC** |
|---|---|---|---|
| **Computation Time [hours]** | Did not Finish | 22.74 | 19.99 |
| **Time Steps** | N/A | 3975 | 4491 |
| **Nonlinear Iterations** | N/A | 5147 | 5158 |
| **Linear Iterations** | N/A | 6412946 | 5795461 |

### 2.3.4.3 *Scalability Experiments*

**True Strong Scalability of CPR and TR solvers**

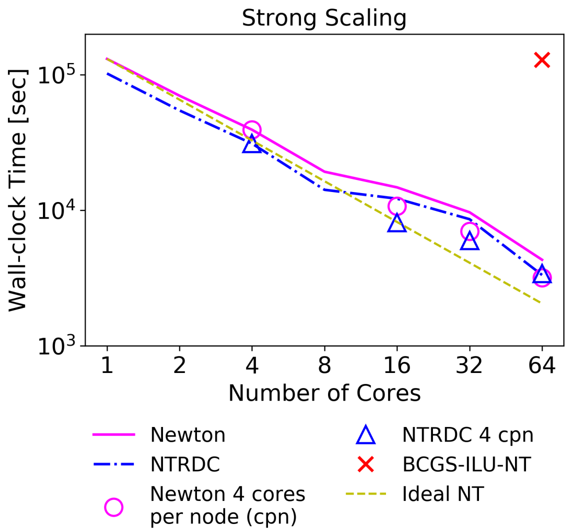

Figure 2-33 Wall-clock time in seconds is plotted against the number of cores involved in the simulation which represents strong scaling of Newton (NT) and NTRDC with FGMRES-CPR-ABF solver-preconditioner combination. NTRDC shows as good of scalability as Newton and follows the trend of ideal strong scaling plot, and it follows the ideal line even closer when node packing defect is reduced.

The Mid Case was run on a different numbers of cores and cores per node to demonstrate the strong scalability of the newly implemented algorithms: FCA preconditioner-linear solver combination with Newton and NTRDC. The strong scaling of FCA-Newton and FCA-NTRDC follows the trend of ideal strong scaling in Figure 2-33. Also, note that the traditional method (BCGS-Newton) is shown with a single available data point in the figure with 64 cores. The trend of fully-packed nodes (16, 32, and 64 cores) is still close and parallel to the ideal trend line. There are four data points with the hollow circle and hollow triangle that represents reduced node packing effect (inefficiency) with 4 cores per node utilization and you can see that it is much closer to the ideal for strong scalability.

### Relative Strong Scalability

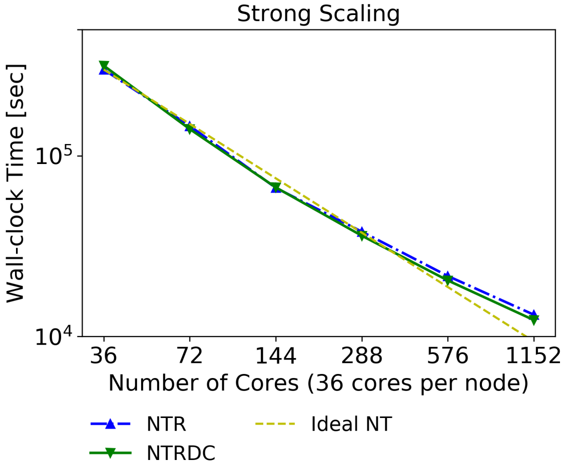

Figure 2-34 The plot shows the relative strong scaling where the base case is running 1 node with 36 cores, a fully packed node. The strong scalability is right on top of the ideal line.

The relative strong scalability of the simulator in general is phenomenal and the same applies for the newly developed NTR and NTRDC solvers. The test was done on the fully-refined domain. The relative strong scalability was tested using one full node as the base-line case and eliminating the node packing effect from the scalability test. The trend follows the ideal line extremely closely except for the last point. Running this domain on 1,152 cores is not efficient because not enough unknowns would be distributed to each processor to maximize each processor efficiency; i.e., this is too small of a problem to solve per processor.

# 2.4 Integration and Outreach

## 2.4.1 SNL/LBNL Integration

### *2.4.1.1 Reduced Order Geomechanics*

Simulating the fully coupled thermal, hydrologic, chemical, and mechanical behaviors of a repository system can be challenging numerically due to large contrasts in timescales associated with each process as well as large contrasts in their associated representative length scales. One way to preserve computational efficiency while maintaining high fidelity modeling is to fully model thermal, hydrologic, and chemical behavior of the repository system while using reduced order models to approximate the system's geomechanical behavior. To this end, the PFLOTRAN Development team worked with scientists at Lawrence Berkeley National Laboratory (LBNL) this year to develop reduced order modeling techniques for approximating geomechanical behavior of repository tunnels during the liquid re-saturation phase of a repository performance period.

Through this collaboration, LBNL performed a series of high-resolution, single-tunnel models by coupling multiphase, non-isothermal flow in TOUGH with geomechanics in FLAC. In these models, a repository was set within a saturated shale host rock bentonite buffer was shown to swell in a nearly isotropic manner as water imbibed from the host rock into the buffer (Sasaki et al., 2021). This swelling stress exerted stress on the surrounding disturbed rock zone (DRZ), which was initialized as a fractured version of the host rock material to incorporate host rock damage due to drilling. When the bentonite exerted stress on the DRZ, fractures in the DRZ responded by closing. Permeability and porosity in the DRZ responded accordingly by decreasing. Since this process was controlled by the transient liquid re-saturation behavior, a reduced order model was developed in PFLOTRAN to relate changes in liquid saturation to changes in DRZ porosity and permeability.

For this reduced order model, PFLOTRAN was first developed to read in swelling properties of the bentonite and compute isotropic swelling stress as a function of liquid saturation as follows:

$$\Delta\sigma_{swell} = 3K\Delta S_l \beta_{sw} \qquad \text{Equation 2.4-1}$$

where $K$ is the bulk modulus of the bentonite, $\beta_{sw}$ is a dimensionless moisture swelling coefficient, and $\Delta\sigma_{swell}$ is the change in swelling stress due to a change in liquid saturation, $\Delta S_l$. This change in swelling stress from the buffer was assumed equal to the change in effective stress exerted on the DRZ:

$$\Delta\sigma_{eff} = \Delta\sigma_{swell} \qquad \text{Equation 2.4-2}$$

where $\Delta\sigma_{eff}$ is the change in effective stress felt by the DRZ.

The change in permeability due to effective stress on a fractured rock depends heavily on host rock lithology and the nature of the fractures. For this study, fractures are generally assumed to run tangentially to the tunnel (perpendicular to a radial swelling stress). Under this assumption, fractures close under an applied stress and both permeability and porosity decrease with increasing swelling stress. Three different permeability models were implemented in PFLOTRAN to describe this process: an exponential function, a cubic function, and a Two-Part Hooke's Law model. A sensitivity analysis was performed over a range of model parameterization for a shale host rock (Figure 2-35) and is the subject of a publication under review. More information on this modeling effort can be found in Chang et al (2021) and LaForce et al. (2020).

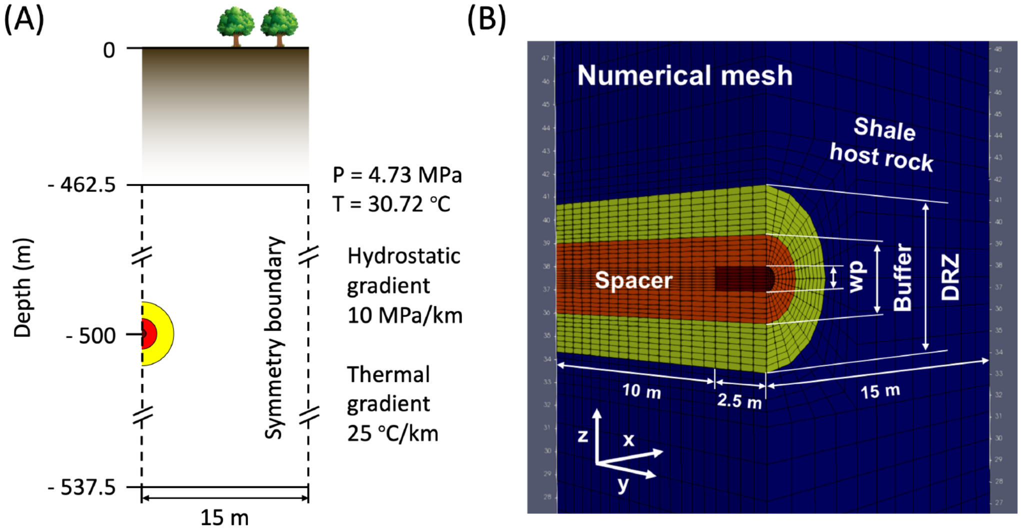

Figure 2-35 A) Conceptual model of a quarter-symmetry domain and B) numerical mesh used to study near-field phenomena in a shale-hosted repository

#### *2.4.1.2 Surrogate Geochemistry Modeling*

On a parallel track, the PFLOTRAN Development team also organized a series of discussions on implementing surrogate geochemistry models into PFLOTRAN as a fast alternative to modeling complex geochemistry in addition to flow, heat transport, and radionuclide decay/ingrowth/sorption on large-scale PA runs. Through this effort, LBNL is performing a series of reactive transport models using TOUGH-REACT with full geochemistry to model the evolution of sorption partitioning coefficients ($K_d$), as a function of a reduced set of geochemical species. These 1D, high resolution, stylized models are formulated to approximate the nearfield of a repository tunnel and include a waste form, buffer, DRZ, and host rock. From these models, $K_d$'s will be extracted as a function of a set of parameters that are solved for during PA-scale PFLOTRAN simulations.

### 2.4.2 SNL/ORNL Neutronics Surrogate Modeling

In support of the DPC Criticality Consequence Assessment work package, PFLOTRAN developers undertook a collaboration with Oak Ridge National Laboratory to integrate neutronics surrogate models into PFLOTRAN. This integration took the form of a criticality sub-module attached to the waste form process model whereby criticality information could either be read in from external datasets or input as parameters to mechanistic surrogate models describing criteria for switching a criticality on or off. PFLOTRAN development work in support of this project is detailed in Section 2.2.7. Additionally, to support development of the reduced order surrogate models, a study was performed to compute transient and steady-state temperatures at the waste package surface as a function of a steady-state critical power level.

#### *2.4.2.1 Waste Package Surface Temperature as a Function of Critical Power Level*

In this study, the near-field model domain described in Figure 2-35 was used to approximate the center-most waste package in the center-most repository tunnel, which would presumably experience the most significant thermal loading in a worst-case scenario where all waste packages go critical. In this hypothetical, conservative scenario, it was assumed that a criticality event could be characterized by an average steady-state power level that would constitute a constant heat source over the course of the criticality event. Given the initial and boundary conditions of the simulation, this constant heat source would presumably initiate a period of transient temperature evolution at the waste package canister surface until ultimately a steady state is reached. This canister surface temperature is an important constraint to neutronics models, which model the change in waste form inventory resulting from fission and decay during the critical event. Therefore, waste package canister surface temperature was identified as a linkage point between PFLOTRAN and ORNL neutronics codes. With canister surface temperatures as a function of time and critical power level, ORNL neutronics codes can generate surrogate models for inventory evolution during a criticality. Figure 2-36 illustrates the evolution of temperature as a function of time for 5 different steady-state critical power outputs: power outputs below 4 kW reached a steady state, while power outputs above 4 kW raised temperatures beyond the equation of state boundaries in PFLOTRAN. This means that all the water boiled away and temperature rose above water’s boiling point; this process would remove liquid water entirely from the waste package and shut off the criticality event due to a lack of moderator, so only scenarios where steady-state temperature profiles were achieved were considered feasible model scenarios.

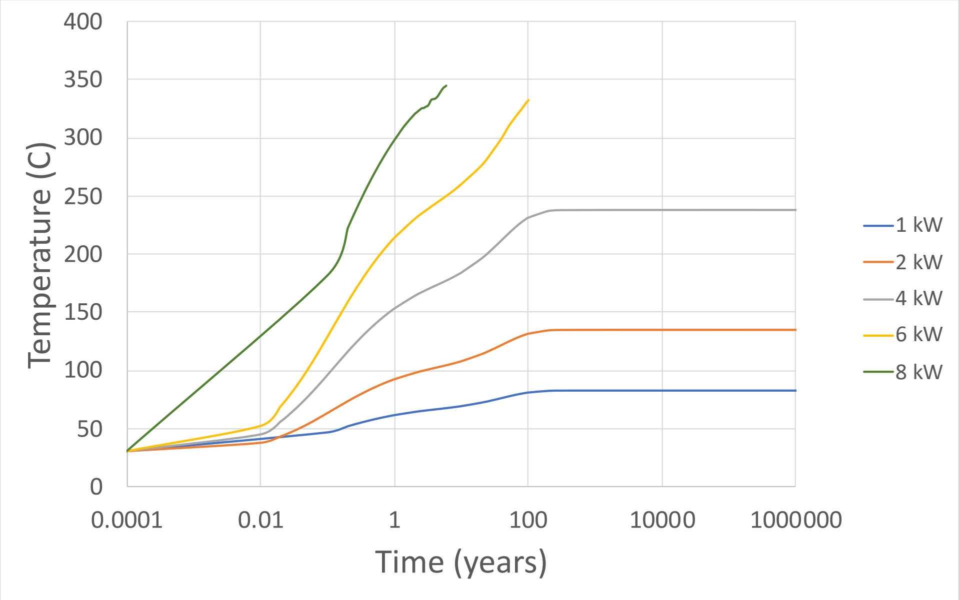

Figure 2-36 Temperature versus time at the waste package boundary for various steady-state critical power levels

### 2.4.3 Short Course

This year, community outreach took the form of a fully virtual PFLOTRAN short course, which took the form of an 8-week (2 hr/wk) course and began on June 7, 2021. The course had 32 participants across 4 national labs and 6 countries. PFLOTRAN developers at Sandia National Laboratories and Pacific Northwest National Laboratory hosted the short course and covered the basics of flow and transport simulations as well as advanced concepts relating to multicontinuum modeling of radionuclide transport and subsurface radioactive waste repository simulations.

### 2.4.4 PFLOTRAN International User Base

PFLOTRAN's open-source licensing and accessible distribution facilitate collaboration amongst a broader U.S. and international community. This broad user community enhances the development of PFLOTRAN by sharing conceptual models, incorporating novel physicochemical algorithms, optimizing code performance, debugging problematic issues, and generating grass-roots publicity, all of which benefit DOE in return.

The PFLOTRAN website at www.pflotran.org directs interested parties to the online documentation and the Bitbucket repository (including source code and documentation build status and code coverage). Developer and user mailing lists are managed through Google Groups.

Estimating the size and extent of the PFLOTRAN user community is relatively difficult due to the inability to track downloads on Bitbucket. However, through Google Analytics, the hits on the PFLOTRAN website are tracked which provides a qualitative estimate (Figure 2-37) and demonstrates that the PFLOTRAN user base is multi-national. The top ten countries with the most users are as follows (from most to fewest users): United States, China, Germany, Japan, United Kingdom, Canada, India, Norway, South Korea, and Italy.

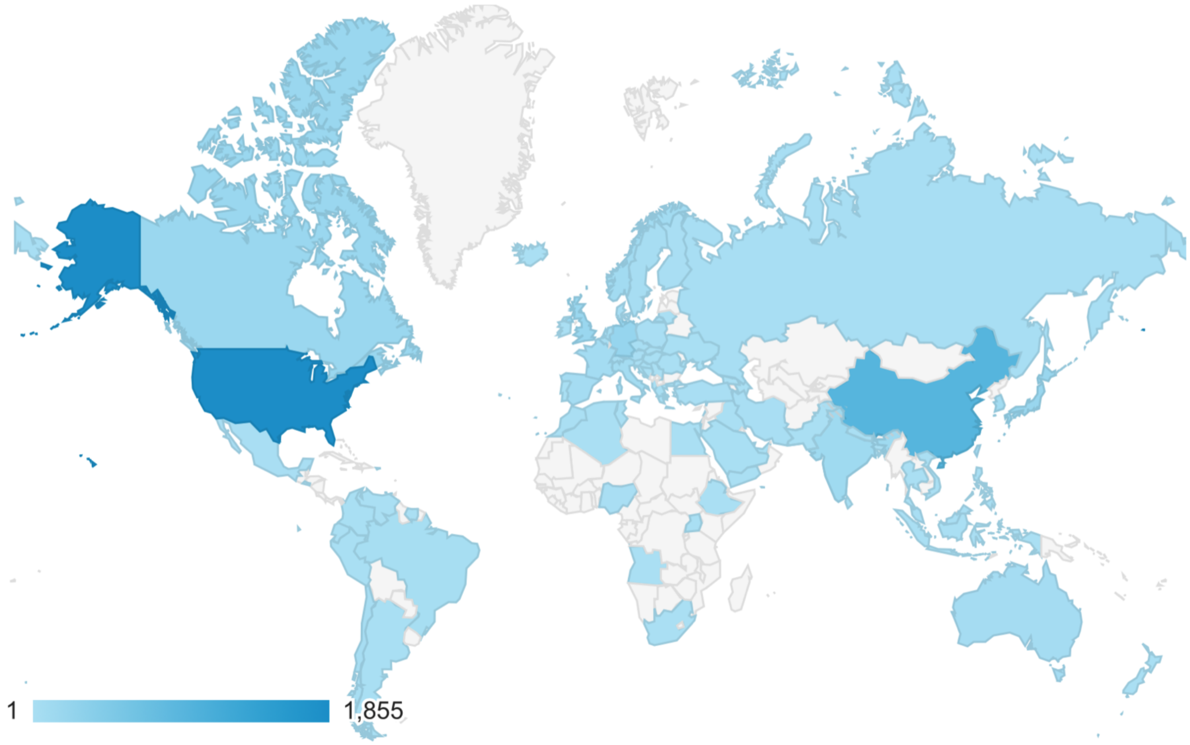

Figure 2-37 User count on the PFLOTRAN website around the world between June 12, 2020 and June 12, 2021, colored by country

### 2.4.5 Open Source

Open-source software licensing governs the free distribution of source code and/or binaries among a group of software developers and users. PFLOTRAN utilizes the GNU LGPL (lesser general public license) which states that the code may be distributed and modified as desired, but any changes to the original source code must be free and publicly available. On the other hand, LGPL allows anyone to link a proprietary third-party library to the code or develop a graphical user interface on top of the code for profit. Further details are provided in Mariner et al. (2019, Section 2.3.4.1).

There are many benefits to open-source collaboration, especially when taxpayer funds support much of the code development. First, it encourages collaboration among a diverse team of developers. This collaboration pushes the code to the global public who can help test and debug the code while providing feedback regarding user interaction. Open source provides transparency that exposes implementation details that are often critical for scientific reproducibility and quality assurance. These details are often omitted from user documentation, journal publications and reports. From a financial standpoint, open source allows developers to pool funds across a diverse set of projects funded in academia, government laboratories or the private sector. In addition, funding that would be spent on licensing fees can be redirected towards development.

PFLOTRAN development is currently supported by multiple developer groups from around the world. DOE provides the most support for PFLOTRAN development through its national laboratories funded by the DOE Offices of Environmental Management, Nuclear Energy, and Science. In addition, private sector companies such as OpenGoSim (opengosim.com) have invested development in support of oil and gas and carbon sequestration efforts, while Amphos21 has developed PFLOTRAN capability for nuclear waste disposal (e.g., de Vries et al, 2013; Iraola et al 2019).

# 3. SUMMARY

The PFLOTRAN Development work package made major strides during FY21, but challenges remain. Improvements were made in three general areas: software infrastructure, process modeling, and code performance. The PFLOTRAN development team has adopted an Agile software development framework using the Jira task manager, which has added enhanced transparency and traceability to the code development process. Process modeling improvements included refinement of the multi-continuum transport mode for application to the international DECOVALEX project, advancements in thermal modeling capability through thermal conductivity function flexibility and anisotropy, and improvements to in-package criticality modeling. Significant performance improvements were achieved by implementing characteristic curve smoothing as well as by developing new linear and nonlinear solver combinations with specific attention to multiphase simulations. Several outstanding challenges remain regarding the topics covered in this report. These challenges include (but are not limited to): integration of the multi-continuum transport mode with the UFD Decay process model for broad applicability of this transport mode to GDSA applications, transport functionality when a liquid phase fully evaporates or boils, more accurate parameterization of geomechanical behaviors, more advanced modeling of $K_D$ evolution, and integration of nonlinear solver capabilities into the release versions of PFLOTRAN and PETSc.

# 4. REFERENCES

Balay, S., J. Brown, K. Buschelman, V. Eijkhout, W. D. Gropp, D. Kaushik, M. G. Knepley, L. Curfman McInnes, B. F. Smith and H. Zhang (2013). PETSc Users Manual. Argonne, Illinois, Argonne National Laboratory.

Bank R. E. , T. F. Chan, W. Coughran, R. K. Smith, The alternate-block-factorization procedure for systems of partial differential equations, BITNumerical Mathematics 29 (4) (1989) 938–954.

Bear, J. (1972). Dynamics of fluids in porous media–American Elsevier pub. *Comp., inc. New York, 764p*.

Birch, A. F., & Clark, H. (1940). The thermal conductivity of rocks and its dependence upon temperature and composition. *American Journal of Science*, *238*(8), 529-558.

Blesch, C. J., Kulacki, F. A., & Christensen, R. N. (1983). *Application of integral methods to prediction of heat transfer from a nuclear waste repository* (No. ONWI-495). Ohio State Univ. Research Foundation, Columbus (USA).

Brooks, R. H., & Corey, A. T. (1964). Hydraulic properties of porous media and their relation to drainage design. *Transactions of the ASAE*, *7*(1), 26-0028.

Burdine, N. (1953). Relative permeability calculations from pore size distribution data. *Journal of Petroleum Technology*, *5*(03), 71-78.

Campbell, G. S., & Shiozawa, S. (1992). Prediction of hydraulic properties of soils using particle-size distribution and bulk density data. *Indirect methods for estimating the hydraulic properties of unsaturated soils*, 317-328.

Chang, K.W., M. Nole, and E. Stein (2021). Reduced-order modeling of near-field THMC coupled processes for nuclear waste repositories in shale. Computers and Geotechnics 138.

Cheng, P., & Hsu, C. T. (1999). The effective stagnant thermal conductivity of porous media with periodic structures. *Journal of Porous Media*, *2*(1).

Chen, X., G. Hammond, C. Murray, M. Rockhold, V. Vermeul and J. Zachara (2013). "Applications of ensemble-based data assimilation techniques for aquifer characterization using tracer data at Hanford 300 area." Water Resources Research 49: 7064-7076.

Chen, X., H. Murakami, M. Hahn, G. E. Hammond, M. L. Rockhold, J. M. Zachara and Y. Rubin (2012). "Three-Dimensional Bayesian Geostatistical Aquifer Characterization at the Hanford 300 Area using Tracer Test Data." Water Resources Research 48.

Cuadros, J., & Linares, J. (1996). Experimental kinetic study of the smectite-to-illite transformation. *Geochimica et Cosmochimica Acta*, *60*(3), 439-453.

Dake, L. P. Fundamentals of reservoir engineering. Elsevier, 1983.

Davidson, G.G., S. Bhatt, M. W. Swinney, E. D. Biondo, J. Salcedo-Perez, K. Banerjee, A. Perry, E. Asano, E. S. Gonzalez, and B. C. Kiedrowski. “Initial Coupled Simulations of a Critical Dual-Purpose Canister in a Saturated Repository.” ORNL/SPR-2020/1723, M3SF-20OR010305016, Oak Ridge National Laboratory, Oak Ridge, TN, September 30, 2020.

Davis, G.B. and C.D. Johnston (1984) Comment on: "Contaminant Transport in Fractured Porous Media: Analytical Solutions for a System of Parallel Fractures" by E. A. Sudicky and E. O. Frind. Water Resources Research, 20 (9), 1321–1322.

de Vries, L. M., J. Molinero, H. Ebrahimi, U. Svensson, P. Lichtner and E. Abarca (2013). Regional Scale HPC Reactive Transport Simulation of Nuclear Spent Fuel Repository in Forsmark, Sweden. Joint 8th

International Conference on Supercomputing in Nuclear Applications (SNA) / 4th Monte Carlo Meeting (MC), Paris, France.

DOE (2012). Used Fuel Disposition Campaign Disposal Research and Development Roadmap. Washington, D.C., U.S. DOE Office of Nuclear Energy, Used Fuel Disposition.

Hillner, E., Franklin, D. G., & Smee, J. D. (2000). Long-term corrosion of Zircaloy before and after irradiation. *Journal of nuclear materials*, *278*(2-3), 334-345.

Frederick, J.M. 2018. PFLOTRAN QA Test Suite. Retrieved July 28, 2020 from qa.pflotran.org .

Freeze, R. A. and J. A. Cherry, 1979. Groundwater, Prentice-Hall, Englewood Cliffs, NJ.

Flynn, D. R., & Watson, T. W. (1969). *MEASUREMENTS OF THE THERMAL CONDUCTIVITY OF SOILS TO HIGH TEMPERATURES. Final Report* (No. SC-CR-69-3059). National Bureau of Standards, Washington, DC.

Gibbs, J. W. (1961). the Scientific Paper of J. Williard Gibbs. *Thermodynamics*, *1*, 55.

Gilman, J. (1986) An efficient finite-difference method for simulating phase segregation in the matrix blocks in double-porosity reservoirs. Soc. Pet. Engs. Reserv. Eng. 1:4, 403–413.

Gray, W. G., & Hassanizadeh, S. M. (1991). Paradoxes and realities in unsaturated flow theory. *Water resources research*, *27*(8), 1847-1854.

Greene, S. R., Medford, J. S., & Macy, S. A. (2013). *Storage and Transport Cask Data for Used Commercial Nuclear Fuel* (No. ATI-TR-13047). DOE-Headquarters.

Hammond, G. E. and P. Lichtner (2010). "Field-scale modeling for the natural attenuation of uranium at the Hanford 300 area using high performance computing." Water Resources Research 46.

Hammond, G. E., P. C. Lichtner and M. L. Rockhold (2011). "Stochastic simulation of uranium migration at the Hanford 300 Area." Journal of Contaminant Hydrology 120-121: 115-128.

Hammond, G. E., P. C. Lichtner, C. Lu and R. T. Mills (2011). PFLOTRAN: Reactive Flow and Transport Code for Use on Laptops to Leadership-Class Supercomputers. Groundwater Reactive Transport Models. F. Zhang, G. T. Yeh and J. Parker, Bentham Science Publishers.

Hammond, G. E., P. C. Lichtner, R. T. Mills and C. Lu (2008). "Toward petascale computing in geosciences: application to the Hanford 300 Area." Journal of Physics Conference Series 125: 12051-12051.

Hammond, G., P. Lichtner and C. Lu (2007). "Subsurface multiphase flow and multicomponent reactive transport modeling using high performance computing." Journal of Physics: Conference Series 78: 1-10.

Huang, W. L., Longo, J. M., & Pevear, D. R. (1993). An experimentally derived kinetic model for smectite-to-illite conversion and its use as a geothermometer. *Clays and Clay Minerals*, *41*(2), 162-177.

Hyman, J. D., S. Karra, N. Makedonska, C. W. Gable, S. L. Painter, and H. S. Viswanathan 2015. "DFNWORKS: A discrete fracture network framework for modeling subsurface flow and transport". Computers & Geosciences, 84, 10-19. doi: 10.1016/j.cageo.2015.08.001

Iraola, A., P. Trinchero, S. Karra and J. Molinero (2019). "Assessing dual continuum method for multicomponent reactive transport." Computers & Geosciences 130: 11-19.

Iraola, A., P. Trinchero, S. Karra and J. Molinero (2019). "Assessing dual continuum method for multicomponent reactive transport." Computers & Geosciences 130: 11-19.

Joshi, N., Ojha, C. S. P., & Sharma, P. K. (2012). A nonequilibrium model for reactive contaminant transport through fractured porous media: Model development and semianalytical solution. *Water Resources Research*, *48*(10).

Karnland, O., & Birgersson, M. (2006). Montmorillonite stability. With special respect to KBS-3 conditions.

Kralchevsky, P. A., Eriksson, J. C., & Ljunggren, S. (1994). Theory of curved interfaces and membranes: mechanical and thermodynamical approaches. *Advances in colloid and interface science*, *48*, 19-59.

Kräutle, S., Hodai, J., Knabner, P. (2020) Robust simulation of mineral precipitation-dissolution problems with variable mineral surface area, accepted for publication in J. Eng. Math., Preprint No. 409 in the Preprint-Reihe Angewandte Mathematik des Departments Mathematik, Friedrich-Alexander-Universität Erlangen-Nürnberg, ISSN 2194-5127, https://www1.am.uni-erlangen.de/research/preprint/pr409.pdf, 1–35.

Kuhlman, K. L., Mills, M. M., Jayne, R. S., Matteo, E. N., Herrick, C. G., Nemer, M., ... & Wang, J. (2020). *FY20 Update on Brine Availability Test in Salt* (No. SAND2020-9034R). Sandia National Lab.(SNL-NM), Albuquerque, NM (United States).

LaCroix S., Y. V. Vassilevski, M. F. Wheeler, Decoupling preconditioners inthe implicit parallel accurate reservoir simulator (ipars), Numerical linearalgebra with applications 8 (8) (2001) 537–549.

LaForce, T., K. W. Chang, F. V. Perry, T. S. Lowry, E. Basurto, R. Jayne, S. Jordan, E. Stein, R. Leone and M. Nole (2020). GDSA Repository Systems Analysis FY 2020 Update Albuquerque, New Mexico, Sandia National Laboratories.

Lichtner, P.C., et al., "PFLOTRAN Documentation, Release 1.1," 2018. [Online]. Available: https://www.pflotran.org/documentation/index.html

Lichtner, P. C. and G. E. Hammond (2012). Quick Reference Guide: PFLOTRAN 2.0 (LA-CC-09-047) Multiphase-Multicomponent-Multiscale Massively Parallel Reactive Transport Code. Los Alamos, New Mexico, Los Alamos National Laboratory.Lu, C. and P. C. Lichtner (2007). "High resolution numerical investigation on the effect of convective instability on long term CO2 storage in saline aquifers." Journal of Physics Conference Series 78: U320-U325.

Lichtner, P.C. (2000) Critique of Dual Continuum Formulations of Multicomponent Reactive Transport in Fractured Porous Media, Ed. Boris Faybishenko, Dynamics of Fluids in Fractured Rock, Geophysical Monograph 122, 281–298.

Lichtner, P.C. and Karra, S. (2014) Modeling multiscale-multiphase-multicomponent reactive flow in porous media: Application to CO2 sequestration and ehanced geothermal energy using PFLOTRAN, In: Computational Models for CO2 Geo-Sequestration & Compressed Air Energy Storage, Editors: Rafid Al-Khory, Jochen Bundschuh, CRC Press, p 81-13.

Mariner, P. E., L. A. Connolly, L. J. Cunningham, B. J. Debusschere, D. C. Dobson, J. M. Frederick, G. E. Hammond, S. H. Jordan, T. C. LaForce, M. A. Nole, H. D. Park, F. V. Perry, R. D. Rogers, D. T. Seidl, S. D. Sevougian, E. R. Stein, P. N. Swift, L. P. Swiler, J. Vo and M. G. Wallace (2019). Progress in Deep Geologic Disposal Safety Assessment in the U.S. since 2010. Albuquerque, New Mexico, Sandia National Laboratories.

Mariner, P., Nole, M., Basurto, E., Berg, T. M., Chang, K. W., Debusschere, B., ... & Swiler, L. P. (2020). *Advances in GDSA Framework Development and Process Model Integration* (No. SAND2020-10787R). Sandia National Lab.(SNL-NM), Albuquerque, NM (United States); Sandia National Lab.(SNL-CA), Livermore, CA (United States).

Mills, R., C. Lu, P. C. Lichtner and G. Hammond (2007). Simulating subsurface flow and transport on ultrascale computers using PFLOTRAN. 3rd Annual Scientific Discovery through Advanced Computing Conference (SciDAC 2007), Boston, Journal of Physics Conference Series.

Mualem, Y. (1976). A new model for predicting the hydraulic conductivity of unsaturated porous media. *Water resources research*, *12*(3), 513-522.

Navarre-Sitchler, A., R. M. Maxwell, E. R. Siirila, G. E. Hammond and P. C. Lichtner (2013). "Elucidating geochemical response of shallow heterogeneous aquifers to CO2 leakage using high-performance computing: implications for monitoring CO2 sequestration." Advances in Water Resources 53: 44-55.

Painter, S. L. (2011). Three-phase numerical model of water migration in partially frozen geological media: model formulation, validation, and applications. *Computational Geosciences*, *15*(1), 69-85.

Powers, J. M. (2004). On the necessity of positive semi-definite conductivity and Onsager reciprocity in modeling heat conduction in anisotropic media. *J. Heat Transfer*, *126*(5), 670-675.

Price, L. et al., 2019. "Preliminary Analysis of Postclosure DPC Criticality Consequences." M2SF-20SN010305061, SAND2020-4106. Sandia National Laboratories, Albuquerque, NM.

Price, L. et al., 2020. "Status Report - Progress in Developing a Repository-Scale PA Model." M4SF-20SN010305064. Sandia National Laboratories, Albuquerque, NM.

Rossi, C., & Nimmo, J. R. (1994). Modeling of soil water retention from saturation to oven dryness. *Water Resources Research*, *30*(3), 701-708.

Sevougian, S. D., E. R. Stein, T. LaForce, F. V. Perry, T. S. Lowry, L. J. Cunningham, M. Nole, C. B. Haukwa, K. W. Chang and P. E. Mariner (2019a). GDSA Repository Systems Analysis Progress Report. Albuquerque, New Mexico, Sandia National Laboratories.

Sevougian, S. D., P. E. Mariner, L. A. Connolly, R. J. MacKinnon, R. D. Rogers, D. C. Dobson and J. L. Prouty (2019b). DOE SFWST Campaign R&D Roadmap Update, Rev. 1. Albuquerque, New Mexico, Sandia National Laboratories.

SKBF. 1983. Final storage of spent nuclear fuel - KBS-3. Volumes I - IV. Stockholm: Swedish Nuclear Fuel and Waste Management.

Skopp, J., and A.W. Warrick (1974) A two-phase model for the miscible displacement of reactive solutes in soils, Soil Sci. Soc. Am. Proc., 38(4), 545–550.

Somerton, W. H., Keese, J. A., & Chu, S. L. (1974). Thermal behavior of unconsolidated oil sands. *Society of Petroleum Engineers Journal*, *14*(05), 513-521.

Stein, E. R., J. M. Frederick, G. E. Hammond, K. L. Kuhlmann, P. E. Mariner, and S. D. Sevougian 2017, April 9-13, 2017. Modeling Coupled Reactive Flow Processes in Fractured Crystalline Rock. Paper presented at the International High-Level Radioactive Waste Management Conference, Charlotte, NC.

Sudicky, E.A. and E.O. Frind (1984) Reply. Water Resources Research, 20 (9), 1323–1324.

Sudicky, E.A., Frind, E. (1982) Contaminant transport in fractured porous media: Analytical solution for a system of parallel fractures. Water Resources Research, 18 (3), 1634–1642.

Sun, Y., Buscheck, T. A., Lee, K. H., Hao, Y., & James, S. C. (2010). Modeling thermal-hydrologic processes for a heated fractured rock system: impact of a capillary-pressure maximum. *Transport in porous media*, *83*(3), 501-523.

Tang DH, Frind, EO and Sudicky EA, 1981. "Contaminant transport in fracture porous media: analytical solution for a single fracture". Water Resources Research, 17(3), 555-564. doi: 10:1029/WR017i003p00555

TRW Environmental Safety Systems, "Spent nuclear fuel effective thermal conductivity report," U.S. Department of Energy, Yucca Mountain Site Characterization Project Office, Las Vegas, NV, MOL.19961202.0030, July 11 1996. [Online]. Available: https://www.osti.gov/servlets/purl/778872

Van Genuchten, M. T. (1980). A closed-form equation for predicting the hydraulic conductivity of unsaturated soils. *Soil science society of America journal*, *44*(5), 892-898.

Webb, S. W. (2000). A simple extension of two-phase characteristic curves to include the dry region. *Water Resources Research*, *36*(6), 1425-1430.

Winterle, J. 1998. Matrix Diffusion Summary Report. Center for Nuclear Waste Regulatory Analyses, San Antonio, TX.

Wolfram Research, Inc., Mathematica, Version 12.0, Champaign, IL (2019).

# 5. APPENDICES

## 5.1 Appendix A: Single Component System with First-Order Kinetics

Consider a batch reactor with a single precipitation-dissolution reaction

$$A_{(aq)} \rightleftharpoons A_{(s)}$$

with aqueous species $A_{(aq)}$ and solid $A_{(s)}$. Assuming variable surface area with a power law formulation, the governing equations are given by

$$\begin{aligned} \frac{d}{dt}(\phi c) &= -\hat{a}_s(\phi_s)^n \hat{I}_s, \\ \frac{d\phi_s}{dt} &= \overline{V}_s \hat{a}_s (\phi_s)^n \hat{I}_s, \end{aligned}$$

for porosity $\phi(t)$, aqueous concentration $c(t)$, solid volume fraction $\phi_s(t)$ with molar volume $\overline{V}_s$, and surface area parameter $\hat{a}_s$. The quantity $\hat{I}_s$ denotes the reduced reaction rate normalized to unit surface area

$$\hat{I}_s = k_s(c - c_{eq})\zeta_s,$$

where $\zeta_s(t)$ takes on the values one or zero depending on whether the solid is present or supersaturated, or undersaturated and not present, respectively. If the mineral is present initially $\hat{a}_s$ has the value

$$\hat{a}_s = a_s^0(\phi_s^0)^{-n},$$

where $a_s^0$ and $\phi_s^0$ denote the initial solid surface area and volume fraction, respectively. These equations are subject to the initial conditions $c(0) = c_0$ and $\phi_s(0) = \phi_s^0$. The quantity $\chi$ defined by

$$\chi = \phi c + \overline{V}_s^{-1}\phi_s = \phi_0 c_0 + \overline{V}_s^{-1}\phi_s^0,$$

is conserved.

As noted by Kräutle et al. (2020), for $n \neq 0$ these equations as written yield the spurious solution $\phi_s^{k+1} \equiv 0$ for a supersaturated solution at the $k+1$st time step, when the solid phase has completely dissolved at the previous step ($\phi_s^k = 0$). This follows from the explicit finite difference solution

$$\begin{aligned} \phi_s^{k+1} &= \phi_s^k + \Delta t \overline{V}_s \hat{a}_s \left(\phi_s^k\right)^n \hat{I}_s^{k+1}, \\ &= 0. \end{aligned}$$

Transforming to the variable $\xi_s = (\phi_s)^{1-n}$ gives the equations

$$\begin{aligned} \frac{d}{dt}(\phi c) &= -\hat{a}_s(\xi_s)^{n/(1-n)} \hat{I}_s, \\ \frac{d\xi_s}{dt} &= (1-n)\overline{V}_s \hat{a}_s \hat{I}_s, \end{aligned}$$

subject to the initial conditions $c(0) = c_0$ and $\xi_s(0) = \xi_s^0$. This reformulation of the problem circumvents the difficulty of a null solution

$$\begin{aligned} \xi_s^{k+1} &= \xi_s^k + \Delta t(1-n)\overline{V}_s \hat{a}_s \hat{I}_s, \\ &= \Delta t(1-n)\overline{V}_s \hat{a}_s \hat{I}_s > 0, \end{aligned}$$

since, by assumption $0 \leq n < 1$ and $\hat{I}_s > 0$. Porosity is related to $\xi_s$ according to the equation

$$\begin{aligned}\phi &= 1 - \phi_s,\\ &= 1 - \xi_s^{1/(1-n)},\end{aligned}$$

a function of the free-ion primary species concentration through the reduced reaction rate.

An example involving precipitation for a single component system in a batch reactor without the solid phase initially present is shown in Figure 2 using Mathematica NDSolve (Wolfram Research Inc., 2019) with the algorithm listed in Figure 4-1. Different surface area powers $n = 0,\ 1/2,\ 2/3$ are used (see caption to Figure 2). Note that for $n = 0$, $\phi_s = \xi_s$. Had $\phi_s$ been used in place of $\xi_s$, Mathematica would have found the null solution.

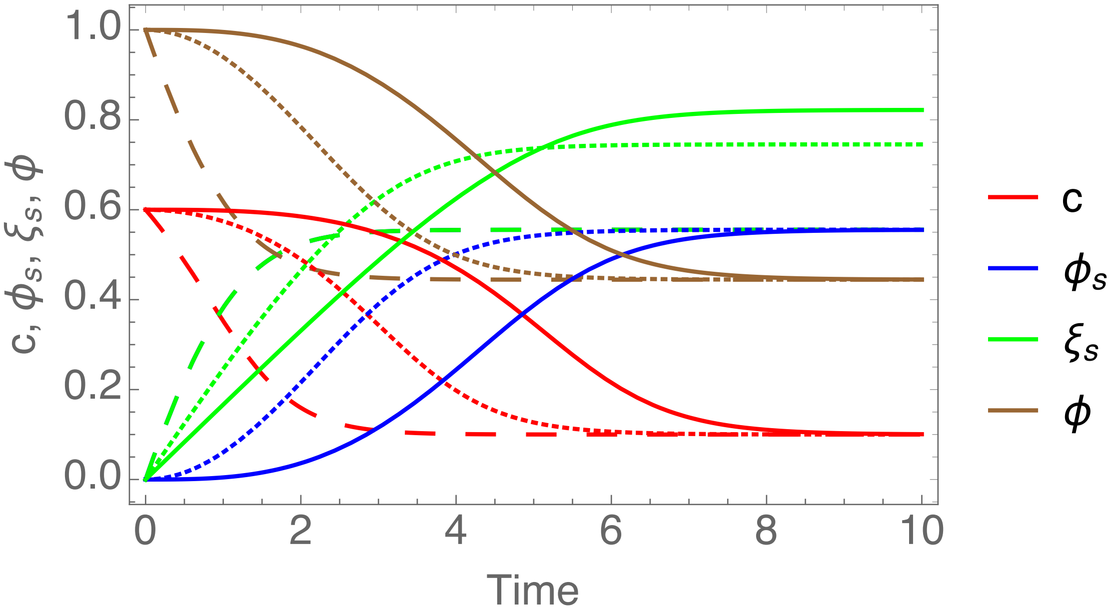

Figure 5-1 Solution using Mathematica NDSolve (Wolfram Research Inc., 2019) with the algorithm listed in Table 4-1 for $n = 0$ (dashed), 1/2 (dotted), 2/3 (solid) curves for aqueous concentration $c$, mineral volume fraction $\phi_s$, $\xi_s$ and porosity $\phi$ plotted as a function of time. Parameters used in the comparison are $c_{eq} = 0.1$, $c_0 = 0.6$, $k_s = 1$, $\hat{a}_s = 1$, $\overline{V}_s = 1$, $\xi^0_s = 0$ and $t_{max} = 10$.

Table 5-1 Mathematica (Wolfram Research Inc., 2019, Version 12.0) Solution using NDSolve

```
n = 2/3;
exipor23 = NDSolve[{
   (1 - xi[t]^(1/(1 - n))) c'[t] -
     1/(1 - n) xi[t]^(n/(1 - n)) xi'[t] c[t] == -k xi[t]^(n/(1 - n)) (c[t] - ceq),
   xi'[t] == (1 - n) vs k (c[t] - ceq),
   c[0] == c0, xi[0] == xi0},
  {c, xi}, {t, 0, tmax}]
```

## 5.2 Appendix B: Example Usage of TCCs

This appendix provides an example of how thermal characteristic curves can be specified in a PFLOTRAN input deck.

```
#========================== material properties ==============================

MATERIAL_PROPERTY shale

  ID 1

  CHARACTERISTIC_CURVES shale

  POROSITY 0.20

  TORTUOSITY_FUNCTION_OF_POROSITY 1.4

  SOIL_COMPRESSIBILITY 1.6d-8

  SOIL_COMPRESSIBILITY_FUNCTION LEIJNSE

  SOIL_REFERENCE_PRESSURE 101325.d0

  ROCK_DENSITY 2700.

  THERMAL_CHARACTERISTIC_CURVES cct_shale

  HEAT_CAPACITY 830.

  PERMEABILITY

    PERM_ISO 1.d-19

  /

/

MATERIAL_PROPERTY buffer

  ID 12

  CHARACTERISTIC_CURVES bentonite

  POROSITY 0.35

  !TORTUOSITY 0.23

  TORTUOSITY_FUNCTION_OF_POROSITY 1.4

  SOIL_COMPRESSIBILITY 1.6d-8

  SOIL_COMPRESSIBILITY_FUNCTION LEIJNSE

  SOIL_REFERENCE_PRESSURE 101325.d0

  ROCK_DENSITY 2700.

  THERMAL_CHARACTERISTIC_CURVES cct_buffer

  HEAT_CAPACITY 830.

  PERMEABILITY

    PERM_ISO  1.d-20

  /

/
```

```
#======================= thermal characteristic curves ========================
THERMAL_CHARACTERISTIC_CURVES cct_shale
  THERMAL_CONDUCTIVITY_FUNCTION DEFAULT
    THERMAL_CONDUCTIVITY_DRY   0.600D+0 W/m-C
    THERMAL_CONDUCTIVITY_WET   1.200D+0 W/m-C
  END
END

THERMAL_CHARACTERISTIC_CURVES cct_buffer
  THERMAL_CONDUCTIVITY_FUNCTION DEFAULT
    THERMAL_CONDUCTIVITY_DRY   0.600D+0 W/m-C
    THERMAL_CONDUCTIVITY_WET   1.500D+0 W/m-C
  END
END
```

(This page is intentionally blank.)